Defect-mediated charge transport in semiconducting structures based on copper oxide

A master's thesis submitted by

Jules Zaleski

for the Department of physics and Civil Engineering in fulfillment of the requirements for the degree of Master in Engineering Physics

Under the supervision of:

Prof. N.D. Nguyen

Prof. B. Vanderheyden

Members of the Jury:

Prof. J.M Redouté

Dr. L. Manceriu

University of Liege - Faculty of applied sciences

Academic year 2023-2024

ATFE9007-1 — Master's thesis

Contents

Chapter 1

Introduction

Nowadays, there is an increasing development in the use of transparent conducting oxides (TCO) to make gas sensors, photodiodes, light-emitting diodes (LEDs), and solar cells. All these technologies could be used to make smart windows or flexible surfaces for example as they are transparent with TCOs. The materials making TCOs are cheaper than conventional silicon and abundant compared to classical compounds such as arsenic. They are binary compounds with a simple metal and oxygen. Of course, TCOs are semiconductors with a band gap large enough to guarantee transparency to certain wavelengths. Moreover, the band gap might not be enough. To ensure transparency, one needs to work with thin films with a thickness under the micron. Common semiconducting TCOs are Al-doped zinc oxide (AZO), zinc oxide, titanium dioxide, nickel oxide, cuprous oxide (Cu_2O), and so on.

There is already a lot of research and development on the use of TCOs to produce the best solar cells with cheap, available, and efficient materials. However, the work becomes complicated when the type of the semiconductor is considered. n-type TCOs are not an issue as they have larger mobility (electrons have larger mobility than holes) and the list is long. For p-types, the oxygen orbitals affect the valence band structure which, in return, makes p-type metallic oxide quite rare [1]. One way to avoid this effect is to use a compound with a larger band gap. The challenge is to find or design p-type TCOs that exhibit as good performances as n-type counterparts to make electronics with both n- and p-type materials.

Among the previously stated examples of TCOs, only two are of type p: NiO [2] and Cu_2O [1]. These are not the only ones: V_2O_3 [3] and Cr_2O_3 [4], are other examples. However, the one that has the largest band gap is the cuprous oxide with a band gap of approximately 2.1 eV making it partially transparent (if not too thick). Moreover, cuprous oxide being non-toxic, cheap and copper being abundant, Cu_2O is the most promising p-type TCO nowadays. It is naturally of type p, without dopants, owing to copper and oxygen vacancies in the crystal.

Moreover, several dopants are available, the two options available in the lab are magnesium and nitrogen. In this work, only nitrogen is considered. It decreases the cuprous oxide resistivity and is easily added in the deposition process that is considered in this work, namely, radio-frequency magnetron sputtering.

This cuprous oxide can be integrated into a lot of heterostructures (with other TCOs). One can make photodiodes [5], gas sensors [6], LEDs [7] and solar cells [8]. Our main interest is in the use of cuprous oxide in solar cells as it makes use of its gap. Having a solar cell made of TCOs could lead to smart windows producing electricity. However, the current efficiency of such cells (AZO-Cu_2O) is not above 8.7 % in practice [9] where, in theory, it can be up to 20 % [10]. This means that there is quite a lot of work to find how to engineer the defects in the bulk and the interfaces of the cuprous oxide to increase its efficiency. To this end, researchers have been trying to add intermediate layers as buffers to mitigate the effect of interface states between the n and p-type. The most commonly used are ZnO [11], TiO_2 [12], Ga_2O_3[10], CdS [11] and so on. Each of these buffers is n-type TCO with a larger band gap than Cu_2O to increase the cell efficiency.

This work aims to determine and understand how interfaces between metals and cuprous oxide or n-type and cuprous oxide interact. How do the properties of the interfaces impact the characteristics of the device? Is it possible to understand these defects and control them to increase solar efficiency?

This work is articulated in 4 chapters. The first one consists of a general theoretical reminder about semiconductors. The concepts of bands, charge carriers, drift, diffusion current, and doping for n and p-type semiconductors are quickly reintroduced. Then, the homojunction (pn) is explained with the current-voltage Shockley theory. After that, heterojunction theory is deduced from the homojunction. Some time is spent on the contact metal-semiconductor. Then, to introduce the solar cell, the different generation and recombination mechanisms are introduced. Finally, the solar cell is explained with its structure and the criteria of contacts and efficiency. The second part of this chapter focuses on the current state of the art of Cu_2O. Its general characteristics, the doping possibilities, and their effect are presented. Then, time is spent on interface states which are one of the main challenges of cuprous oxide cells. The deposition technique and post-annealing are introduced.

The second chapter focuses on the tools used during this work and the fabrication methodology. First, the deposition tools are introduced, namely, RF sputtering and thermal evaporation. Next, the measurement tools are also explained. These are structural and electrical measurement machines. Then, the second part consists of the sample fabrication, and their electrical and optical characterization to understand what is studied with the samples. Thermal annealing is tested and its effect on the crystallinity and the electrical properties is discussed. The mobility is also discussed with regard to the crystal orientation. Lastly, a silver deposition on the cuprous oxide is considered with an undesired behavior.

The next chapter develops the metallic contact tungsten-cuprous oxide. It is shown that the current through the contact follows neither an ohmic nor a rectifying behavior. The space-charge-limited current model is introduced and applied to the current-voltage measurements of the samples of cuprous oxide as has been done already in some studies.

The last chapter tackles the solar cell Ga_2O_3-Cu_2O. First, the numerical tool Scaps is fully introduced, and validated with the theory of the homojunction. This first part aims to have a complete understanding of the tool before using it for our cell of interest. Once this is done,

the main cell is, at first, studied in its pristine form to find the optimal parameters, under some stated hypotheses. Next, defects are added in both compounds from the literature to understand their effects on the optimal parameters. Lastly, to add a buffer to the cell, the AZO-Ga_2O_3-Cu_2O cell is studied to also find the optimal parameters of AZO in its pristine form. The efficiency is not as high as hoped. Prospects are discussed with the different assumptions and the numerical tools to understand this effect.

The end of this work consists of a conclusion and the different references of this work.

Chapter 2

Theoretical background

2.1 Semiconductor and band theory

Semiconductors are materials that have special optical properties. The crystal structure of the semiconductor can absorb incoming light to produce electricity or from a given current, emit light such as LEDs (light emitting diodes).

To understand these phenomena, it is important to recall the energy band structure of semiconductors. When unexcited at 0 K, all the electrons are in the valence band at a certain level of energy. To excite the electrons, one can heat the crystal or shine a light on its surface, which means, sending photons. In this work, no temperature effects are considered. Planck's relation that links the light and the energy of the photon E_λ is given in as.

$$E_\lambda = \frac{hc}{\lambda}, \tag{2.1}$$

where λ is the wavelength of the light, c is the speed of light, and h Planck's constant.

If the exciting energy is large enough, the electron can cross the energy band gap E_g to the conduction band. Having multiple free electrons being able to move produces an electric current. Furthermore, the electron, by leaving the valence band, makes a hole in the surrounding of the atom he was in. The hole can move and represents the movement of a particle of positive charge. The process of electron-hole pair generation is illustrated in Figure 2.1.

The transition of the electron can be direct or indirect. In the case of the Figure 2.1, this is a direct band gap because the minimum of the conduction band is at the same wavenumber k than that of the maximum of the valence band. The direct or indirect band gap character influences the light absorption as seen later in section 2.6. If the extrema are not at the same wavenumber, as is the silicon case, it is an indirect band gap semiconductor.

2.2 Intrinsic and doped semiconductors

A pure crystal is called intrinsic. It means that there are always the same number of excited electrons and holes. Once an electron crosses the band gap, it leaves a hole.

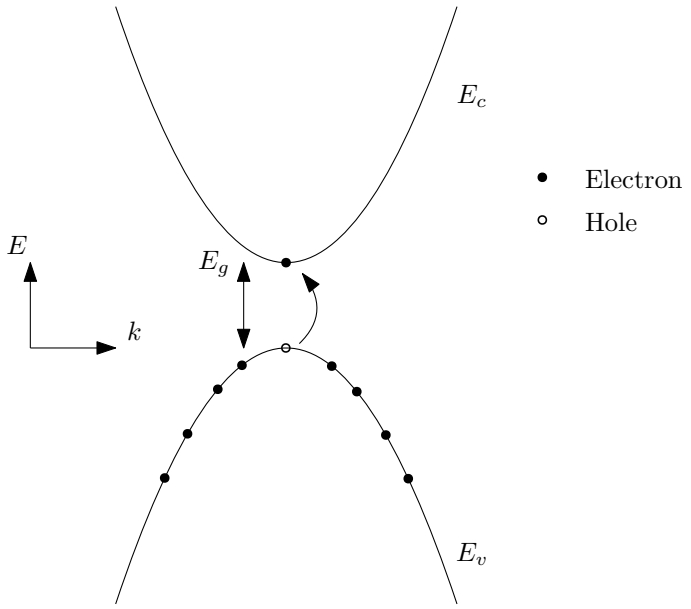

Figure 2.1: Electron-hole pair generation in a direct gap semiconductor with the parabolic band approximation.

This gives

$$n = p = n_i, \tag{2.2}$$

where n is the concentration of free electrons in the crystal (in number per cm^3), p is the concentration of holes and n_i is the concentration of electrons in the intrinsic semiconductor.

To characterize the available states for the electrons in the conduction band at a certain energy E, one introduces the Fermi-Dirac statistics. Without light excitation and generation of charge carriers (i.e. electrons and holes), the Fermi-Dirac function gives the probability of occupation of states as in

$$f(E) = \frac{1}{1 + \mathrm{e}^{\frac{E - E_f}{k_b T}}}, \tag{2.3}$$

where E_f is the Fermi level of the compound, k_b is Boltzmann's constant, and T is the temperature in SI units.

This distribution gives statistical information about the distribution of electrons and holes in the band diagram. For intrinsic crystals, the Fermi level is close to the middle of the band gap. This is seen on the left of Figure 2.2. Given the Fermi distribution, in a non-degenerate case, the charge carrier concentrations are given by

$$n = n_i \cdot e^{\frac{E_f - E_i}{K_b T}}, \qquad p = n_i \cdot e^{-\frac{E_f - E_i}{K_b T}}, \tag{2.4}$$

where E_i is the intrinsic level, defined as the value taken by E_f for an intrinsic semiconductor.

In practice, a crystal is never pure and some impurities can get in, with a low concentration. These impurities can have a different valence than the crystal. Hence having more electrons in the last layer of the atom or less. If it has more, this impurity tends to give an electron away more easily. This free electron can be released in the conduction band. The atom

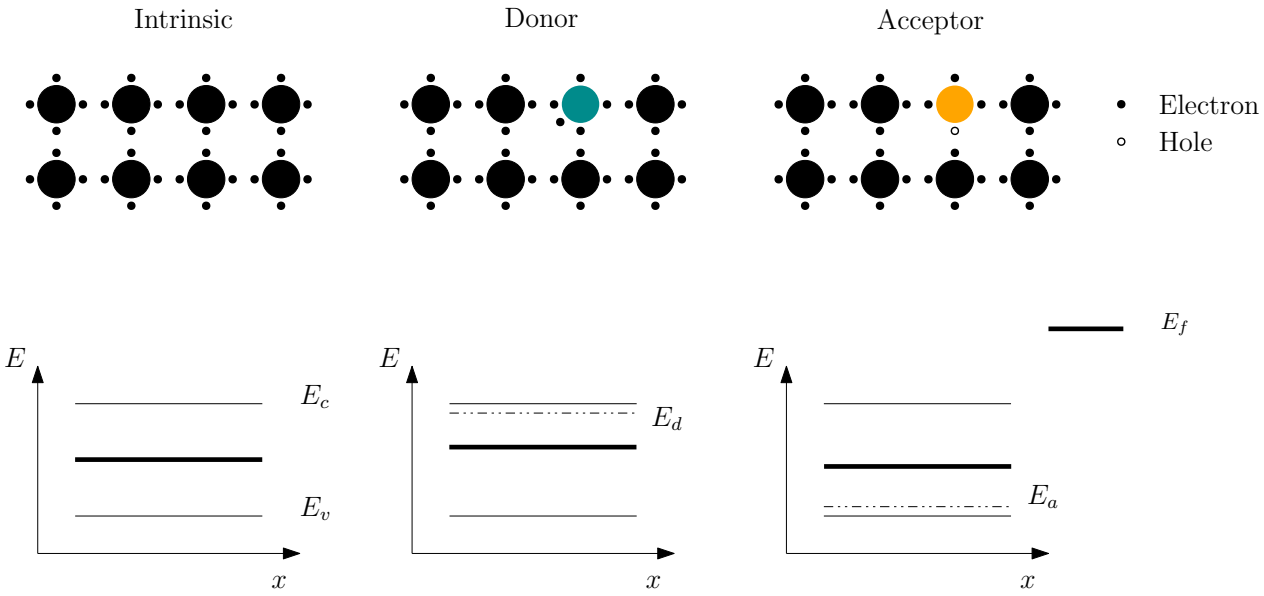

Figure 2.2: Comparison of the atomic structure and the band gap of an intrinsic (left), n-doped (center), and p-doped (right) semiconductor.

that gives electrons easily is called a donor. It is represented by a new energy level, E_d, closer to the conduction band than the valence band. The second possibility is an impurity with fewer electrons than the atoms of the crystal. It has a larger electron affinity than the pure bulk and tends to capture an electron, thus creating a hole in the valence band of the semiconductor. This impurity is called an acceptor and has an energy level, E_a, closer to the valence band. These behaviors are respectively seen in the center and the right of Figure 2.2.

Having impurities improves the conductivity of the material by having more charge carriers. Hence, materials that have a majority of donors with a concentration N_D are called n-type. The donors add extra electrons and this changes the balance of electrons and holes. Hence, to satisfy Fermi's statistics, the Fermi level is closer to the conduction band as seen in Figure 2.2. If it is a majority of acceptors with a concentration N_A, it is a p-type and the Fermi level is closer to the valence band as seen in Figure 2.2.

2.3 Current in the semiconductor

An important point of comprehension on the semiconductor is the current mechanism. There exist two ways for charge carriers (electrons and holes) to move across the bulk.

2.3.1 Drift current

Drift current occurs when an electric field is applied along the semiconductor. Naturally, the charge carriers undergo a force $\vec{F} = q\vec{E}$. By introducing the carrier mobility for electron and holes, respectively μ_n and μ_p, one can find

$$\vec{J}_n^{\text{drift}} = q\mu_n n\vec{E}, \qquad \vec{J}_p^{\text{drift}} = q\mu_p p\vec{E}. \tag{2.5}$$

2.3.2 Diffusion current

The diffusion current is due to a gradient of minority carriers in the semiconductor. This can be due to an injection of carriers at a specific location of the compound for example. Those out-of-balanced carriers diffuse in the semiconductor until they recombine with a majority carrier to have a uniform distribution of carriers. It is also expected that the diffusion length, which is the characteristic length a minority charge carrier travels before being recombined, depends on the material. Hence, one can find the average diffusion current density of electrons (J_n^{diff}) and holes (J_p^{diff}) as in

$$\vec{J}_n^{\text{diff}} = -qD_n\nabla n, \qquad \vec{J}_p^{\text{diff}} = qD_p\nabla p, \tag{2.6}$$

where q is the charge of the electron, n and p are the carriers concentration and D_n and D_p are the diffusion coefficient of the carriers.

Note that to find the diffusion coefficient, one can use the Einstein-Debye relation which says that at thermal equilibrium without incoming photons, no current is expected and thus, the sum of the drift and the diffusion is zero. One finds Equation 2.7 with Equation 2.4,2.5 and 2.6 and has

$$\frac{D_n}{\mu_n} = \frac{k_bT}{q} = \frac{D_p}{\mu_p}. \tag{2.7}$$

2.4 Homojunction: *pn* junction device

A common semiconductor combination is a pn junction. It consists of having a semiconductor split into two parts: one p-type next to a type n. For the sake of explanation, the junction is at first considered perfect, which means that the contact between the two is perfect. No surface charges are considered.

Once the contact is made, it is expected that a part of the free electrons from the n-type semiconductor on the right goes to the left, diffuses, and recombines with the free holes, and vice versa, some free holes may travel to the right in the n-type to recombine too, thus leaving near the contact a zone without free carriers. What remains are dopants which are donors in the n-type and acceptors in the p-type. This zone, with a width $W = x_n + x_p$, is called the depletion region where an electric field opposed to the movement of the free carriers across the pn contact appears. This makes an equilibrium of charge between the two semiconductors and is represented in Figure 2.3. The equilibrium in the depletion region where the only charges are acceptors and donors induces charge neutrality and is expressed in

$$x_nN_d = x_pN_a. \tag{2.8}$$

To understand the upcoming physics, the energy band diagram is plotted in Figure 2.4, with each n and p side with their own Fermi level due to doping. To guarantee equilibrium, the Fermi level must be at the same level, thus, there is a bend in the valence and conduction bands near the contact.

To find the different properties of a junction at equilibrium, one can introduce the contact

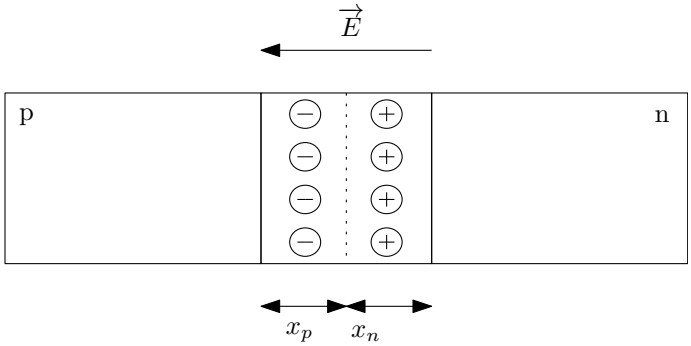

Figure 2.3: Schematic of an ideal homogeneous pn-junction at equilibrium.

potential V_0 or built-in potential. Then, Poisson's equation can be solved in the depletion region as in

$$\frac{\rho}{\varepsilon_0} = -\Delta V.$$

The computations are not detailed here but well in *The handbook of photovoltaic science and engineering* [13].

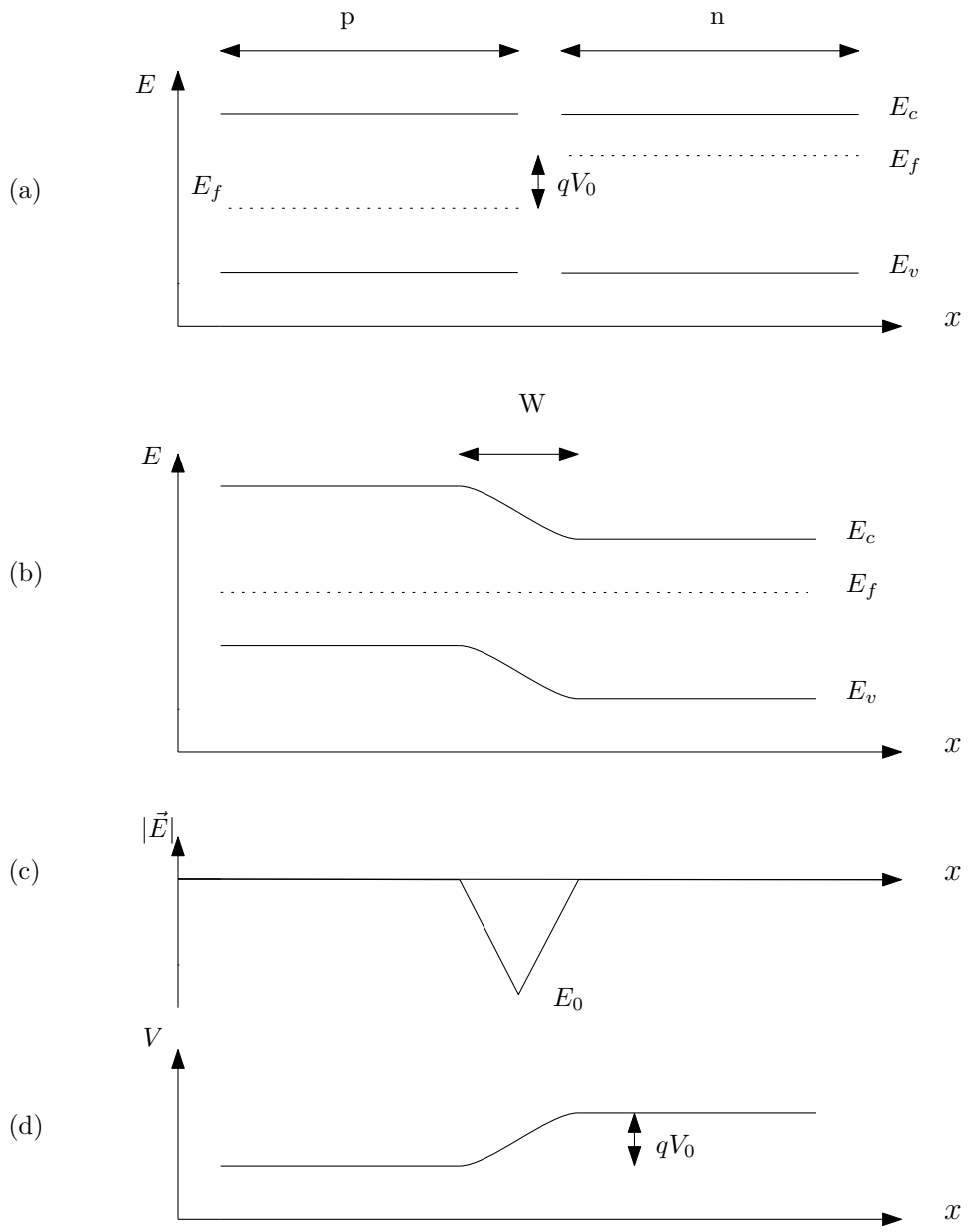

Figure 2.4: Energy band diagram of an ideal homogeneous pn junction (a) before and (b) after the contact of the two semiconductors. (c) Magnitude of the electric field across the junction. (d) Potential across the junction.

2.4.1 Rectification at a semiconductor junction

A *pn* junction becomes interesting once a potential is applied across the device. In one direction, it allows for a drift of the carriers in the depletion region plus the diffusion of charge carriers, thus, a larger current. In the other direction, there is only a small current opposed as to the previous one is visible.

Forward bias

First, let us consider the effect of a positive voltage to the right. It induces an electric field opposed to the equilibrium electric field of the junction. This decreases the potential barrier as seen in Figure 2.5 and allows for more charges to cross the depletion region. This induces a net current to the right. Out of equilibrium, the current density of minority and majority

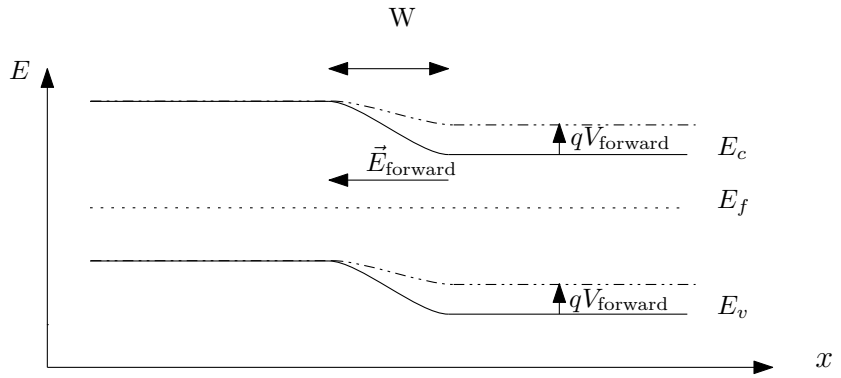

Figure 2.5: Energy band diagram of an ideal *pn* junction under a forward bias.

carriers is not constant in the junctions. Intuitively, the current density along the junction can be decomposed between drift and diffusion for electrons and holes. Without going into the details, the current density is plotted in Figure 2.6. The drift of the majority carriers is

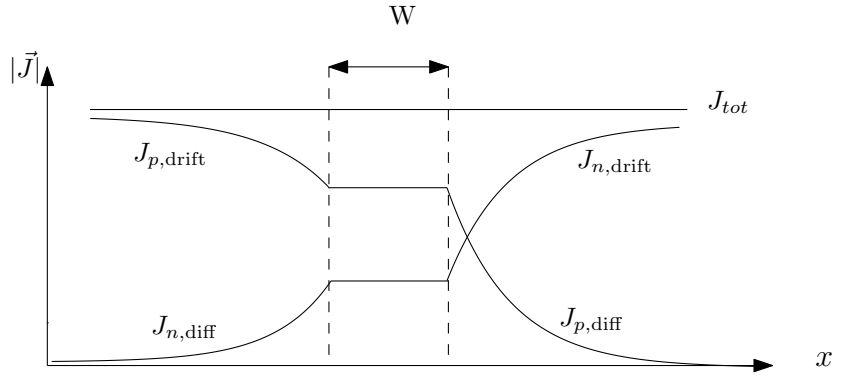

Figure 2.6: Current density of an ideal *pn* junction under a forward bias for a long junction.

due to the local electric field in the depletion region, given by the equilibrium electric field and the applied potential. When carriers are generated in or near the depletion region (they can diffuse in the depletion region), they undergo the local electric field in the depletion region and are accelerated.

The diffusion can be quite important because the barrier has been lowered between the n and the p-type. This lowering of the barrier increases the number of carriers crossing the depletion width. But far from the depletion region, the minority carriers have recombined and the diffusion current is zero if the semiconductor is long enough.

Reverse bias

In the case of a negative potential applied across the junction, the energy barrier between the two semiconductors is deeper as seen in Figure 2.7, and hence, decreases the diffusion current. Intuitively, the majority carriers from each side have more trouble crossing the depletion

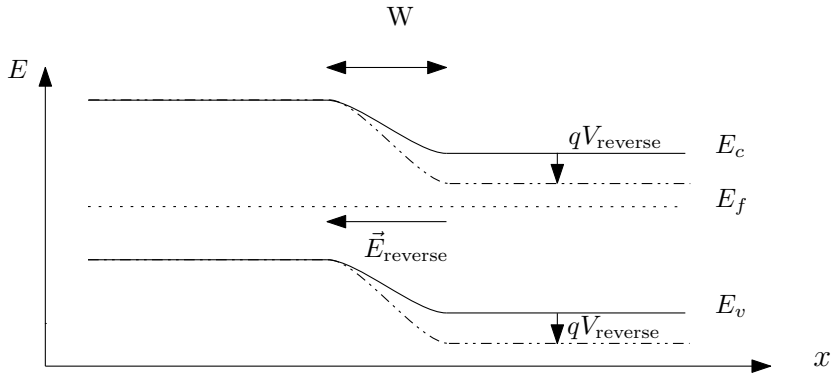

Figure 2.7: Energy band diagram of an ideal pn junction under a reverse bias.

region to become minority carriers and diffuse. This decreases the diffusion current. The drift current is due to the carriers generated near the depletion region (a distance smaller than the diffusion length) and expelled out by the electric field in the depletion region. Hence, without the diffusion current, the only contribution is the drift current. Note that the drift current does not vary much with the applied potential because the current does not depend on how fast the carriers are swept to the side but rather on how many carriers there are near the depletion region.

2.4.2 I-V curve

To fully characterize the electrical properties pn junction, one can plot the current-voltage curve (I-V curve) as done schematically in Figure 2.8.

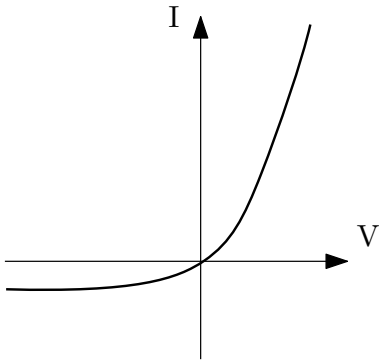

Figure 2.8: Schematic of an I-V curve for a non-illuminated pn junction.

To understand the I-V behavior of an ideal junction, thus a diode, one starts with the total current

$$J_{tot} = q\left(\frac{D_p p}{L_p} + \frac{D_n n}{L_n}\right) \cdot \left(e^{\frac{qV_{app}}{k_b T}} - 1\right).$$

This is plotted in Figure 2.6

Here, the minority diffusion current density in the diode has the shape of an exponential as in

$$J_{\text{diff}} = J_0 \cdot e^{\frac{qV_{app}}{k_b T}}. \tag{2.9}$$

As shown in Figure 2.8, the diffusion becomes exponentially larger as the applied bias increases. Hence, in forward bias, one can neglect the drift, and the current is only dictated by the diffusion of minority carriers. However, in reverse bias, diffusion is not favored and only remains a small constant drift current.

2.5 Heterojunction

Now that the *pn* junction between two identical semiconductors, the homojunction, is introduced, one can understand the heterojunction. Hence, a junction with two different semiconductors or a metal and a semiconductor.

2.5.1 Work function

To start with, let us introduce the work function, $q\phi$, of a crystal. This is the energy required to take an electron from the Fermi level, which depends on the doping level, and put it in the vacuum level, a level where it is free from the influence of the crystal. One important thing one should not forget is that the concept of work function only takes place in the context of the Schottky-Mott rule for thermionic emission. The work function in the bulk can be much different at the interface. It can change from one measurement to another because of different crystal quality and so on.

Taking two compounds to form a heterojunction with perfect contact still results in an alignment of the two Fermi levels. But this induces a change in the vacuum level for one of the two crystals, thus, a built-in potential, qV_0, appears in equilibrium. This potential is easily understandable. As soon as the contact is made, electrons flow out from the material which has the lowest work function. They go where it is harder to take them out, hence where it is more stable. An example of the contact is schematized in Figure 2.9. In Figure 2.9, the electronic affinity has also been introduced, $q\chi$ = Vacuum level - Conduction band. Here, this value does not depend on the doping. It becomes handy in the following chapter in the software.

It is seen that the contact can induce discontinuity in the bands and hence, different space charge distribution around the contact. These differences in the band can be expressed as in

$$\Delta E_c = q\chi_p - q\chi_n, \qquad \Delta E_v = E_{g,n} - E_{g,p} - \Delta E_c. \tag{2.10}$$

At equilibrium, the built-in potential induces an electric field in the depletion region and the same hypothesis is made as in the homojunction with charge neutrality in the depletion region and quasi-neutral region outside.

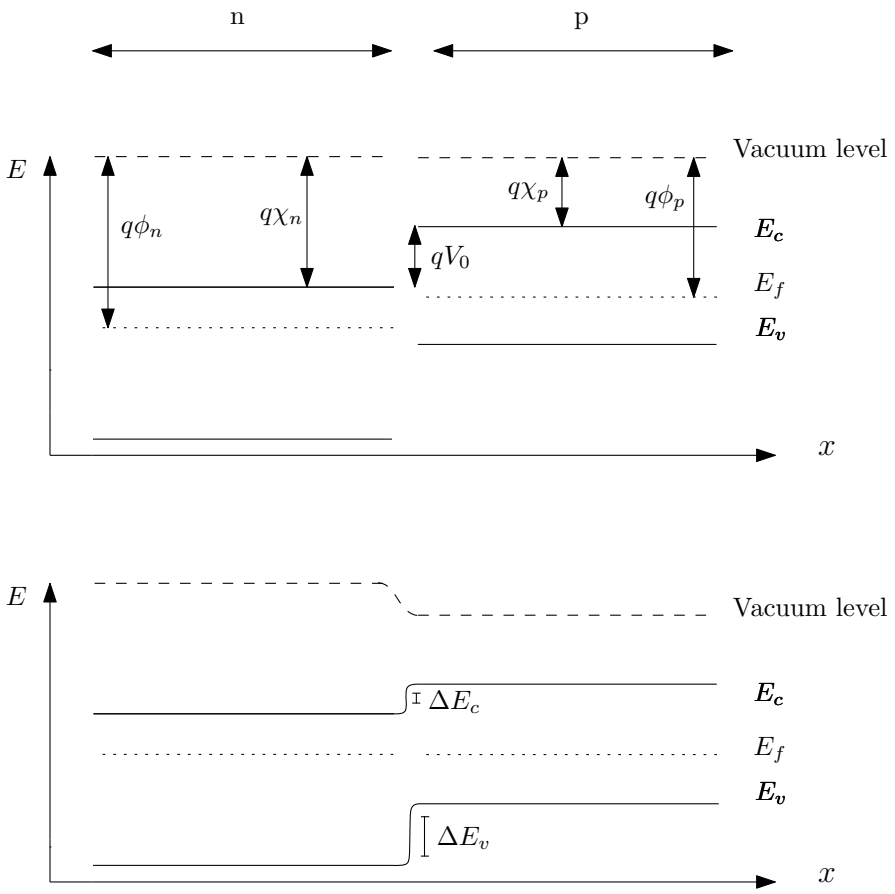

Figure 2.9: Scheme of the energy band diagram of a heterojunction between two semiconductors at equilibrium with ideal contact.

One can compute the heterojunction with Copper oxide (Cu_2O) and Gallium oxide (Ga_2O_3): From the data available in Table 2.1, one finds:

$$\Delta E_c = 4 - 3.2 = 0.8 \text{ eV} \qquad \Delta E_v = 2.7 + 0.8 = 3.5 \text{ eV}$$

Here, because gallium oxide has a larger band gap, it induces a smaller potential barrier for the electrons to go into the copper oxide, which eases the electron current.

	Cu_2O	Ga_2O_3
E_g [eV]	2.1	4.8
$q\chi$ [eV]	3.2	4

Table 2.1: Energy band diagram information for a heterojunction. Data available in [14], [15] and [16]

2.5.2 Applied bias

The same concepts as for the pn junction apply to forward and reverse bias voltage across the junction. The potential barrier gets higher or lower which increases or decreases the current

of charge carriers through the depletion region. Particular effects may happen at very high or very low potential but this is not considered in this work. Furthermore, one can, starting from Poisson's equation, find an expression for the quasi-neutral region's widths. This is given by [17] in the following

$$x_p = \left(\frac{2}{q}\varepsilon_1\varepsilon_2\frac{N_d}{N_a}\frac{V_0 - V_{app}}{\varepsilon_1 N_a + \varepsilon_2 N_d}\right)^{\frac{1}{2}}, \qquad x_n = \left(\frac{2}{q}\varepsilon_1\varepsilon_2\frac{N_a}{N_d}\frac{V_0 - V_{app}}{\varepsilon_1 N_a + \varepsilon_2 N_d}\right)^{\frac{1}{2}}. \tag{2.11}$$

These relations will be used later to check simulations. In these equations, the built-in potential, V_0, is simply the difference between the work functions of the two semiconductors.

2.5.3 Metal-semiconductor junction

Having a metal-semiconductor junction is common and can help us with doping characterization in the semiconductor. The construction of a metal-semiconductor junction used the Schottky-Mott rule which uses the work functions to determine contact conditions.

To understand the metal-semiconductor junction, the metal can be assumed to be ultra-doped with electrons. Two types of junctions are possible:

- Ohmic: the current can flow in the two directions. The barrier height does not prevent the charges from crossing the junction in any direction.
- Rectifying: the current flow is the same as the one of an I-V curve for two semiconductors, this is called a Schottky diode. The main difference between a *pn* diode and a Schottky one is that the latter works with majority carriers and not minorities. For a *p*-type in forward bias, the holes diffuse from the semiconductor to the metal and the barrier height prevents the holes from the metal to cross the junction to the semiconductor. In reverse bias, the barrier height remains the same but the hols from the semiconductor cannot diffuse in the metal anymore.

The rectifying behavior bends the valence and conduction bands as shown in Figure 2.10 for an *n*-type and a *p*-type semiconductor. From these diagrams, one can easily find the conditions to have a Schottky contact and the relations are given by

$$q\phi_m > q\phi_s \quad \text{for an } n\text{-type}, \qquad q\phi_m < q\phi_s \quad \text{for a } p\text{-type}. \tag{2.12}$$

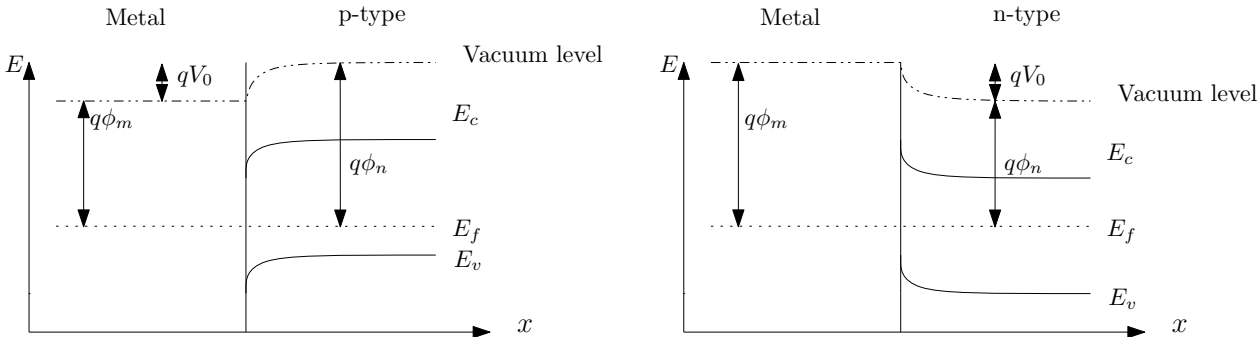

Figure 2.10: Scheme of the two rectifying contacts between an n-type semiconductor with a metal and a p-type semiconductor with a metal under no bias with assumed ideal contact.

2.6 Light absorption

As said earlier, photons can excite electrons in the valence band. This behavior is very important in semiconductor devices. There are multiple ways to have photon absorption. The energy E_λ must be greater than the energy band gap. The incoming energy induces the creation of charge carriers. It can be one electron or one hole from an intermediate state or an electron-hole pair (EHP). This absorption of light by the crystal is represented by an absorption coefficient α. The latter depends on the wavelength of the incident light. The absorption depth depends on this coefficient. Having a very large absorption coefficient means a very thin absorption layer.

To have light absorption, conservation of energy and momentum must be guaranteed. With the conservation criteria fulfilled, the absorption coefficient of the phonon, $\alpha(\nu)$, is dependent on the probability of transition between the valence to the conduction band and the density of states of both initial and final energy. The transition depends on the type of material:

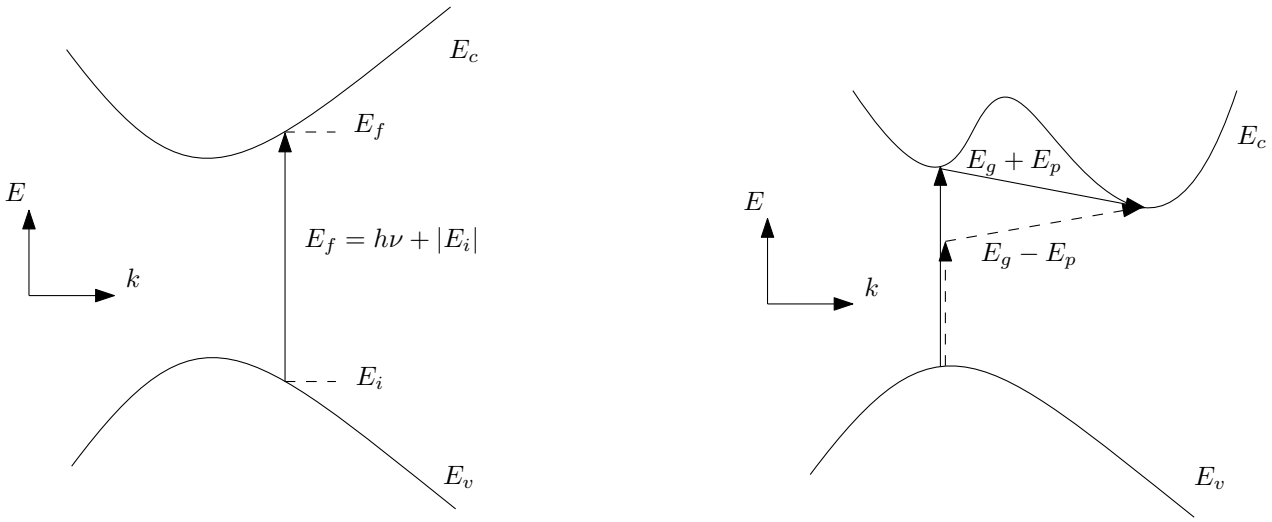

Figure 2.11: Electron hole pair generation for direct and indirect band gap material in the wavevector space.

- For direct band gap materials, the electron only crosses the band gap vertically in the k-space, hence, with momentum conservation (i.e. the momentum for particles is given by $p = \frac{h}{k}$ where k is the wavevector and where the photon momentum is negligible compared to the crystal momentum) as shown in the left of Figure 2.11.

- In the case of an indirect band gap material, there is at first a direct absorption and then a change in momentum to let the electron fall in the minimum of the conduction band. But to conserve the momentum, a phonon in the crystal may be absorbed or emitted. Both options are shown on the right of Figure 2.11. Hence, the total required energy is given for the absorption of phonons $(-)$ and the emission $(+)$ in

$$h\nu = E_g \pm E_p. \tag{2.13}$$

2.7 Recombinations

While charge carriers can be light generated, they can also recombine which decreases their density. There are three recombination processes, all schematized in Figure 2.12 and explained below.

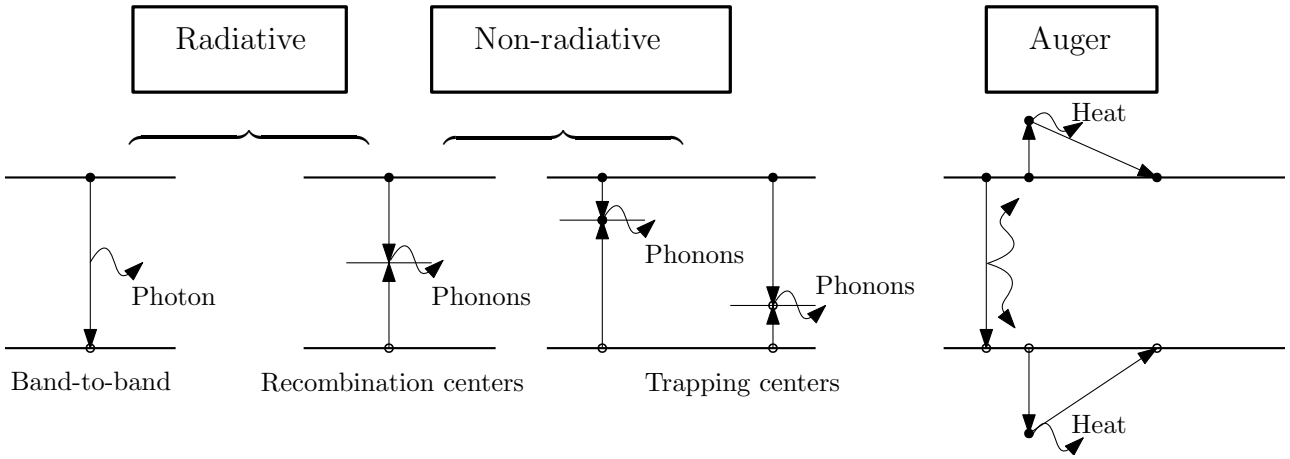

Figure 2.12: Scheme of the three recombination processes in a semiconductor.

- Band-to-band recombinations are radiative recombinations which happen without trap states. This phenomenon is more likely to happen in a direct gap semiconductor. This is the opposite of the optical generation, thus, after the recombination, a photon is emitted. If there is a radiative recombination in an indirect gap material, there is also a phonon generation for the optical generation. Radiative recombinations can also happen with traps with a photon emission.

- Indirect or non-radiative recombinations occur with the help of recombination levels due to defects or trap states in the band gap with phonons emission. The electron can be captured from the conduction band to the trap level by emitting phonons and thus heat and then recombine in the valence band by emitting another phonon. Or vice-versa for the hole.
  The difference between recombination centers and trap states is that the first captures with an equal probability of both electron and hole recombining while the second captures one type of carrier more easily. Hence, the first is located near the middle of the band gap, and the second is near the conduction band (so captures electrons more easily but holes more hardly) or the valence band (to capture holes more easily).

- Auger recombination is quite similar to radiative recombination. The key difference is that the energy is not emitted as a phonon but is given to another charge which will lose this excess of energy thermally.

All those recombination processes happen at the same time, hence, the net recombination is the sum of the three processes.

2.8 Solar cell

Finally, the solar cell device can be introduced. It is nothing more than a pn junction under light that can be used to produce electricity. One can take the classical junction and add an optical EHP generation. This produces a photocurrent, I_{ph}, which is given by:

- the drift of carriers optically generated in the depletion region,
- the diffusion of minority carriers of each side generated near the depletion region which goes to the depletion region.

This has an effect on the I-V curve plotted in Figure 2.13. I-V measurements can be made by measuring a current and applying a voltage across the junction.

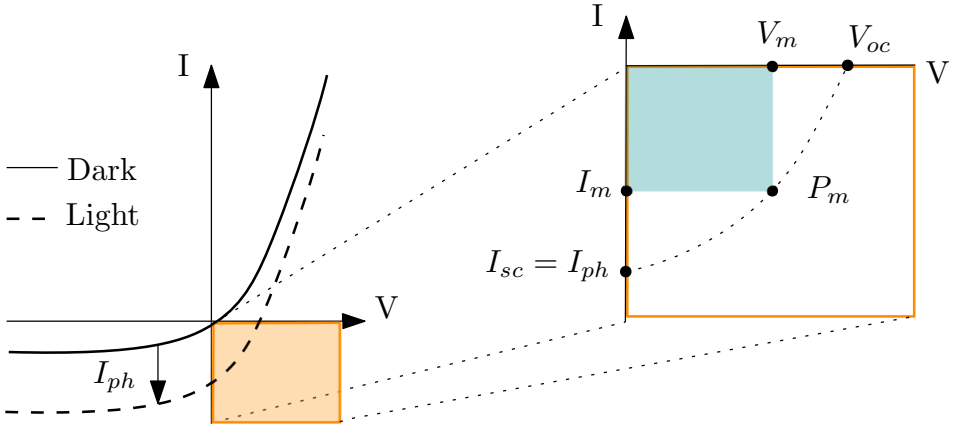

Figure 2.13: Scheme of an I-V curve with and without light.

As can be seen, compared to the curve in the dark, there is now a region on the bottom right in orange where there is power generation (using the passive sign convention). The point of maximum power, P_m, is given by

$$P_m = V_m I_m = FFV_{oc}I_{sc}, \tag{2.14}$$

where FF is the fill factor of the curve, V_{oc} is the open-circuit voltage and I_{sc} is the short-circuit current. From this, one can find the efficiency of the cell with

$$\eta = \frac{P_m}{P_{\text{solar}}} = \frac{FFV_{oc}I_{sc}}{P_{\text{solar}}}, \tag{2.15}$$

whereas E_g increases,

- V_{oc} increases as $I_{\text{dark}} \propto e^{-E_g/2k_bT}$ decreases,
- $I_{sc} \propto I_{ph}$ decreases because less photons are absorbed as the semiconductor is more transparent.

For our Cu_2O-Ga_2O_3 solar cell where Gallium oxide has a larger gap than copper oxide, having a larger band gap means a more transparent crystal. It is therefore better to have light on the Gallium side than the copper to have more electron-hole pair generations overall.

2.8.1 Solar cell structure

In reality, a solar cell is more complicated with multiple layers to maximize its performance.

- A small anti-reflective layer is added on the top to avoid reflection and have more absorption in the crystal.
- Use a thin layer electrode to avoid reflection too on the top and the back of the cell plus maximize the surface area of the exposed semiconductor.
- Use layers between the semiconductors and the electrode to guarantee good contacts and avoid too many interface defects.

2.8.2 Numerical source of light

For this work, simulations of the I-V curve are computed with a numerical source of light. To understand the solar spectrum used for the simulations, one first needs to see the impact of the air in the atmosphere as shown in Figure 2.14. The air mass number is defined by

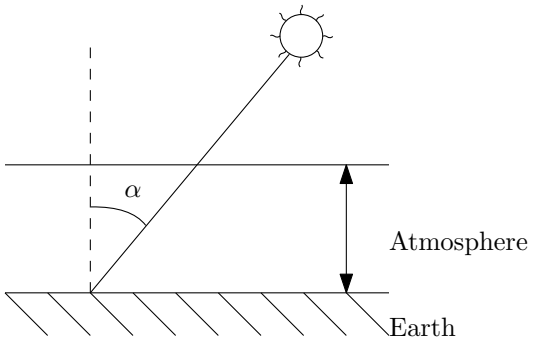

Figure 2.14: Schematic of the incident rays from the sun on the surface of the Earth.

$$\text{Air mass} = \frac{1}{\cos(\alpha)}. \tag{2.16}$$

For example, having a sun with an angle of 48.2° corresponds to AM = 1.5. For the simulation, the spectrum of the source of light represents the sun. The spectrum is : "AM1.5" normalised to a total power density of $P_{\text{solar}} = 1$ kW/m^2. It is useful because it takes the mass of the atmosphere for the diffusion of the sunlight before it touches the solar cell. The complete spectrum is shown in Figure 2.15.

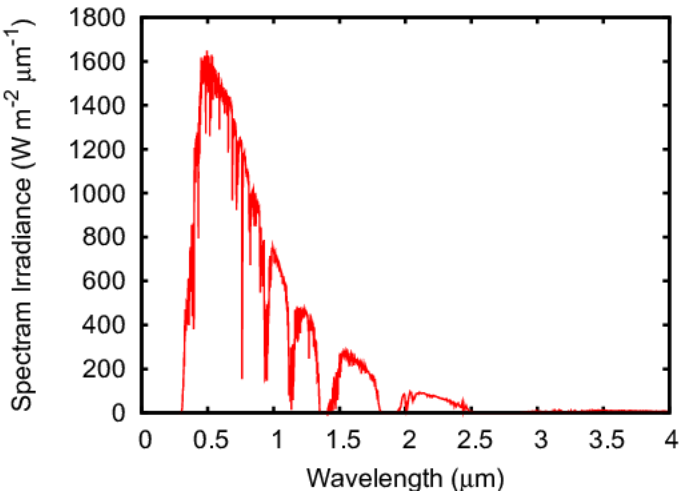

Figure 2.15: Solar spectrum AM 1.5 [18].

2.9 General introduction to copper oxide

To understand the interest of Cu_2O as an important transparent conducting oxide (TCO), one needs to understand the current knowledge and process of the nanofabrication of cuprous oxide films.

2.9.1 General characteristics

Cuprous oxide is one of the few TCOs that is *p*-type. Its *p*-type property comes from its oxygen and copper vacancies. It has a cubic lattice as seen in Figure 2.16 with direction-dependent mobility [19]. It is a direct band gap semiconductor with a band gap of around 2.1 eV. The value differs from different articles as it has been reported with 2 eV in [20] and 2.56 eV in [21]. The band gap is the largest when under Cu_2O form. It is the form with the least amount of oxygen atom per copper atom. The other forms are CuO and Cu_4O_3. Both of which are *p*-type but with lesser mobility and less transparency.

2.9.2 Deposition techniques

The fabrication of Cu_2O sample can be made with varying methods. One can grow thin films using ambient liquid-phase epitaxy with different levels of crystallinity and crystal orientation as used by Pan *et al.* in [19]. This allows for better electrical and optical properties. Another solution is using electrodeposition as in [23]. This is one of the cheapest methods. However, chemical deposition has a lower mobility than physical deposition techniques. Lastly, the method used in the lab is RF sputtering. This method allows us to dope the film during the deposition with an incoming flux of nitrogen. This method has been thoroughly described by Ishizuka *et al.* in [24]. This method is the one that provides the best mobility as shown by Li *et al.* in [25].

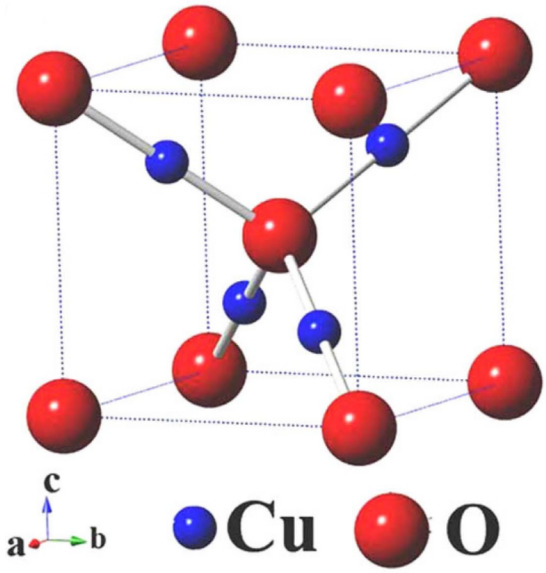

Figure 2.16: Cubic lattice of Cu_2O (a=4.29 V) [22]

2.9.3 Doping

Dopants in the semiconductors are defects that aim to add energy level to the materials. This increases the concentration of charge carriers and hence, decreases the resistivity. Several dopants are available for cuprous oxide (Cu_2O). One well-known is magnesium (Mg). It gives good electrical and optical properties to the film and is already studied in [26]. However, this doping must be made in bulk before the sputtering. Another promising doping is nitrogen. It is the best, with the current state of the art, dopant as it provides the film with the lowest resistivity as it increases the density of holes. The advantage of this doping is, as said previously, the possibility to add a nitrogen flow in the chamber with a regular cuprous oxide target inside. Other doping materials are possible such as gallium, sodium, nickel, and so on

2.9.4 Post-annealing

Sample annealing is common for cuprous oxide as it enhances the electrical properties by increasing the crystallinity [27]. This can be done under different gas atmospheres such as oxygen, air, nitrogen, or vacuum. The difference between oxygen and air is pretty minor [21]. It has been shown that there is a certain threshold temperature for each of these gases. Pass this temperature, the film tends to oxidize with air and oxygen and loses its oxygen with nitrogen and a vacuum atmosphere. For nitrogen atmosphere, it is shown later in this work and for vacuum, it is reported by Umar *et al.* in [28]. When done properly, annealing increases the carrier mobility and increases the crystallinity by increasing the gain size [29].

2.9.5 Interface defects

Cuprous oxide is known to have quite a lot of defects at the interfaces. This has a big impact on solar cell efficiency. This loss of efficiency comes from the too-high recombination losses between the cuprous oxide and its neighbors [30].

Hence, the idea of introducing a buffer layer in the cell to reduce recombination losses is developed with oxides such as TiO_2[12], ZnO[31] or Ga_2O_3 [10].

2.9.6 Juntions with n-type metallic oxides

As stated in the introduction of this work, there a several options of n-type TCOs. To name a few, there are zinc oxide, Al-doped zinc oxide (AZO), titanium dioxide, and gallium oxide.

Gallium oxide is a possible promising n-type material for solar cells due to its high energy band gap but lower electronic affinity than the usual ZnO [32]. Moreover, it is used undoped, which makes it easier to work with compared to other n-type TCOs [10]. Here, the interested phase is $\beta-Ga_2O_3$ as this phase is the stablest of all the others [16]. Its lattice can be seen in Figure 2.17.

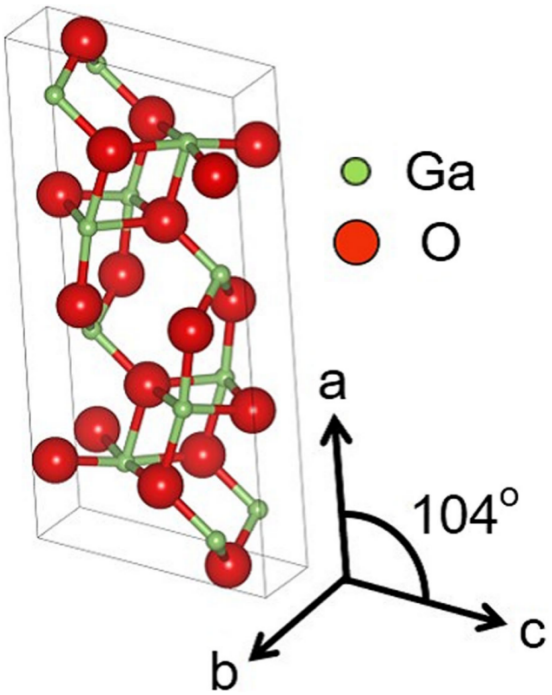

Figure 2.17: β-Ga_2O_3 lattice ($a = 12.2$ Å, $b = 3$ Å, $c = 5.8$ Å) [33].

The films are easy to make at room temperature and are economical as it is only a binary compound with oxygen and can be mass-produced, compared to other wide-gap semiconductors. Moreover, it is very stable, physically and chemically. Its deposition process is the same as cuprous oxide with RF sputtering but here, it is non-doped and no nitrogen is needed but oxygen.

2.10 Availability of the materials

2.10.1 Copper oxide

As copper oxide in Cu_2O phase was one of the first semiconductors to be discovered, it is a well-known solution for a low-cost solar cell with a theoretical efficiency of 20 %. Even though it does not have the highest efficiency, its transparency makes cuprous oxide a promising metallic oxide to make transparent solar cells. It has some advantages compared to silicon as it is non-toxic, it is a *p*-type metallic oxide, only binary and naturally formed. But most importantly, copper is very abundant in the soil. However, the abundance of copper does not mean the ease of extraction and the cleanliness of the production. The production of copper, as described in [34], requires open-pit mines, acidic solution, electrowinning, and so on. These processes are not very clean. Solutions are currently developed to recycle copper. The most advanced technique nowadays uses catalytic etchants as shown by Zante *et al.* in [35]. Their method has the advantage of not using acidic solvents. However, if one wants to recover copper and gallium up to 100 %, the leaching processes using acids are inevitable. As shown by Kavousi *et al.* in [36]. This kind of process is still in development and not cost-effective but going in this direction and having a clean method is the key.

To understand the need for better copper oxide production, one can see the growth rate of demand for copper in the world. The demand in 2021 was 290 billion USD and is expected to be 476.9 billion USD with a growth rate of 5.1 % every year (Data from [37]).

2.10.2 Gallium oxide

As the high-tech product demand is constantly increasing, the demand for power electronics with better efficiency and lower cost increases too. One promising way is to replace the silicon, widely used nowadays, with materials with a higher band gap. These materials, as shown in this work for gallium oxide, can give high performance. The market is expected to grow by 44.1 % by 2033 according to [37]. Even if the technology is as good as it needs to be, the resources are not abundant. European and Chinese projects try to improve the development of such materials but these are hard to find on earth.

The gallium oxide is not found pure in the ground and needs to be refined to use it. Currently, 90 % of the gallium production comes from the production of Zinc and alumina. Such a process is not sustainable and recycling projects are not yet to be working on a large scale. As shown by Maarefvand *et al.* in [38], processes for recovery of gallium in LEDs are developed with chemical treatments and so on.

While gallium oxide is very promising for its electronic applications with lower power consumption, if the market growth continues, it is important to also develop the production and the recyclability of the devices made of gallium oxide.

2.10.3 Global need of solar cell

To summarize, as politics tend to go toward renewable and cleaner ways to produce energy, it becomes more and more important to consider solar cells as a big part of the new energy

field. However, the required compounds (copper and gallium) need to be also renewable to guarantee a real gain.

Chapter 3

Tools and methodology

This chapter aims to show the different experimental techniques available in the lab and how they are used throughout this work. A brief introduction to each technique is made with typical results. Then, the fabrication part starts with Schottky devices and their first electrical measurements. With these samples, two types of annealing are compared and criticized to enhance the film quality. To finish, several unexpected behaviors with the metallic contact are discussed.

3.1 Experimental tools

3.1.1 Thin film deposition

To deposit thin films in the laboratory, two techniques are chosen. One allows us to deposit films of a tenth of a micron for semiconductors and insulators for example. This is radio frequency sputtering (RF sputtering). The second allows for the very easy deposition of metals of tenths of microns, namely thermal evaporation. Both techniques are used to fabricate the studied Schottky device.

Radio Frequency Sputtering

The RF sputtering consists of a small target of bulk on which an argon cloud is excited by an RF electric field. This high level of energy excites the argon and makes a plasma. Atoms from the target are thus detached by the plasma and those atoms in suspension travel in the chamber and deposit everywhere, thus also on the sample. This movement of particles in suspension depends on the mean free path of the particles themselves. This mean free depends on the quality of the vacuum as the lower the inside pressure, the larger the mean free path. This explains the required vacuum inside the chamber to guarantee a deposition and a film deposited without defects from the air. This allows the production of samples from 10 nm up to 400 nm. The deposition rate can vary from 0.008 nm/s to 38 nm/s. However, making samples with compounds that have never been used in the laboratory induces a calibration phase. Each RF sputtering machine has its specificities and a recipe must be developed with the right argon pressure and flow, the right power, and so on.

Thermal evaporation

The thermal evaporation allows us to deposit thin film of $\approx$ 200 nm of metals such as gold or silver. The machine consists of a small tungsten crucible (as its fusion temperature is very high) on which the metal pellet one wants to evaporate is put. Under vacuum, a high current is passing through the crucible. Thanks to the Joule effect, the crucible becomes hot enough to evaporate the pellet in the chamber and hence, on the substrate above it. This technique only works for specific metals, depending on their fusion temperature. It can be used for metals such as gold, aluminum, and silver.

3.1.2 Structural analysis

To be able to characterize the structure of a certain film, X-ray diffraction measurements can be used. This technique allows us to determine the phase of a film or to measure the grain properties of the surface of a film, for example.

X-ray diffraction measurements

One way to find whether the deposited film is in the right crystalline phase is by doing X-ray diffraction measurements (XRD). This works as follows, the machine sends a beam of X-ray with a known angle $\omega = 1$ degree on the surface of the film. As X-rays have a wavelength of the same order as the distance between crystalline atoms, the beam is diffracted. Hence, a sensor, being at a variable angle, receives the diffracted beams for certain angles. Then, we are provided with a curve of the intensity measured with respect to the angle of diffraction. The intensity has no units and is only returned by the machine by a "count" of this intensity. It is then easy to compare this curve with the literature to determine whether it is, for example, Cu_2O or Cu_4O_3. These exact peaks from the literature are measured from compounds in powder form where they exhibit all the possible peaks for all lattice directions [39]. Then, these exact peaks are used to compare the phase of any film. A simple representation is shown in Figure 3.1. A typical XRD scan is shown in Figure 3.2. This sample is indeed a

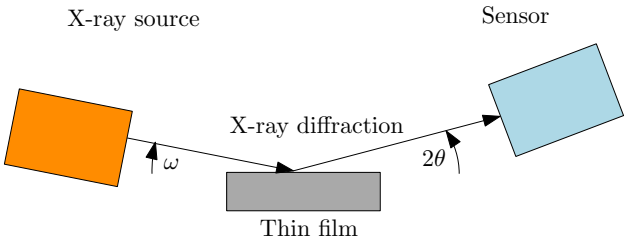

Figure 3.1: Schematic of the X-ray diffraction measurement.

Cu_2O sample as the theoretical peaks of the lower plot in Figure 3.2 are at the same angle 2θ at the peaks in the XRD pattern, in 36, 42, and 61. Moreover, the XRD pattern can have more peaks if several phases of a compound and different materials are present at the surface of the sample. There is then an uncertainty in the phase.
Additionally, the higher the peak, the more present the phase is. Furthermore, if the peak

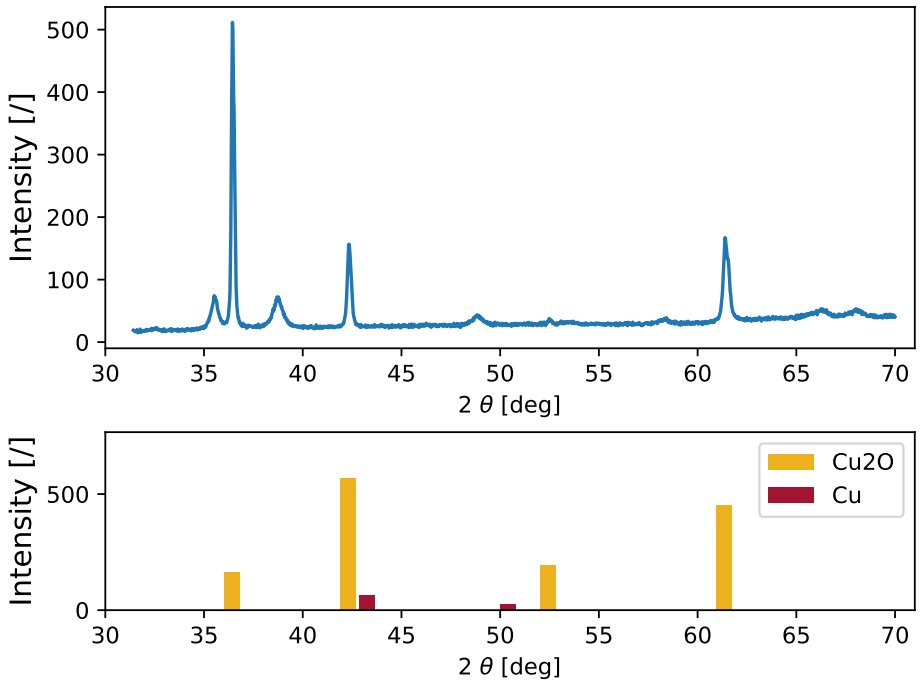

Figure 3.2: **Upper graph**: Typical XRD pattern of a Cu_2O sample. **Lower graph**: Exact peaks from XRD measurements of powder for Cu and Cu_2O.

is very thin, it means that the sample is very crystalline because the lattice constant is the same everywhere.

3.1.3 Electrical measurements

To measure the electrical properties of a film such as the mobility, resistivity, and so on, electrical measurements are needed.

Van der Pauw measurements

To measure the resistivity of a thin film, a square sample is required. Thanks to its square shape, a potential across the diagonal is applied as shown in Figure 3.3.

If the current is also known, by using Ohm's law, the sheet resistivity is found and is defined with the square shape property. The maths of determining the sheet resistivity with the measured resistances of each 2-point configuration are not detailed here but well by Geng *et al.* in [40]. The resistivity is thus given by

$$\rho = R_s t, \tag{3.1}$$

where t is the thickness of the sample and R_s is the measured resistance. To have a better value, the measurements are averaged with different corner combinations.

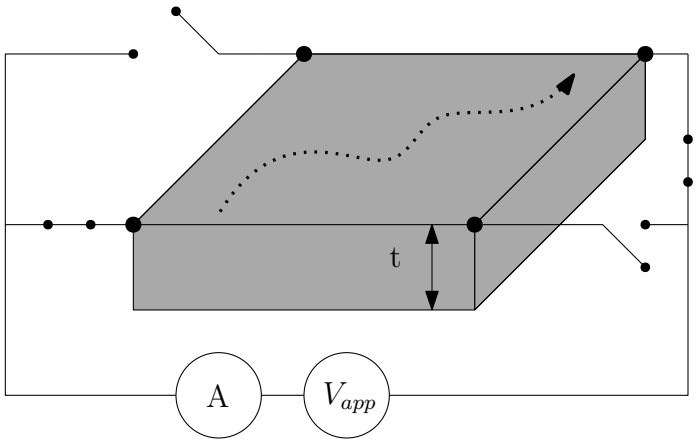

Figure 3.3: Scheme of the resistivity measurement using Van der Pauw technique.

Hall effect measurements

The Hall effect is the creation of a transversal potential across a thin film. This potential exists when a current is passing along the film (from left to right) with a normal applied magnetic field. The latter causes the charges to drift and accumulate on both the front and back sides of the film. Hence, it induces an electric field. This is illustrated in Figure 3.4.

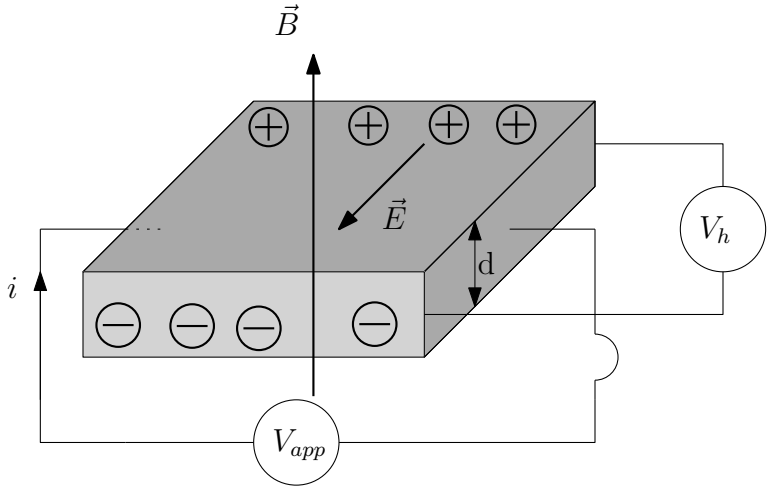

Figure 3.4: Setup of the Hall measurements for an n-type conducting material.

The charge equilibrium induces the following relation:

$$\frac{1}{\rho} = q(\mu_n n + \mu_p p).$$

As the films are p-doped, the minority carriers are neglected. A relation between the majority carriers and their mobility for an p-type material for example is found with

$$\frac{1}{\rho} = q\mu_p p. \tag{3.2}$$

Moreover, the Hall potential due to the electric field gives for an n-type

$$V_h = \frac{iB}{pqt}. \tag{3.3}$$

Hence, from the resistivity measured by Van der Pauw and the majority carriers density n with Equation 3.3, one finds the mobility by Equation 3.2.

3.2 Film fabrication

This section aims to show how the metal-semiconductor device is fabricated and what are its properties. To start with, the device is shown in Figure 3.5.

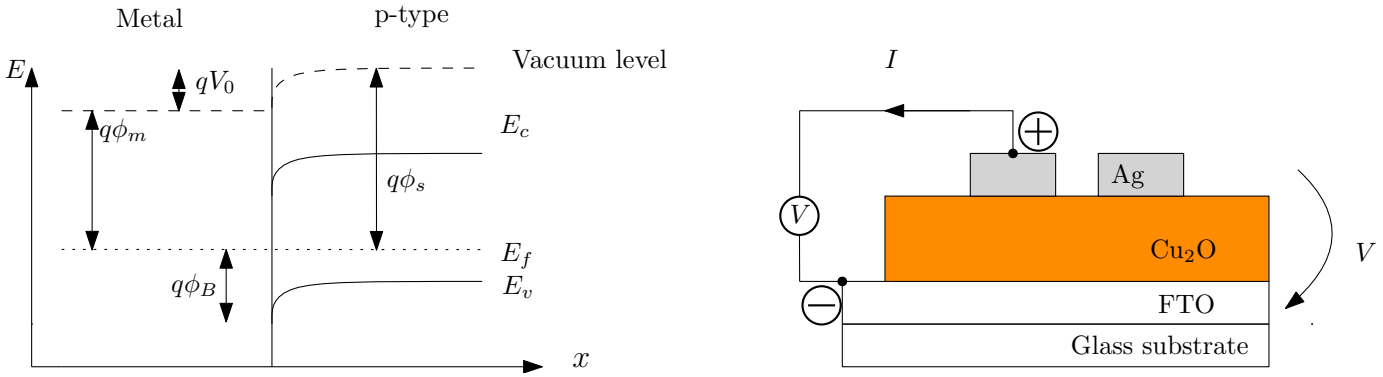

Figure 3.5: **Left**: Energy band diagram of the Schottky contact between a metal and a p-type semiconductor. **Right**: Diagram of the experimental setup for the Schottky I-V curve.

- The fabrication starts with a FTO (Fluorine-doped Tin Oxide) coated glass. The FTO being conductive, plays the role of the back contact. Its resistivity is assumed very small compared to copper oxide. And the contact between the FTO and the copper oxide is ohmic.
- The layer of copper oxide is deposited via RF sputtering. The deposition parameters are given in the following:

Thickness	Argon pressure (Plasma gas)	Temperature	Power	Ar flow	N_2 flow	Chamber pressure
200 nm	$6.66 \cdot 10^{-3}$ mbar	22°C	23 %	20 sccm	16 sccm	$2.67 \cdot 10^{-7}$ mbar

Table 3.1: RF sputtering deposition parameters for N-doped cuprous oxide thin films.

This recipe of copper oxide is well known in the lab and yields a p-type semiconductor with properties of Table 3.2. These measures are made using Van der Pauw and Hall techniques.

Resistivity	R_{sheet}	Majority carrier concentration (p)	Majority carrier mobility (μ_p)
6.14 ± 0.03 Ωcm	$(2.73 \pm 0.02) \cdot 10^5$ Ω	$(2.5 \pm 1.7) \cdot 10^{18}$ /cm^3	0.69 ± 0.46 cm^2/V·s

Table 3.2: Electrical properties for N-doped cuprous oxide thin films.

During this work, no Mg doping has been used but nitrogen. This choice is made because it has been seen in the lab that doping with nitrogen was easier, more effective, and gives higher carrier concentration. The flow of nitrogen has been optimized to guarantee the right copper oxide phase with the best doping. The mobility is very low compared to the example in the literature. It is shown in [41] that having a deposition at room temperature of copper oxide via RF sputtering lowers mobility. For the rest of this work, the values in Table 3.2 are used.

- The last step is to deposit small pads of silver on the cuprous oxide. Silver is a metal that, in theory, has a rectifying contact with the copper oxide which is what is aimed for the measurements. The aim is to make a series of CV measurements of the Schottky device to extract a density of acceptor at the interface. This technique is fully explained by Schroder in [42]. It works by applying a variable voltage along the junction. This changes the depletion width and thus the capacitance. From the capacitance, one finds the density of acceptors in the depletion region of the cuprous oxide film, hence, the interface. The silver is deposited via thermal evaporation. The chamber pressure is at $5 \cdot 10^{-6}$ mbar and a pellet of 233 mg are evaporated.

Finally, the final device is shown in Figure 3.6. One can see the small square corresponding to the silver pads, the typical copper color, and the transparent FTO back contact.

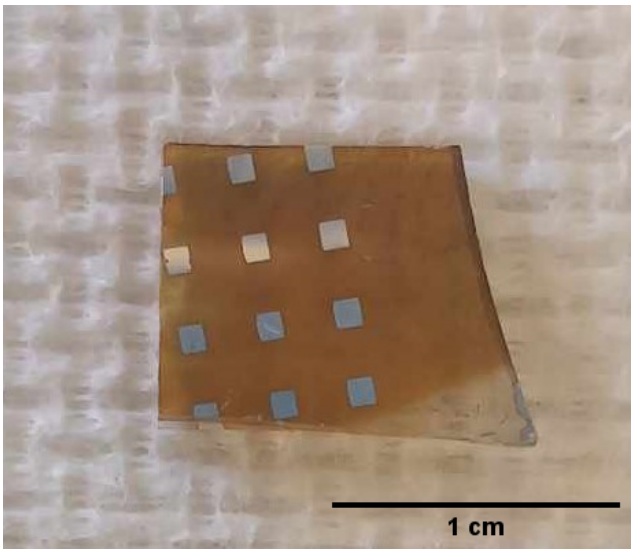

Figure 3.6: Photo of the fabricated sample of Cu_2O and silver pads on the FTO substrate.

3.2.1 Four types of samples

First, four types of samples are fabricated following the same protocol as described above. They are made from:

- a target A of CuO without thermal annealing (TCuO-NA),
- a target A of CuO with thermal annealing of 25 min at 200° (TCuO-A),
- a target B of Cu_2O without thermal annealing (TCu2O-NA),
- a target B of Cu_2O with thermal annealing of 25 min at 200° (TCu2O-A).

This variability of the targets comes from the supplier. However, while the targets are different, the deposited phase with the nitrogen flow in the sputtering chamber is Cu_2O for both targets. This can be checked in the XRD analysis for the four samples.
Additionally, they exhibit the same electrical parameters.

This choice of four samples is mainly due to a change in the supplier. The old targets were Cu_2O and the work has been initialized with those, however, the new targets provided exhibited a CuO phase but Cu_2O once deposited. Hence, the work has to be articulated on these two targets.

3.2.2 Annealing effect

It has been shown in the literature that thermal annealing improves the crystallinity of the films and thus, the electrical properties [27], [43]. Having a better crystal can give better contacts by reducing interface defects [27]. For those reasons, two different annealing are tested.

To test the effect and the process of the annealing, samples are fully fabricated and then cut into two pieces just before annealing and only one is annealed. This reduces the experimental variability.

Hard annealing

At first, a sample TCu2O-A is annealed under nitrogen atmosphere for 20 min at 450°C. This value is just 50°C larger than the highest temperature used by Bunea *et al.* in [21]. Because the temperature is a bit larger, it is annealed for less time. Both annealed and not-annealed samples are then electrically analyzed. As it turns out, the sample without annealing TCu2O-NA is non-ohmic, and the annealed, TCu2O-A, which should have a better crystallinity is undesirably ohmic. To know why, the two samples have been analyzed via XRD measurements.

Note that the analyzed zone is not only the cuprous oxide film we are interested in, but also the FTO, under it, and the silver, on top of it, but a conclusion can be drawn. The results are shown in Figure 3.7. The lower graph shows the known peaks for each phase in the measured samples. The upper graph shows the XRD pattern of the two samples with and without annealing. As can be seen for the sample with annealing, there are additional peaks, at the same angle as the pure copper. These are visible in $2\theta = [43, 50, 74]$ degrees.

This means that the annealing removed some oxygen in the copper oxide which leads to a Cu phase and the loss of the rectifying behavior. Hence, slower and cooler thermal annealing is to be considered. This behavior has already been pointed out by Umar *et al.* in [28]. They

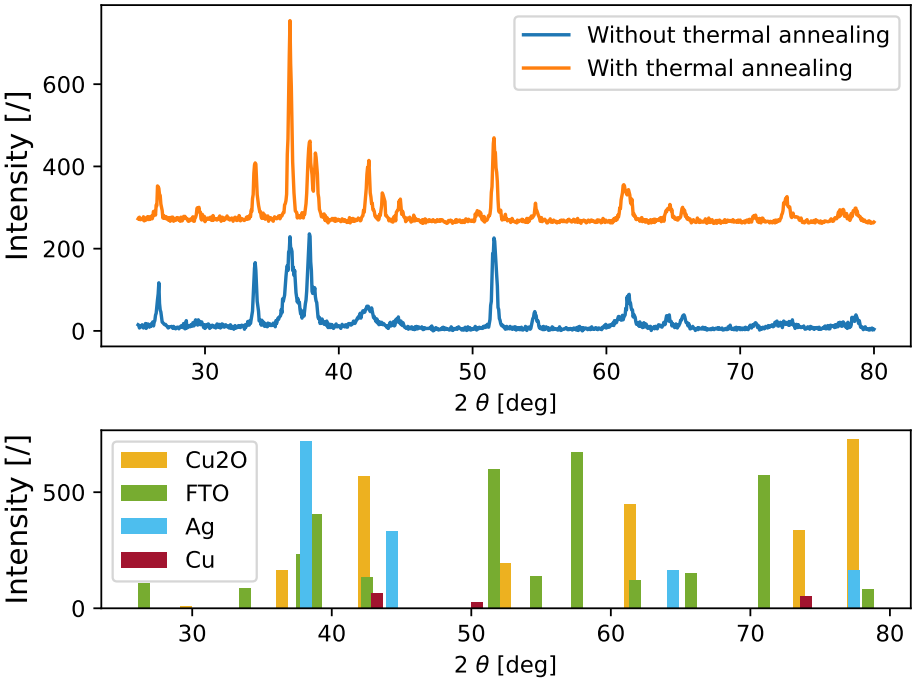

Figure 3.7: **Upper graph**: XRD pattern of the Schottky device without and with annealing of 450°C for 20 minutes under N_2 atmosphere for TCu2O-NA and TCu2O-A. **Lower graph**: Exact peaks from XRD measurements of powder for FTO, Ag, Cu, and Cu_2O.

concluded that a certain temperature threshold was exceeded. Thus, a longer with lower temperature annealing must be considered.

Soft annealing

Because the hard annealing did not provide us with non-ohmic behavior and because an undesired pure copper phase appeared, another annealing process was introduced. It is expected that this annealing does not give a pure copper phase but increases the electrical properties with a non-ohmic behavior. To remind the reader, the films are made using both CuO and Cu_2O targets but once deposited, the films are only Cu_2O.

The annealing process consists now of a heating of the sample for 25 min at 200°C under a nitrogen atmosphere. A temperature in the lower range of Bunea. This soft annealing aims to enhance the crystallinity to have a non-ohmic behavior and no copper phase appearing. As desired, it is shown in Figure 3.8 that the lower temperature prevents the formation of pure copper but increases the crystallinity. It can be seen that at $2\theta = 37$, the Cu_2O peak is more than two times higher and thinner for the annealed sample. Having such peaks means that the crystallinity is enhanced [27].

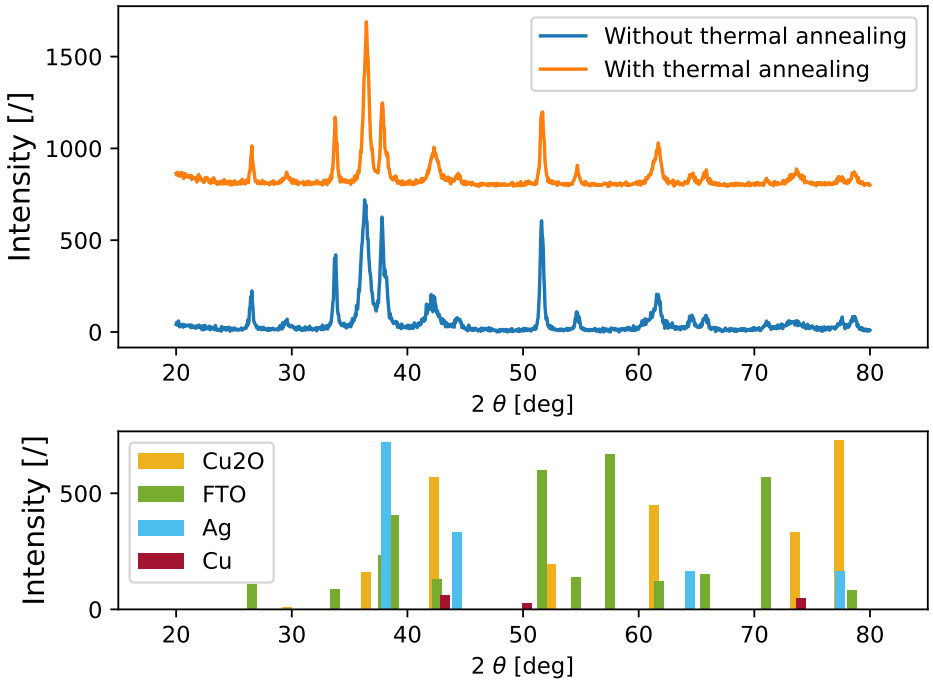

Figure 3.8: **Upper graph**: XRD pattern of the Schottky device without and with annealing of 200°C for 25 minutes under N_2 atmosphere for TCuO-NA and TCuO-A where the target is made of CuO but all the deposited film are made of Cu_2O. **Lower graph**: Exact peaks from XRD measurements of powder for FTO, Ag, Cu, and Cu_2O.

Hence, this soft annealing is applied to TCu2O-A and TCuO-A samples and the hard annealing is no longer considered. This annealing allows to us see during further measurements if the crystalographic structure does change the electrical properties considerably. Moreover, because the metallic contact on cuprous oxide can be difficult, the annealing could enhance this contact as seen in the latter.

3.2.3 Crystalline orientations

From the previous XRD measurements, the main crystallographic texture can be determined. To help understand the following explanation, a diagram of the crystal facet orientation of a compound is given in Figure 3.9.

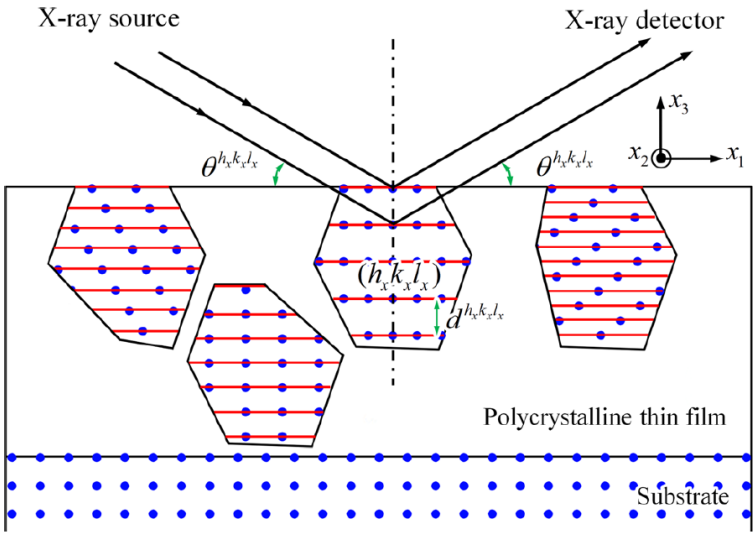

Figure 3.9: Diffraction of X-rays on the crystalographic planes for each region in a polycrystalline thin film. [44]

As can be seen, each grain has its own orientation. For example, because the Cu_2O lattice is cubic, one can visualize more easily how a cube can have a specific orientation to give different tangential planes. The constructive interferences from the reflected X-rays on the tangential planes give peaks at specific inter-plane distances d. As seen in Figure 3.9, the distance depends on the orientation. From these measurements, it is found that the higher the peak of a specific grain orientation, the higher the proportion of the related crystal facet.

One can identify which peak corresponds to which lattice direction. This is made in both [19] and [45]. The same process is made in this work. The directions for each peak for cuprous oxide are taken from the previous papers and displayed with the results. These lasts are shown in Figure 3.10.

As can be seen, the grains in the cuprous oxide have preferential directions. Note that only the visible peaks are given. There is no peak in the XRD pattern in 52° where it should correspond to a peak of the (200) phase. The more present peaks are (111), (200), (220) and (222). This means that from the surface scan, there are more grains in the (111) direction than (311) for example. As there is not only one phase, this means that overall, the film is quite anisotropic. This result has already been reported by Akkarii *et al.* in [46].

One interesting thing is that the film is not a fully random-oriented polycrystalline, nor textured with only one or two phases. Here, it has preferenced orientations and a dominant texture (111) but nearly all the phases are appearing, thus making it polycrystalline. One can nearly see a peak in every direction, this is normal for polycrystalline, but some are much higher than others, which is normal for a textured film. This reasoning is guided by

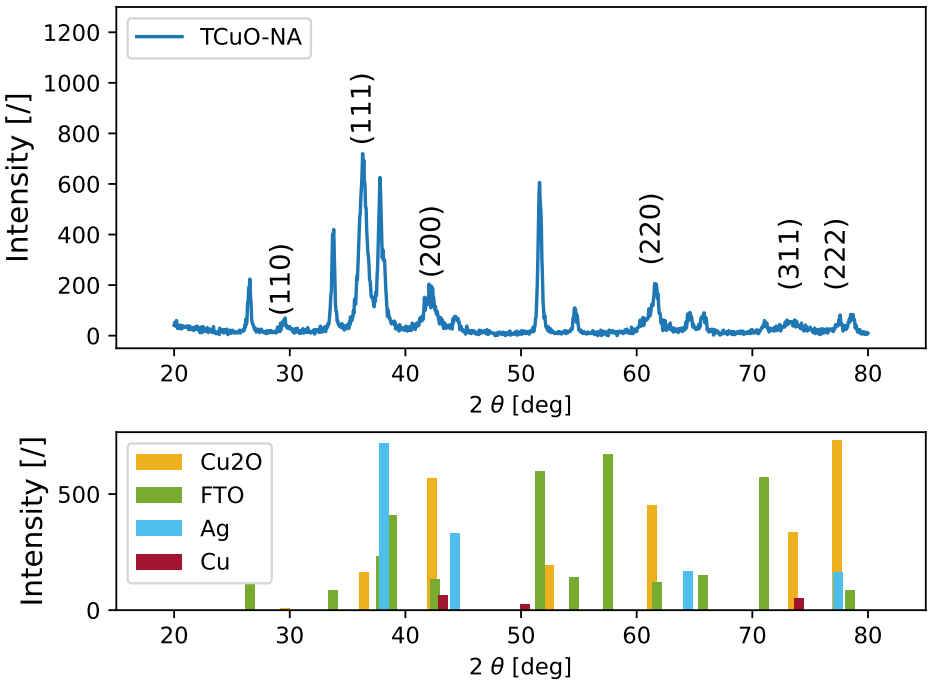

Figure 3.10: XRD spectrum for TCuO-NA sample with the cuprous oxide direction phase peaks.

the explanation from Harrington *et al.* in [39].

However, care must be taken, as the XRD pattern is done with other compounds. As said earlier, having FTO and Ag peaks in the XRD spectrum reduces the certainty. Some peaks, such as (222) can also be due to the silver phase. But it can be said that either the (222) peak is Ag or Cu_2O. As it is very small, this peak and this orientation are negligible. The peaks that are very present with a high intensity do not leave any doubt on being Cu_2O.

Here, in the case of our film, the mix between a random polycrystalline and a textured one is not clear. In both cases, there is then not a real strong preferential direction, hence a strong directional dependence for the mobility. This will be validated with the in-plane (Van der Pauw) and the transversal mobility in the latter.

3.2.4 Silver analysis

To start with, the choice of silver is motivated by the desire to have an easy deposition via thermal evaporation with a metal, that in theory, has a rectifying contact with the Cu_2O. The work function of silver is approximately 4.5 eV [47] and the one of Cu_2O is approximately 5 eV [48]. The condition of a rectifying contact with a *p*-type, being that $q\phi_m < q\phi_s$, is fulfilled for compounds in theory. Here, the work functions may differ from the center of the film or the interface. Hence, the condition may be fulfilled in theory but not in practice.

Silver has already been deposited on cuprous oxide by Pham *et al.* in [49] and in [50] and [51]. These articles study effects using the combination of Ag/Cu_2O with nanoparticles but no electrical properties. They did not study the electrical contact of two thin films via thermal evaporation to find a rectifying contact. Thus, knowing that the contact is possible, it is then investigated in this work as it has not been done. Note, that it has been checked that the cuprous oxide was thick enough to guarantee a depletion region smaller than the Cu_2O thickness.

I-V motivation

Before any first electrical measurement on the fabricated device, it is worth explaining the role of I-V curves. This type of measurement aims to determine the type of contact: ohmic if the curve is linear, rectifying if the curve has an exponential shape or a different shape for another model. Finding the right type of contact and the corresponding I-V law helps us characterize the cuprous oxide by fitting the curve with a given model.

However, fitting a model to I-V curves does not just allow for an interface characterization. Indeed, most of the measurement techniques work with a plane analysis such as XRD, and Van der Pauw. Here, the I-V curve is a scan of the core of the film from top to bottom. The current flows transversely and gives information that could not have been measured with our equipment, such as the transversal mobility of the film.

Depending on the model of current conduction, one can extract from I-V curves parameters such as the metal-semiconductor barrier height, the density of the majority of dopants, and so on. The measures are made using a Keithley 2450 SourceMeter with small tungsten needles as shown in Figure 3.11.

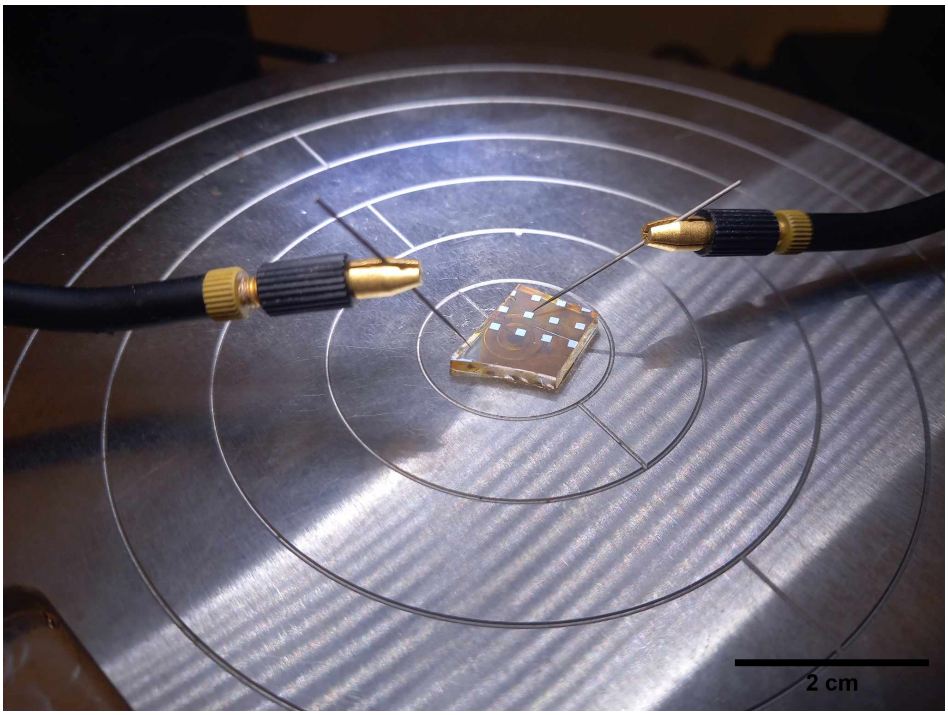

Figure 3.11: Experimental protocol picture of the two electrodes for the silver-cuprous oxide contact.

Electrical response on Ag/Cu_2O contacts

When the first I-V curves are measured from the FTO to the silver pad, the curves are linear and not exponential.

One expected Schottky contact with the silver and the cuprous oxide, however, all samples TCuO-NA, TCuO-A, TCu2O-NA, and TCu2O-A have been fabricated and measured but every time, the current was purely ohmic as shown in Figure 3.12. This means that while the annealing process enhanced the crystallographic properties, it is not useful for the silver-cuprous oxide contact. From this curve, a resistance of around 40 Ω is extracted.

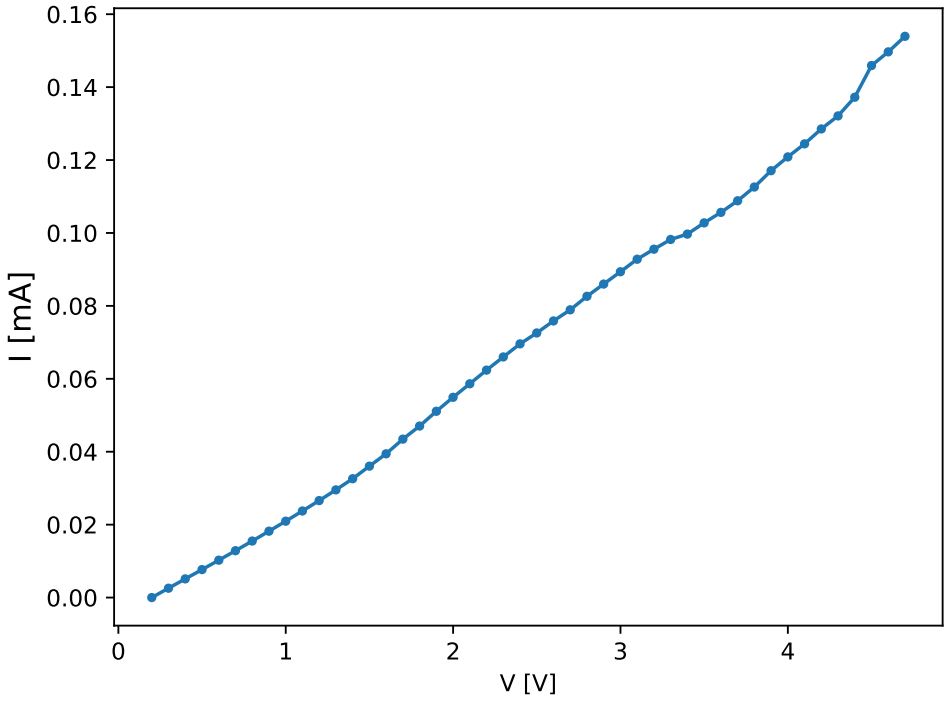

Figure 3.12: Ohmic I-V curve of sample TCu2O-A of the silver short circuit through the cuprous oxide.

To understand this ohmic behavior, one can measure the resistance of the FTO and the transversal cuprous oxide with an ohmmeter. The expected current path is shown in Figure 3.13.

The measured resistance via the Ohmmeter between two points of the FTO substrate is of the order of 15 Ω, which is expected with its resistivity of approximately 10^{-4} Ω·cm [52]. The transversal resistance is measured. However, it is measured directly on the cuprous oxide and not the silver pads and the FTO. Thus, the total resistance is given by the sum of the resistance of the FTO (R_{FTO}) and the Cu_2O (R_{Cu_2O}): $R_{FTO} + R_{Cu_2O}$. The measured value is of the order of the kilo ohm. This means that the transversal resistance of the cuprous oxide is much larger than the FTO. This is also validated as the resistivity of the cuprous oxide measured in the lab is around 0.5 Ω·cm.

From these results, it can be concluded that when the current passes from the FTO to the

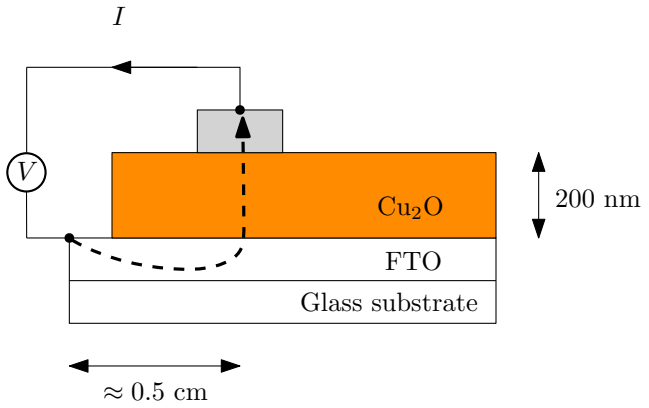

Figure 3.13: Representation of the expected current flow from the FTO to the silver pad.

silver pads (pad with its resistance R_{Ag}), the total resistance should be: $R_{FTO}+R_{Cu_2O}+R_{Ag}$. Here, because R_{Cu_2O} is approximately 1 kΩ, and the FTO and silver are more conductive than cuprous oxide, the total resistance is expected to be of the order of the kΩ. However, the total measured resistance is of the order of 10 Ω. It is the same order as if only the FTO and the silver resistances were measured. Thus, it behaves as if the current is not passing through the cuprous oxide.

One hypothesis is that there could be a parasitic channel of silver that passes through the cuprous oxide. The silver would act as a short circuit and this would explain the low resistance ohmic behavior. This short circuit could be explained by the high porosity of the cuprous oxide. A small line of silver could pass through it. Then, there is a diffusion as shown in [50].

To overcome this problem, annealing before the silver deposition has been tried to increase the crystallinity and thus decrease the silver diffusion but in vain, the same ohmic curve is obtained. This was expected as it has been shown by Umar *et al.* in [28] that the annealing process increases the size of the grain but also the porosity.

The silver short circuit hypothesis is consolidated by the fact that Cheng Siah *et al.* in [53] have managed to have good contact between the silver and the cuprous oxide. This means that they did not have a short circuit and that it is possible. The question is to find out what is the issue for the samples.

Note that we were expecting rectifying behavior but Cheng Siah reported that silver has an ohmic contact with N-doped Cu_2O. This is discussed in the next chapter.

Hence, from these results and analysis, it can be can concluded that the silver deposition on the cuprous oxide is not working as expected. Hence, an alternative must be found. This is done in the next chapter where another metal is studied, namely, tungsten. The aim is to run the same experiments done with silver but with tungsten. Additionally, it could be interesting in another work to deposit thicker cuprous oxide films with soft annealing. This could maybe prevent the silver deposited by thermal evaporation from making a short circuit to the FTO back contact.

Chapter 4

Electrical characterization of Cu_2O contacts

This section ultimately aims at determining the physical parameters of the cuprous oxide films fabricated in the laboratory. An alternative to the silver-Cu_2O contact is determined and studied via the appropriate model on the I-V measurements. This metallic contact offers some pros and cons. Then, once the model is correctly fitted to the measurements, approximated cuprous oxide parameters are extracted such as the hole transversal mobility, the acceptor density, and the concentration of holes at thermal equilibrium.

4.1 Cuprous oxide interface defects model

4.1.1 Tungsten probe, a silver alternative

Because the silver contact has been tried many times with TCuO-NA, TCuO-A, TCu2O-NA, and TCu2O-A without success, an alternative must be found. The replacement is tungsten. This choice is guided by the literature which is quite sparse with only two known references. It could interesting to bring something new. The only known effect between cuprous oxide and tungsten are for a cell tungsten oxide - cuprous oxide [54] and the use of tungsten as a back contact for the zinc oxide - cuprous oxide cell [55]. Additionally, the work function (in ideal conditions) provides a rectifying behavior as tungsten's work function is lower than the one of cuprous oxide [56]. However, Azanza *et al.* in [55] use tungsten as an ohmic contact, not the desired rectifying. This will be discussed later.

Tungsten has been investigated as a metallic contact on the cuprous oxide. We can implement such contact by using the tip of the probe station of the laboratory.

The advantage of this technique is that it does not require a tungsten deposition. There are no risks of diffusion of the tungsten inside the cuprous oxide film. This is also very easy as it is only a contact with a precision tip. The downside of the use of a tungsten probe is that the contact area is not very precise. The manufacturer provided us with needles with a spherical head of 0.35 μm in diameter but as the needles are used, they get wider. An error in the contact area must be taken into account. Moreover, the needle can be pushed

too hard on the film, thus increasing the contact area but increasing the uncertainty. To avoid this effect, the protocol for approaching the needle is the following. An ohmmeter is connected to both needles: one on the FTO contact behind the cuprous oxide and one on the cuprous oxide which is approached slowly towards the film. As soon as the ohmmeter reads something and a current flows, the needle is fixed. This gives a certain reproducibility in the measurements as each measurement will be made with the same needle contact pressure and area.

4.1.2 Tungsten probe measurements

The I-V curve is then measured for the four samples with a tungsten electrode on the FTO and a tungsten electrode on the cuprous oxide.

Moreover, to test the reproducibility of the I-V curves and the effect of voltage soaking, Figure 4.1 can be analyzed. The probe touching the Cu_2O is placed at one point of the cuprous oxide for 2 I-V curves one after the other. Then, the probe is placed at a different point and 2 other I-V are taken. Thus, there are 4 I-V curves from 2 different points of the same sample. The studied applied potential is restricted to positive voltage as the measured curves were odd functions and the later-used model only requires positive voltage. Thus, there is no need to measure the negative voltage part. Here, it can be seen that the curves keep

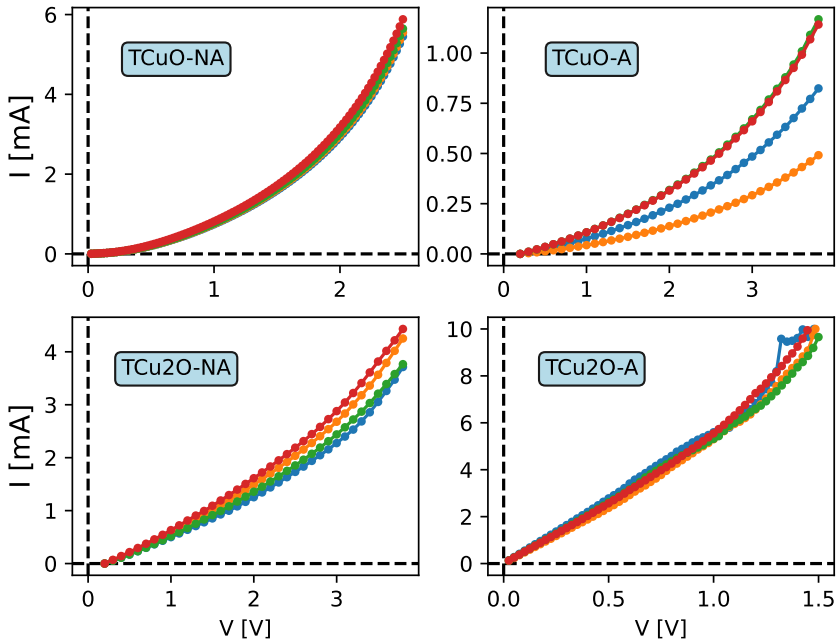

Figure 4.1: I-V curve of the tungsten probe-cuprous oxide contact for the four types of sample (Cu_2O or CuO target and annealed (A) or not annealed (NA) sample). Four measurements for each sample are made and are plotted in their respective sample subplot.

the same shape for each sample and that there is not one order of magnitude of difference between the curves of a sample. This means there is no impact on the polarising of the

measurements. One downside is that the sample TCuO-A has a small variation and then sits to have the red and green curves. There might be an impact on the polarisibility of the sample and then a stabilization.

From Figure 4.1, no ohmic, nor rectifying behaviors seem to be visible. This is an issue as a rectifying behavior was expected. Although the theoretical work function of tungsten should give a rectifying behavior with the cuprous oxide. Both respective work functions may vary.

The concept of work function only takes place in the context of the Schottky-Mott rule. It has been seen many times that the concept of work function does not hold very often and the work function in the bulk is much different at the interface. It has been seen in [57] and [47] for example that even the crystal orientation changes the work function.

It is then not surprising that the I-V is not rectifying as the work functions may not satisfy the Schottky condition at the W (tungsten)-Cu_2O interface. This non-rectifying behavior is observed by Azanza *et al.* where they use tungsten as an ohmic back contact with Cu_2O [55].

Hence, it is needed to find the right model to understand the I-V behavior of the samples.

4.1.3 Drift/diffusion model

The most known model is the one that has been introduced to understand the mechanism of the *pn* junction: the drift/diffusion model. The charge carriers are microscopically modeled as classical particles. Then, the current of carriers is modeled by two mechanisms: the drift due to electric fields and the diffusion, due to gradients of charge concentration. This model has already largely been discussed in the theoretical reminder and is the basic semiconductor model.

4.1.4 Shockley model

The second is the Shockley model. It is based on the thermionic emission. When a metal is placed near a semiconductor, there is a natural potential barrier that is formed with the bands. When charge carriers from the metal have an energy higher than the barrier, they pass through the barrier and recombine in the semiconductor. This emission of charge in the metal is characterized by the thermionic current and the diffusion current in the semiconductor. Hence, the total current is written as in

$$I = I_s \left(e^{\frac{qV}{n_0 k_b T}} - 1 \right), \qquad I_s = A^\star T^2 e^{\frac{-q\phi_B}{k_b T}}, \tag{4.1}$$

where n_0 is the ideality factor, $A^\star$ is the Richardon's constant, V is the applied bias and $q\phi_B$, the barrier height. This model gives the previously discussed exponential I-V curve, well known for the Schottky diode.

4.1.5 Space-charge-limited current model

Another charge transport mechanism is the space-charge-limited current model (SCLC). In this model, the current is no longer defined by the movement of charge carriers inside the

crystal but rather by the injected carriers at ohmic contacts at both sides of the semiconductor. This means that the carrier's mobility is much more important than the density of carriers in the compounds. Moreover, the I-V curve thus behaves differently. It is not ohmic, nor rectifying. It has a different curve shape depending on the type and specificities of the semiconductor. One typical I-V curve with the SCLC model for copper oxide is presented in Figure 4.2 by [20].

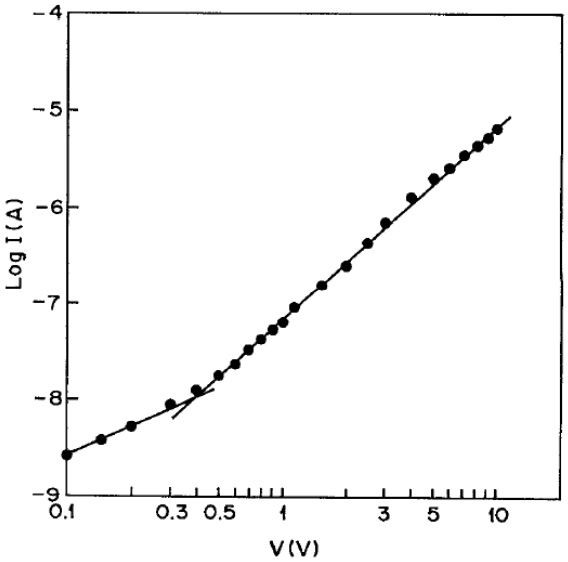

Figure 4.2: I-V curve of electrodeposited Cu_2O (2.6 μm) in loglog scale [20].

First, by taking the SCL model for semiconductors and without traps, from [19], Mott–Gurney law is used:

$$J = \frac{9}{8}\varepsilon\mu_i\frac{V^2}{t^3}. \tag{4.2}$$

The use of this law needs some hypothesis:

- there is only one type of charge carrier,
- constant mobility and permittivity in the semiconductor,
- no electric field at the ohmic contact (thus, no diffusion of carriers at the interfaces with other compounds).

This equation is not perfect as it only works for intrinsic semiconductors and using it with doping must be made with caution. Moreover, no traps in the bulk is a too strong assumption that needs to be taken into account with an additional term. Adding single-level shallow traps can change the slopes of the curve. Additionally, as seen in Figure 4.2, different laws for different applied voltages are expected.

To take traps into account, it has been proposed by Rakhshani *et al.* in [20] to add a ratio to free-to-trapped carriers $\theta(N_v)$, where N_v is the density of states in the valence bands. This additional term gives very good results in Rakhshani's work with nearly perfect fits of the

I-V curves. Equation 4.2 becomes:

$$J = \frac{9}{8}\varepsilon\mu_i\frac{V^2}{t^3}\theta. \tag{4.3}$$

The identification of the model and the fit on experimental curves can provide us with electrical characterization such as the mobility and the majority doping concentration.

4.2 SCL model for cuprous oxide

As has been discussed in [19], [58] and [20], SCL is a model that can be applied to the Cu_2O thin film with metallic contact. Hence, a more detailed investigation is done in the following.

According to Rakhshani *et al.* in [20], the positive part of the I-V curve can be split into two segments: a linear and quadratic part as can be seen in Figure 4.3. The linear part

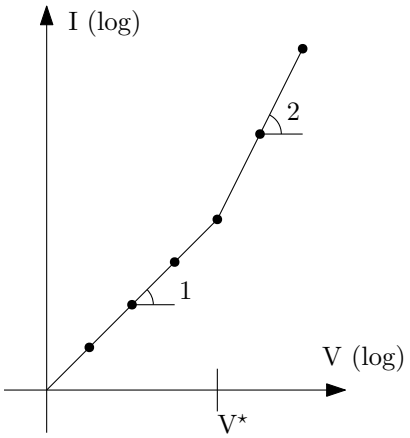

Figure 4.3: Diagram of the log-log I-V curve with two curve fittings and the point of change of slope where 1 and 2 are the slopes of the linear slopes in log-log scale and $V^\star$ is potential where the zones change from one slope to the other.

corresponds to an ohmic current with constant resistivity. Its equation is given as:

$$I = Aq\mu_p p_0\frac{V}{t}, \tag{4.4}$$

where A is the area of the ohmic contact, here, the area of the tungsten probe and p_0 is the hole concentration on the valence band at thermal equilibrium.

The quadratic part is given by the updated Mott–Gurney law with a single-level shallow trap taken into account as previously explained and reminded in:

$$I = \frac{9}{8}A\varepsilon\mu_p\frac{V^2}{t^3}\theta, \tag{4.5}$$

where $\varepsilon = \varepsilon_0\varepsilon_r$, $\theta = G\frac{N_v}{N_a}e^{-(E_a-E_v)/k_bT}$ is the ratio to free-to-trapped carriers with $G = 2$, the acceptor degeneracy factor, N_v, the density of states in the valence band, and $E_a - E_v$, the energy difference between the valence band and the acceptor level. This value has been

measured for N-doped Cu_2O by Lee *et al.* in [59] and Malerba *et al.* in [60] and is 0.12 eV.

The voltage at which the curve changes from linear to quadratic is found:

$$V = \frac{qN_a t^2}{2\varepsilon}. \tag{4.6}$$

4.2.1 Curve fitting and doping concentration

To understand how the model is fitted to the curves, it is first fully detailed for one curve and then, the global results for all the samples are shown.

SCL analysis for one sample

1. The chosen sample is TCu2O-A and the I-V curve in loglog scale is given in Figure 4.4.

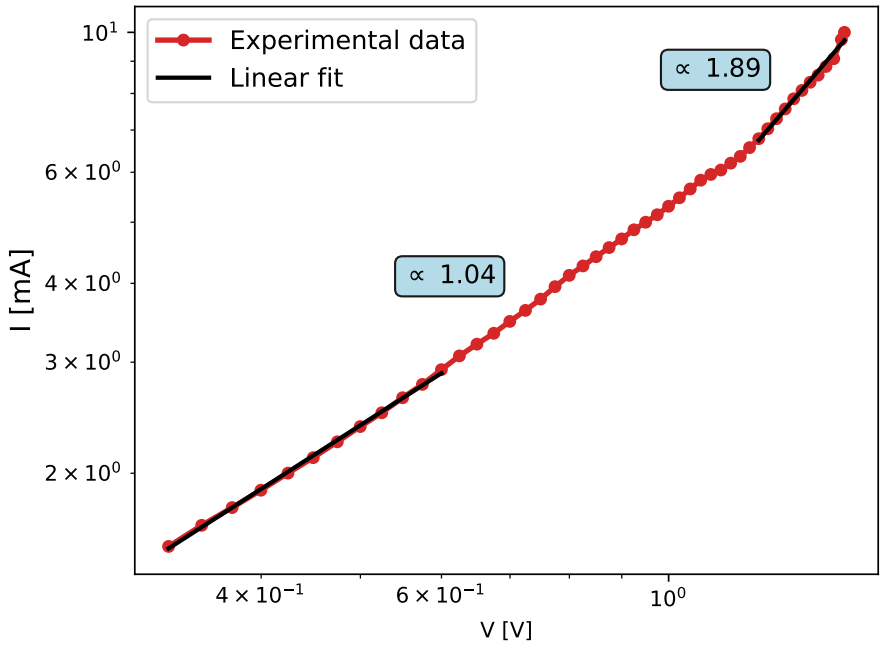

Figure 4.4: Loglog of the I-V curve of the tungsten probe, cuprous oxide contact at one point for the TCu2O-A sample highlighting two power laws where both fits are made at optimal voltage range to find the best slope coefficient. The left slope (1.04) represents the power of the ohmic part and 1.89 is the power of the quadratic part.

2. As can be seen in Figure 4.4, there are two linear zones with different slopes, hence, exponent of V. To have the best slope possible (one closer to 1 and the other to 2), the zones are not next to each other and there is a spacing between them.

3. The first one, corresponding in the SCL model, is the ohmic region $I \propto V$. The chosen segment is V from 0.2 to 0.6 V. A line on this part can be fitted and a slope of 1.04

which is quite close to 1 is obtained.

4. The second linear zone is chosen between 1.2 and 1.5 V. It is expected to be quadratic, so $I \propto V^2$. The slope is 1.89 which is also close to 2.

5. These two slopes are close to what is expected in the model. Having a model that gives a slope of 1 and 2 and a sample that exhibits these same slopes is convincing that the I-V curve follows indeed the SCL model.

6. Hence, from the model, the acceptor density for $V^\star = 1.1$ V with Equation 4.6 is found and this gives:

$$N_a = V^\star \cdot \frac{2\varepsilon}{qt^2} = 2.31 \cdot 10^{16} \ /\mathrm{cm}^3. \tag{4.7}$$

Moreover, from Equation 4.5, one can find the transversal mobility. To do so, the ratio of free-to-trapped carriers, θ with the just-found acceptor density needs to be calculated.

It is given by

$$\theta = G\frac{N_v}{N_a}e^{-(E_a-E_v)/k_bT}, \tag{4.8}$$

where N_v is a parameter that is known and used in the simulations from the next chapter, thus, its value is taken from there and is: $1.34 \cdot 10^{19}$ /cm^3, and $G = 2$ as proposed in [20].

The hole mobility in the film is known via Van der Pauw measurements with a current flowing along the film so tangential to its surface. Experimentally, in the currently measured I-V curve, the current flows transversely to the Cu_2O film, this means that the desired hole mobility is transversal. This is an interesting feature of our measurements as it is seen by Pan *et al.* in [19] that the mobility is very dependent on the cubic lattice direction. Hence, the hole mobility might be different from the current direction in the crystal. It is then possible to measure the transversal mobility with I-V curves in complement to the in-plane mobility obtained with Van der Pauw measurements.

From the fit in the linear scale plot as seen in Figure 4.5, one finds the coefficient A_1 and A_2 for the linear fit and B_1 and B_2 for the quadratic which respectively corresponds to:

$$I = A_1 \cdot V^{A_2}, \qquad I = B_1 \cdot V^{B_2}.$$

Hence, from Equation 4.4 and Equation 4.5 from the SCL model, the coefficients are given as:

$$\boxed{A_1 = \frac{Aq\mu_p p_0}{t},} \qquad \boxed{B_1 = \frac{9}{8}\frac{A\varepsilon\mu_p\theta}{t^3},} \tag{4.9}$$

by saying that the non-exact coefficients $A_2 = 1$ and $B_2 = 2$ do not influence the pre-factors. First, from N_a, one finds θ and thus the mobility with B_1, and then, with the latter, p_0 in the ohmic region is also found. The results are then:

$$\boxed{p_0 = 1.27 \cdot 10^{17} \ /\mathrm{cm}^3,} \qquad \boxed{\theta = 10.06,} \qquad \boxed{\mu_p = 0.19 \ \mathrm{cm}^2/Vs,} \tag{4.10}$$

with $t = 200$ nm and $A = 2.5 \cdot 10^{-13}$ m^2. Note that the area is only an approximation as stated in the issues of the tungsten probe. The order of magnitude is right but there is an

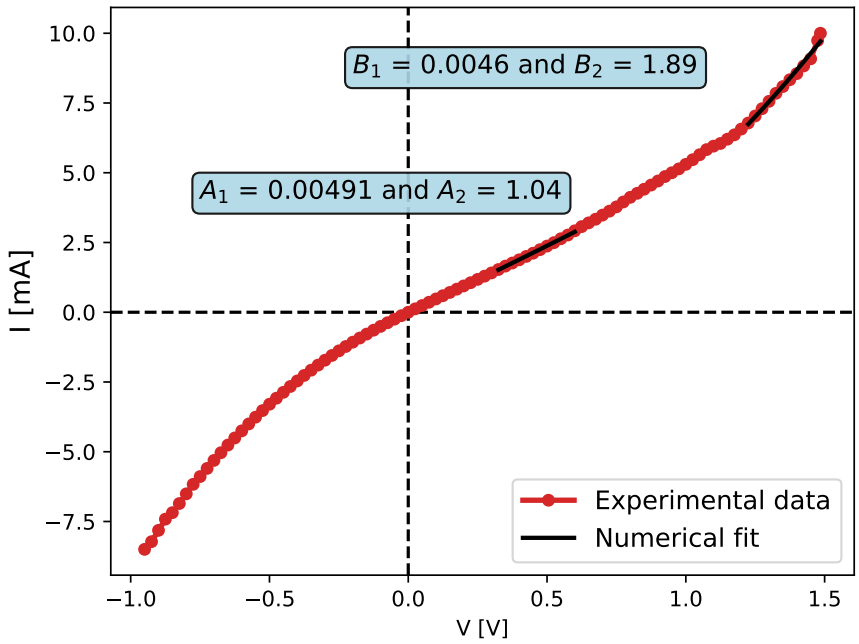

Figure 4.5: I-V curve and two linear fits of the tungsten probe, cuprous oxide contact at one point in linear scale for the TCu2O-A sample. Both linear (left fit) and quadratic (right fit) zones are represented with their fit in linear scale and their coefficient of the form: $I = A_1 \cdot V^{A_2}$.

uncertainty. If precise measurements are desired, having needles with known surface area on the tip and a precision contact leads to an exact knowledge of the area and, thus, more precise results. An expensive solution is to use a new needle for each measurement. The new needle has a known diameter which makes the area certain.

First, the hole mobility is of the same order as the Van der Pauw measured one. This means that contrary to what is shown by Pan *et al.* in [19], the mobility of the samples does not vary a lot with the direction. This can be explained by the non-uniformity of the film crystal. In their study, Pan *et al.* grown very pure epitaxial films. Here, while they have a preferential grain phase, our films are textured. This means that the grain facets have preferential orientations with good electrical properties but there is not only one. This leads to a certain anisotropy of the electrical properties.

Secondly, the concentration of the hole in the valence band at thermal equilibrium, p_0, is one order of magnitude above the density of the acceptor just previously found. This means that all the dopants are ionized. Note that the used formulas and thus results are not perfect as the slopes are not perfectly linear and quadratic. Hence, the focus is only put on the orders of magnitude and not precise values.

The resistivity, ρ, of the cuprous oxide could also be found with the slope of the linear part, $\rho = \frac{1}{A_1}\frac{A}{t} \approx 0.025\ \Omega\cdot$cm. However, it is already available via Van der Pauw measurements and the linear part is not very ohmic for the majority of the latter curves. Nothing can really be said from this value.

Full SCL analysis

At first, the measurements are displayed in Figure 4.6. As can be seen and as stated earlier, the range of applied voltage is not the same for the 4 samples as they have breakdowns at different voltages.

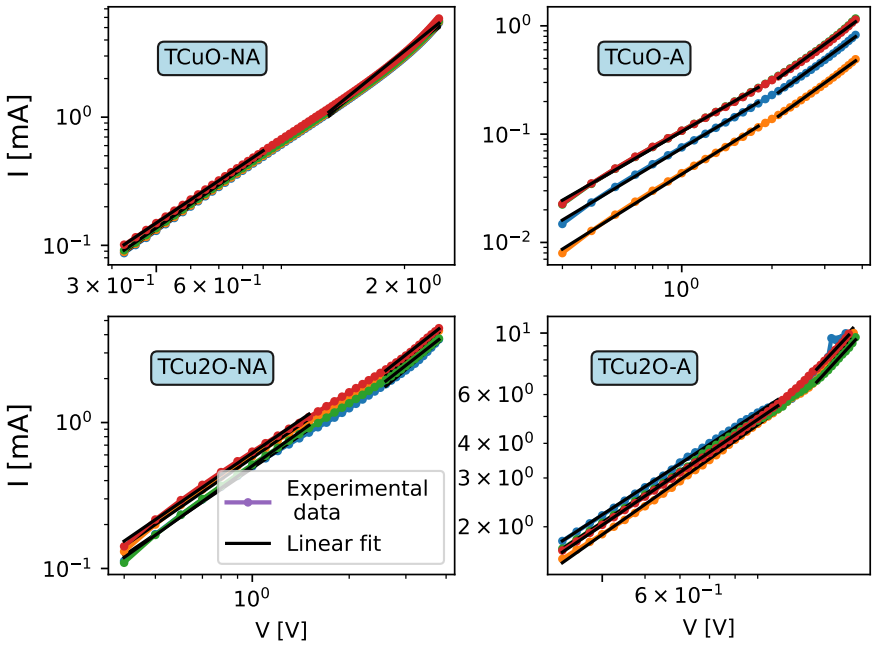

Figure 4.6: I-V curve of the tungsten probe, cuprous oxide contact at one point in log-log scale. With, for each curve, a linear fit on the left and a quadratic fit on the right (each with its zone to have the best SCL fit). The linear fitting parameters of both zones are displayed with the expression: $I = A_1 \cdot V^{A_2}$

From the several I-V curves, one can fit a linear and a quadratic curve on different portions of each curve. To have the best fit possible, the voltage range for the linear and quadratic parts is different for each sample.

The same procedure as previously made is done for the four samples. For each sample, four measurements, thus curves, are made that are analyzed separately. Once the slopes in the log-log scale for the linear and quadratic zones are found for each curve, they are averaged arithmetically to find a mean curve corresponding to the sample. Moreover, the standard deviation is also given to see the variability of these averaged slopes. Then, the same variables can be found with the fit parameters: μ_p and p_0.

All these results are shown in Table 4.1.

4.2.2 SCL model interpretation

First, the quadratic fit is quite good as the power is close to 2 for all samples. However, the linear part is not perfect, thus ohmic, as the power is not very close to the unity. It has a difference of 50 % in some cases.

	TCuO-NA	TCuO-A	TCu2O-NA	TCu2O-A
Voltage range	$[0.2; 0.7]$ and $[1.2; 2.5]$	$[0.2; 1.8]$ and $[2; 3.9]$	$[0.2; 1.5]$ and $[2.5; 3.9]$	$[0.2; 1]$ and $[1.2; 1.5]$
Linear	1.9 ± 0.02	1.65 ± 0.056	1.52 ± 0.029	1.07 ± 0.031
Quadratic	2.23 ± 0.002	2.01 ± 0.017	1.77 ± 0.048	1.77 ± 0.071
$N_a(V^\star)$ [/cm^3]	$N_a(0.8) = 1.68 \cdot 10^{16}$	$N_a(1.2) = 2.52 \cdot 10^{16}$	$N_a(1.4) = 2.94 \cdot 10^{16}$	$N_a(1.1) = 2.31 \cdot 10^{16}$
μ_p [cm^2/Vs]	0.018 ± 0.0005	0.0024 ± 0.0006	0.015 ± 0.002	0.18 ± 0.01
p_0 [/cm^3]	$(2.16 \pm 0.013) \cdot 10^{17}$	$(1.62 \pm 0.0081) \cdot 10^{17}$	$(1.53 \pm 0.0092) \cdot 10^{17}$	$(1.47 \pm 0.060) \cdot 10^{17}$

Table 4.1: Extracted parameters from the SCL curve fitting with the given voltage range for the four samples. From the slopes, the hole mobility and hole concentration at thermal equilibrium are obtained.

A possible explanation of why the I-V curves do not have a linear part, hence, an ohmic behavior could be due to the resistivity. As the thin film resistivity is much smaller for our samples compared to [20], the ohmic behavior is much smaller and negligible compared to the quadratic power. That is why the curve fitting cannot capture a linear part.

First, the acceptor density N_a is of the order of 10^{16} /cm^3 for all samples. This is a pretty good order of magnitude as it is the same as [20] and others. This is the order aimed for this work. However, the precise value does not matter that much as it depends on the potential choice $V^\star$, in which precision is subjective because the change between the linear and quadratic parts is not straightforward. Then, as already mentioned, the hole mobility is a bit smaller or of the same order as the Van der Pauw measurement. This means that there is only a small change between the in-plane mobility and transversal. This can be explained by the fact that the film is polycrystalline. At the same time, it is also a bit textured with a small majority of the phase (111). This could mean that if the mobility is larger in the in-plane direction, the (111) phase is oriented in that direction, as the (111) phase has a larger mobility as reported in [19]. However, this effect is not strong, and concluding a real difference between the mobilities is not advised.
Last, at thermal equilibrium, the hole concentration in the valence band extracted from the SCL model is one order of magnitude smaller than the one measured with the Van der Pauw measurement. This is not an issue because, as said earlier, the ohmic region is not perfectly ohmic and the concentration of holes is extracted from this part. This means that errors are possible and the difference between this value and the one measured via Van der Pauw is not enough to discard the SCL model. From these results, one can say that there is no clear change in behavior between the annealed samples and the others. The films being textured, enhancing the crystallinity does not change the overall anisotropic character of the films.

Here, the results are not as useful as the one measured by Pan *et al.* in [19] or by Rakhshani *et al.* in [20]. In their articles, the slopes were perfectly at 1 and 2. They could then extract very precise physical quantities. In the current work, only orders of magnitude are obtained due to variability in the measurements. These lasts can be due to the variable contact area of the needle and due to the tungsten contact. In their articles, they use gold [19] or aluminum [20] contact instead. It is known that the contact gold-cuprous oxide is a good ohmic contact.

Here, the aim was to see whether the tungsten was a good and quick alternative, not having precise measurements. To conclude, I would say that for quick and easy contact to find an order of magnitude of the different physical quantities in Table 4.1, tungsten is a good option that could be more developed.

Additionally, it would be interesting to try a gold deposition instead of the use of the tungsten probe. This gold contact could maybe exhibit a better contact with the cuprous oxide and give a better SCL curve. If the curves are the same as the ones obtained with the tungsten probes, this means that the imperfect behavior of the I-V curves with respect to the SCL model comes from the film and not the contact. This would mean that the tungsten contact gives the same results as the gold ones without a real deposition.

Chapter 5

Solar cell simulations

This chapter aims to investigate solar cells made of copper oxide and gallium oxide. Copper oxide solar cells are very promising for transparent solar cells as cuprous oxide is the most convenient transparent p-type semiconductor. Moreover, the most studied thin film solar cell made of cuprous oxide is the Al-doped zinc oxide | cuprous oxide cell. Toghyani Rizi *et al.* in [61] have shown that the main issue with this cell is a conduction band offset (ΔE_c), as it decreases the shunt resistance, hence, the efficiency. This problem can be tackled using a buffer layer, such as gallium oxide. Having an n-type material with a large band gap as the one of gallium oxide can yield a greater efficiency. Moreover, in its article [10], Minami *et al.* do not take an N-doped Cu_2O, as is the case experimentally in this work. The idea of this work is then to take the doping from the laboratory and simulate it to see the impact.

The first part of this work introduces the software Scaps [62] that is used. This allows us to understand the limitations and the results of the simulations. Then, to determine the best solar cell parameters, the influence of the doping and the thickness of each layer is varied using the software. At first, the ideal cell without defects is studied to find optimal parameters. Then, defects in the bulk are added with the same parameters optimization to understand their effects on the I-V parameters. Lastly, adding an n-type as a buffer layer is investigated hopefully to increase the efficiency.

5.1 Numerical tools

To simulate the I-V curve of any cells, the recombination rates, currents, and so on, the software Scaps is used. It is a one-dimensional semiconductor device solver. It works as follows:

- It takes a complete problem in input with several semiconductors side-by-side, with their physical parameters such as the carrier's concentration, affinity, band gap, etc. One can also specify defects, and interface states for each semiconductor. Furthermore, simulation under light can also be carried out with a given spectrum such as AM 1.5. Additionally, it is also required to give a temperature:300 K.
- It automatically discretizes the spatial domain along x. Furthermore, the Scaps' dis-

cretizing algorithm adds more elements in the 1-D mesh near the interfaces with an element size always under the Debye length. The Debye length is the characteristic distance of the net electrostatic effect of a charge carrier. The spatial discretization for an ideal silicon pn junction is displayed in Figure 5.1.

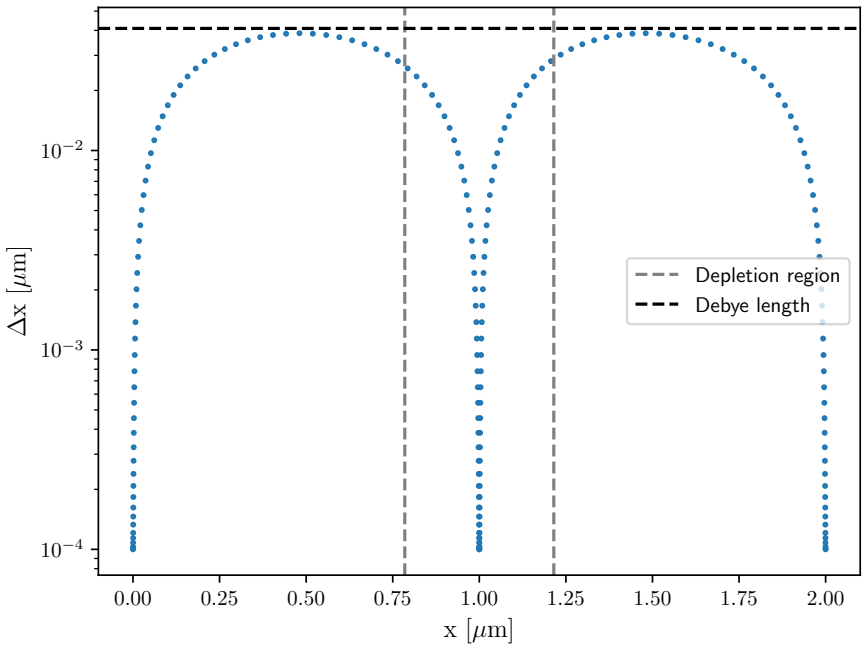

Figure 5.1: Spatial discretization used by Scaps for an ideal pn junction with the given parameter in Table 5.1.

- Once the simulation is ready, the only required step is to solve the semiconductor equations for $(\Phi, E_{fn}$ and $E_{fp})$ with the system of equations 5.1 and 5.2:

$$\begin{cases} \dfrac{\partial}{\partial x}\left(\varepsilon\dfrac{\partial \Phi}{\partial x}\right) = -q\left(p - n + N_d - N_a + \dfrac{\rho}{q}\right), \\ \dfrac{1}{q}\dfrac{\partial J_n}{\partial x} - U_n + G = \dfrac{\partial n}{\partial t}, \\ -\dfrac{1}{q}\dfrac{\partial J_p}{\partial x} - U_p + G = \dfrac{\partial p}{\partial t}, \end{cases} \tag{5.1}$$

$$\begin{cases} J_n = \mu_n n \dfrac{\partial E_{fn}}{\partial x}, \\ J_p = \mu_p p \dfrac{\partial E_{fp}}{\partial x}. \end{cases} \tag{5.2}$$

From those results, one can find all the measurable variables such as the potential, the recombination rate, the I-V curve, and so on.

5.1.1 Numerical and analytical comparison for the homojunction

The considered junction is an ideal Si pn junction with the parameters in Table 5.1.

	p-type	n-type
x [μm]	1	1
ε	11.7	11.7
E_g [eV]	1.12	1.12
$q\chi$ [eV]	4.05	4.05
N_c [cm^{-3}]	$3.2 \cdot 10^{19}$	$3.2 \cdot 10^{19}$
N_v [cm^{-3}]	$1.8 \cdot 10^{19}$	$1.8 \cdot 10^{19}$
μ_n [cm$^2/(V \cdot s)$]	50	50
μ_p [cm$^2/(V \cdot s)$]	50	50
N_d [cm^{-3}]	0	10^{16}
N_a [cm^{-3}]	10^{16}	0

Table 5.1: Si data for pn junction without defects and interface states.

To compare the numerical and analytical results of the ideal pn junction, the analytical results for an ideal abrupt junction are taken in *Power Electronics Semiconductor Devices* by Perret [63]. Without going into the mathematical details, the semiconductor equations are solved for an electrical internal potential. One can compare easily the electric field and the charge carrier concentrations. Both results are shown in Figure 5.2.

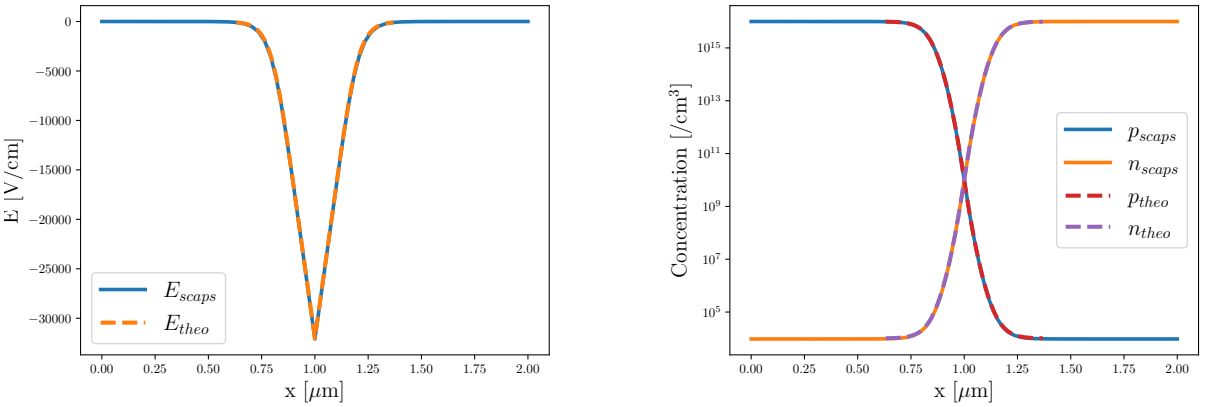

(a) Electric field comparison at equilibrium.

(b) Charge carriers' concentrations at equilibrium.

Figure 5.2: Analytical and numerical comparison for the ideal pn junction.

As can be seen in Figure 5.2, the curves from Scaps are very close to the analytical ones, hence, it can be concluded that for the simple homojunction, the numerical results from Scaps are correct.

5.1.2 Numerical and analytical comparison for the heterojunction

One can make the same comparison with the heterojunction. For the moment, the cell is given as it is but is developed deeply in the second part of this chapter.

One issue is that there are no analytical results for the heterojunction. Because the homojunction provided good numerical results, a comparison with only the band's discontinuity and the depletion width with their known analytical expressions at equilibrium is used to validate the results.

The studied heterojunction has the parameters given in Table 5.2.

	Ga_2O_3 - n-type	Cu_2O - p-type
x [μm]	0.5	5
ε_r	10	7.6
E_g [eV]	4.8	2.1
$q\chi$ [eV]	4	3.2
N_c [cm^{-3}]	$3.72 \cdot 10^{18}$	$2.43 \cdot 10^{19}$
N_v [cm^{-3}]	$3.72 \cdot 10^{18}$	$1.34 \cdot 10^{19}$
μ_n [$cm^2/(V \cdot s)$]	118	200
μ_p [$cm^2/(V \cdot s)$]	50	100
N_d [cm^{-3}]	$1.6 \cdot 10^{18}$	10^9
N_a [cm^{-3}]	10^9	10^{14}
α_r [cm^3/s]	10^{-12}	10^{-12}
α_A^n, α_A^p [cm^6/s]	10^{-30}	10^{-30}

Table 5.2: Ga2O3-Cu2O data for pn junction without defects and without interface states.

The energy band diagram at equilibrium is plotted in Figure 5.3. Note that while the quasi-Fermi levels do not seem to coincide together if the junction gets much longer (100 μm), the quasi-Fermi levels do meet together at the Fermi level. From the expression given in section 2.5, one finds:

$$\boxed{x_n = 10^{-4}\ \mu\text{m},} \qquad \boxed{x_p = 2.59\ \mu\text{m}.}$$

Moreover, the shifts of bands at the junction are the same as calculated in section 2.5 and are indeed:

$$\boxed{\Delta E_c = 0.8\ \text{eV},} \qquad \boxed{\Delta E_v = 3.5\ \text{eV}.}$$

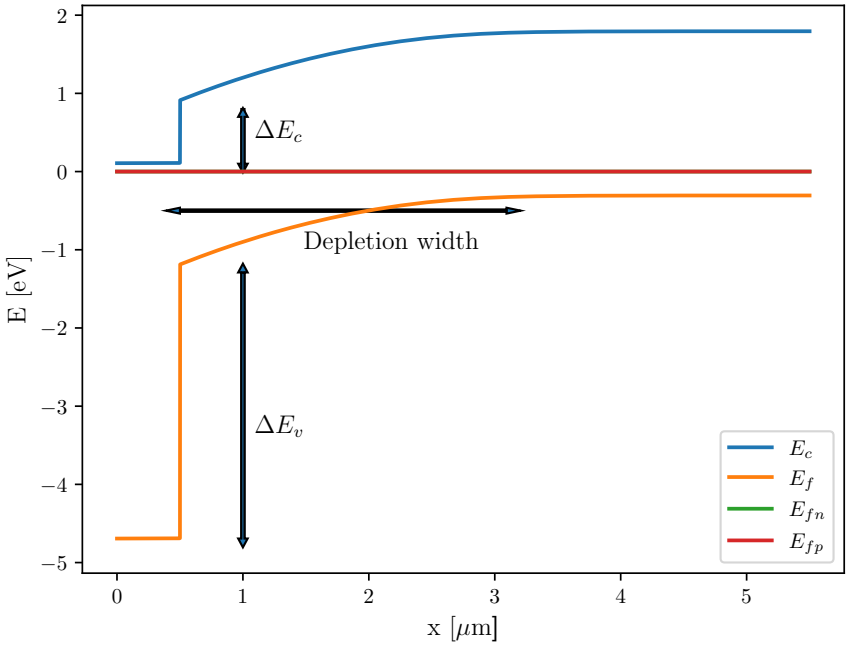

Figure 5.3: Energy band diagram of the heterojunction Cu_2O-Ga_2O_3 at equilibrium.

5.1.3 Homo and hetero junction comparison

One question the reader could ask is: would not it be more interesting and efficient to work on the homojunction of Cu_2O than having a hetero junction with Ga_2O_3? To answer this question, using Scaps, the comparison between both under light is pretty straightforward. To do so, the previous heterojunction from Table 5.2 is used and the homojunction is made of Cu_2O. To compare both homo and heterojunction, the same doping density $N_d = 1.6 \cdot 10^{18}$ cm^{-3} is used.

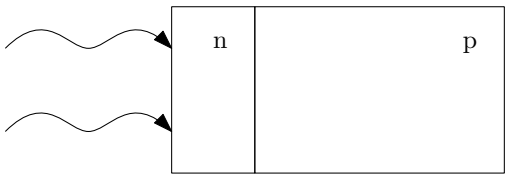

Figure 5.4: Schematic of the homo and hetero junction with incident light.

The numerical setup is displayed in Figure 5.4.

Energy band diagram comparison

The first thing one can do to visualize the differences is simply see the changes in the depletion region in the energy band diagram at equilibrium between the hetero and homo junction. As can be seen in Figure 5.5, the differences in band gap induce large shifts in the depletion region for the heterojunction.

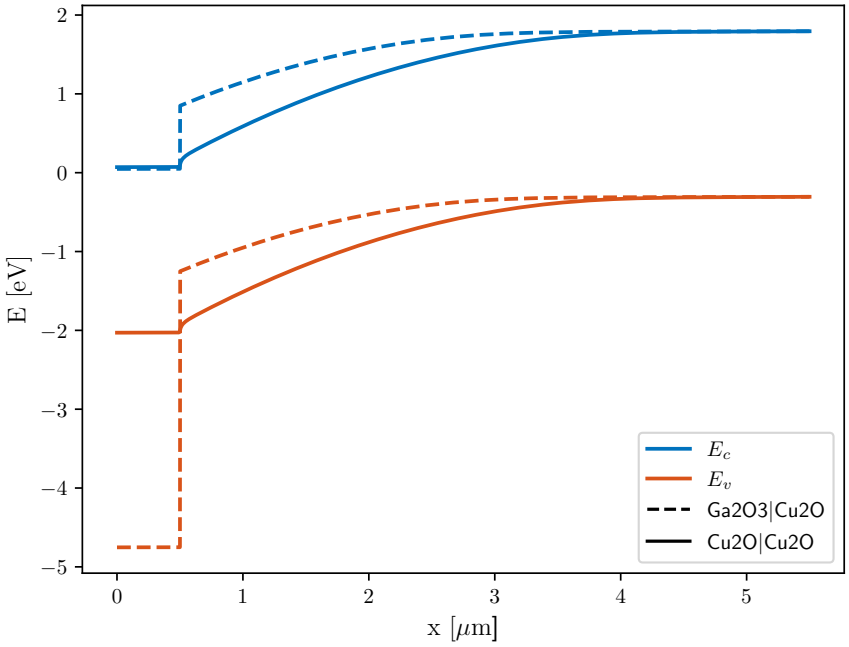

Figure 5.5: Energy band diagram at equilibrium without illumination for the hetero and homojunction.

Electron hole pair generation comparison

The second comparison is between the recombination and generation of charge carriers along the junction. Figure 5.6 clearly shows that due to the large gap of the Ga_2O_3, all the light is transmitted to the Cu_2O and there are nearly no generations in the n-type. Whereas for the homojunction, the generation decays exponentially from the illuminated surface as expected. Here, the comparison is simple as there are no defects nor traps in the bulks. As the bulks are considered perfect without defects, hence trap states, only Auger and direct radiative recombinations are allowed. To simulate these, it is required to give coefficients for those mechanisms available in Table 5.2.

To understand the shape of the recombinations, one can see that there are constants in the bulk out of the depletion region and vary quickly in the depletion region. In the latter case, it follows the given curves as shown in Figure 5.7, which are the products appearing in the recombination expressions. Namely: radiative recombination $R_{rad} = \alpha_r(np - n_i^2)$ and the Auger recombination $R_{aug} = (\alpha_A^n n + \alpha_A^p p)(np - n_i^2)$. The aim of this recombination plot is also to see whether Auger's processes are as important as direct recombinations. One sees that the radiative effects are several orders of magnitude above the Auger processes. This means that Auger processes are not very important. Auger recombinations can be neglected in our interpretations.

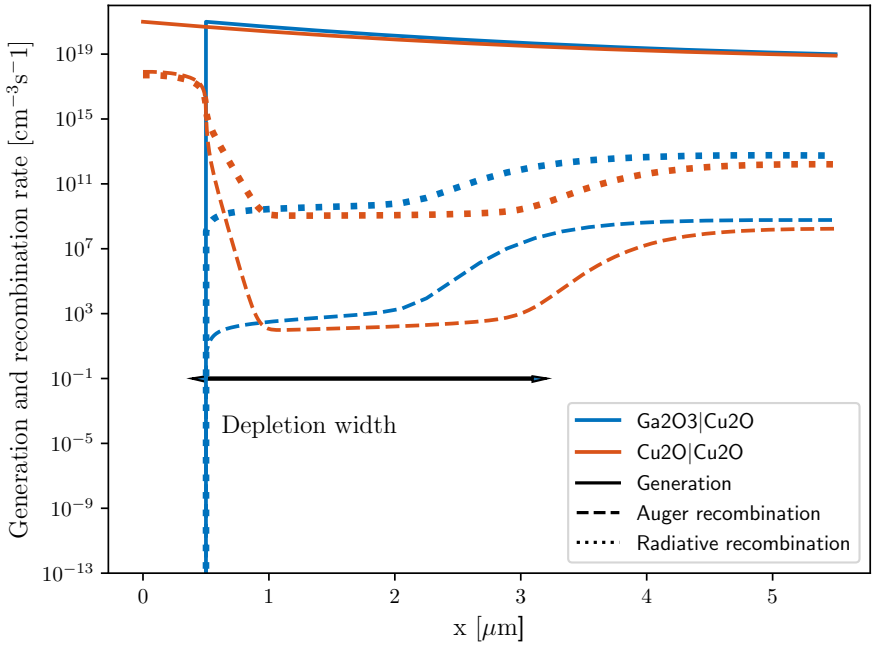

Figure 5.6: Generation and recombination of EHP of the hetero and homo junction at 0 V.

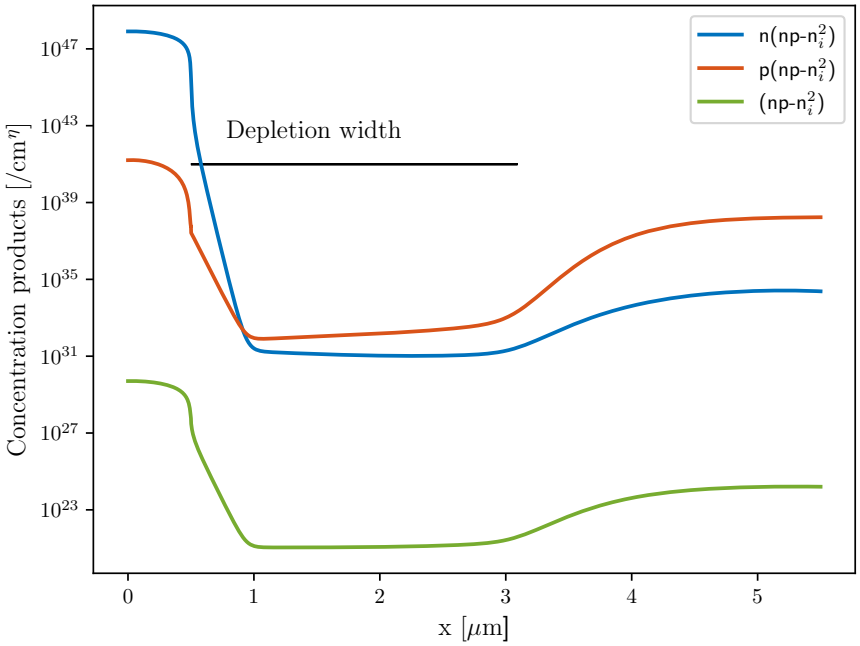

Figure 5.7: Concentration products for each type of recombination processes

Current density comparison

One useful piece of information for a solar cell application is the total current density. The higher the current, the higher the power. Here, the junctions are at equilibrium with illumination on the left.

$$\boxed{J_{\text{tot}}(\text{Cu}_2\text{O-Cu}_2\text{O}) = -11.61 \text{ mA/cm}^2,} \qquad \boxed{J_{\text{tot}}(\text{Ga}_2\text{O}_3\text{-Cu}_2\text{O}) = -12.03 \text{ mA/cm}^2.}$$

Here, even though the gallium oxide is nearly completely transparent, it is important because all the light goes to the copper oxide without being absorbed by the gallium oxide. Thus, a large current is generated by the latter.

To conclude, it is more efficient to have a heterojunction with the gallium oxide as it decreases the recombination at the interface and generally increases the efficiency. Moreover, in the current situation, it is not possible to have an n-type Cu_2O in reality. Even though the homojunction existed, it would not be interesting to use it instead of the heterojunction.

5.1.4 Fill factor analysis

During this work, no shunt or series resistances are considered. However, there is still a given fill factor by Scaps. One can understand its behavior by looking at Figure 5.8 with their respecting fill factor in Table 5.3.

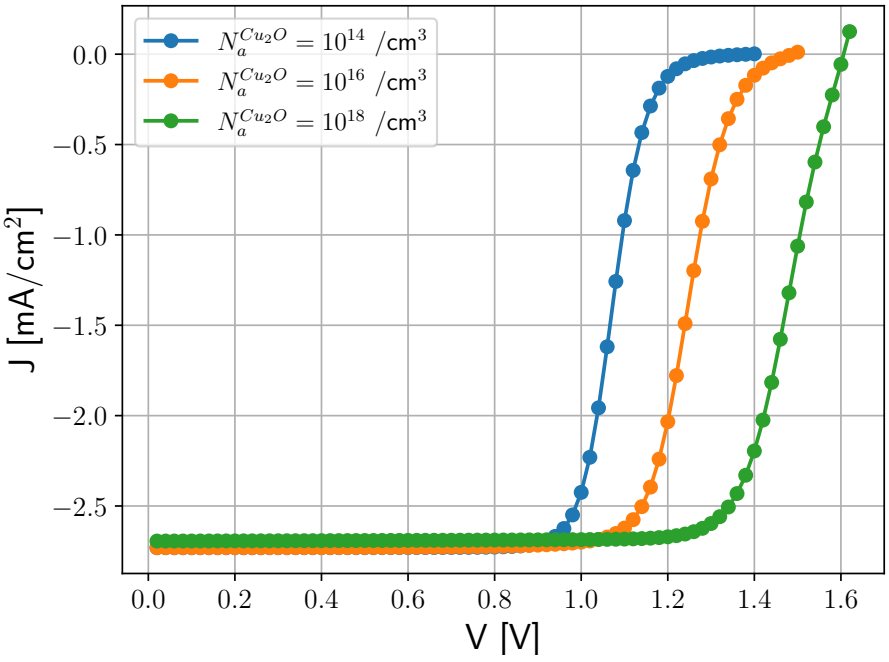

Figure 5.8: I-V curve of the heterojunction Ga_2O_3-Cu_2O solar cell under AM 1.5 illumination with default parameters given in Table 5.4.

From these results, one can see that with doping, as expected, the short-circuit current

$N_a^{Cu_2O}$ [/cm^3]	FF [%]	V_{oc} [V]	J_{sc} [mA/cm^2]
10^{14}	66.6	1.38	-2.73
10^{16}	71	1.45	-2.73
10^{18}	78	1.6	-2.69

Table 5.3: I-V parameters for the I-V curves shown in Figure 5.8.

does not change a lot while the open-circuit voltage does. The point of interest here is the fill factor. Because there is no external resistance, it is only influenced by the geometrical aspect of the I-V shape. This means that the larger the short circuit current or the open circuit voltage, the larger the fill factor. And the more square-like the shape is, the larger the fill factor. Here, one sees on Figure 5.8 that the shape is very similar between the three and it seems that they are shifted, which shows that the variation of parameters has an impact on J_{sc} or V_{oc} but not directly on the fill factor.

5.2 Modelling of the cell

In this work, the computed cell is made of an absorber layer of Cu_2O and a transparent layer of Ga_2O_3. This cell has a maximum theoretical efficiency of 20 % [10]. However, the experimental record is around 10 % using additional buffer layers. Hence, having a good recipe for N-doped Cu_2O can increase efficiency. This is investigated in this chapter. The choice of gallium oxide as justified in [10] comes from the decrease of the shunt resistance with this layer. Having a large ΔE_c, thus, increases the fill factor and the efficiency. This is not talked about in this work but it has other impacts with its doping that are investigated here.

5.2.1 Hypothesis

- During the simulations, the doping is uniform in the material, as well as the defects in the bulk. The possible added defects have a Gaussian distribution energy in the band gap as discussed later. No interface defects are simulated in this work.
- For the first section, the cell is considered pristine. However, in the latter, real defects are taken into account.
- During this work, no resistance in or out of the junction is taken into account, namely, the series and shunt resistance. This has an effect that is not negligible for a real cell. It has been demonstrated by Sahin *et al.* in [64] that both shunt and series resistance have different impacts on solar efficiency.
- The contact on the left and right of the junction are ohmic with imposed flat bands. This guarantees more readable graphs. Experimentally, in the case of cuprous oxide, the electrode is often gold as it has indeed a good ohmic contact as shown in [12] and [65].
- While it has been shown in the chapter chapter 4 that the main current model for the cuprous oxide was the SCL model, Scaps only uses the drift/diffusion model. Thus, the drift-diffusion model is used.
- The absorption coefficient for cuprous oxide is measured and shown in Figure 5.9. It is measured via optical measurement (UV-Vis spectroscopy). However, the gallium oxide, also shown in Figure 5.9, has a band gap larger than the glass on which it is deposited. Hence, with optical measurement of the gallium oxide on glass, one would only measure the glass. Special substrates, such as quartz, are needed. Unfortunately, this option is not available in the laboratory. Hence, the only solution to know the absorption coefficient of gallium oxide is to model it in Scaps using $\alpha(\nu) \propto \sqrt{h\nu - E_g}$ as in Figure 5.9. Because the band gap is very large, and the solar spectrum AM 1.5 is mainly in the range [400,2000] nm, the gallium oxide is nearly 100 % transparent and the model is not that important.

The starting point of this numerical study is the cell previously studied with gallium oxide and cuprous oxide. The parameters are reminded in Table 5.4. These values come from

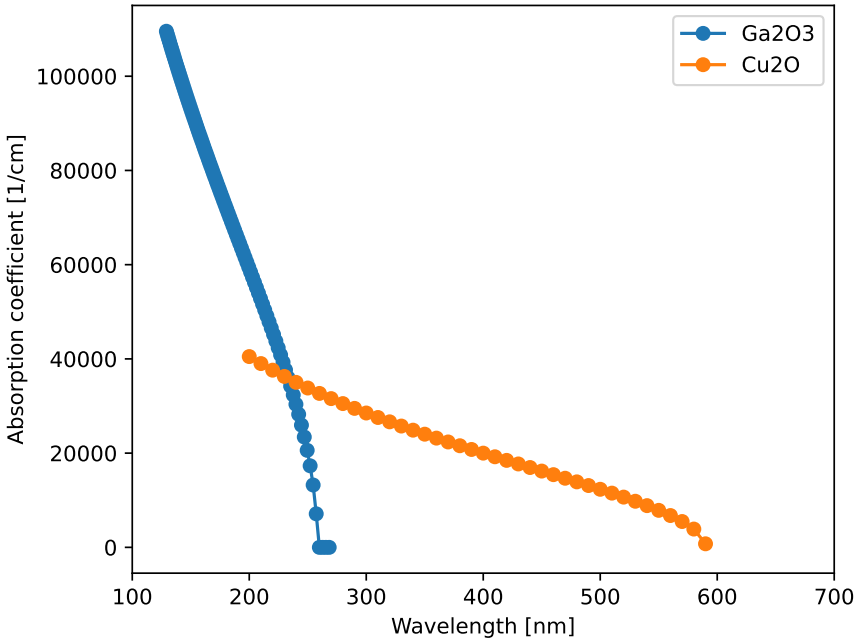

Figure 5.9: Absorption coefficient used in Scaps for the solar cell modeling.

measurements in the laboratory, or other articles as [66], [61] and [12]. Some quantities such as electron mobility in cuprous oxide are not experimentally measured. However, this is not important as they have been varied numerically and do not have a relative impact superior to 15 % on solar efficiency when varying from 1 to 200 cm^2/Vs $((\eta(200) - \eta(1))/\eta(200))$. Values from numerical simulation based on experimental work as taken as in [61]

	Ga_2O_3 - n-type	Cu_2O - p-type
x [μm]	0.01	0.2
ε_r	10	7.6
E_g [eV]	4.8	2.1
$q\chi$ [eV]	4	3.2
N_c [cm^{-3}]	$3.72 \cdot 10^{18}$	$2.43 \cdot 10^{19}$
N_v [cm^{-3}]	$3.72 \cdot 10^{18}$	$1.34 \cdot 10^{19}$
μ_n [$cm^2/(V \cdot s)$]	118	200
μ_p [$cm^2/(V \cdot s)$]	50	0.7
N_d [cm^{-3}]	$1.6 \cdot 10^{18}$	10^9
N_a [cm^{-3}]	10^9	10^{14}
α_r [cm^3/s]	10^{-12}	10^{-12}
α_A^n, α_A^p [cm^6/s]	10^{-30}	10^{-30}

Table 5.4: Ga_2O_3-Cu_2O data for pn junction without defects and without interface states.

5.2.2 Thickness variation

To start with, one can study the thickness variation of both layers. However, the studied thicknesses need to be fabricated via our RF sputtering which can only make films of around 300 nm. Other methods such as electrodeposition are low-cost and privileged, but the cells lose their transparent ability. Most importantly, because this work aims to develop transparent or semi-transparent films, one is only limited to tenths of microns. Hence, the thickness study is limited. The I-V parameters resulting from this study are shown in Figure 5.10.

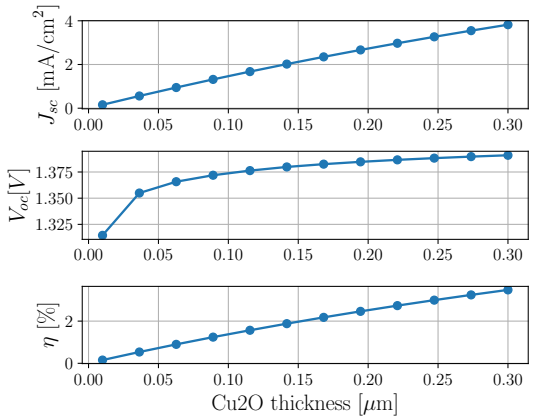

(a) Variation of the I-V parameters with the Cu_2O thickness.

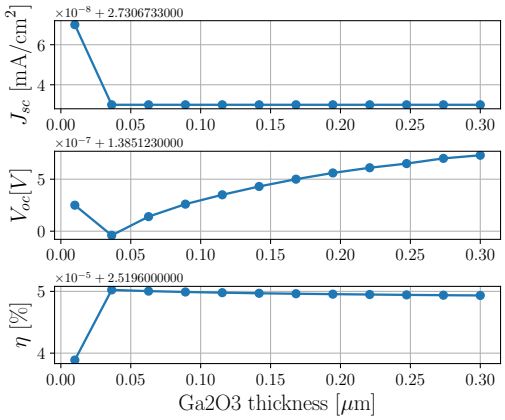

(b) Variation of the I-V parameters with the Ga_2O_3 thickness.

Figure 5.10: Variation of the I-V parameters with both thickness of the ideal Ga_2O_3-Cu_2O solar cell under AM 1.5 illumination with default parameters given in Table 5.4.

As can be interpreted, the thickness of the gallium oxide does not change at all of the I-V parameters. The variations are of the order of the floating points error of Scaps. It was expected because it is highly transparent. It is important to note that the varied thickness still guarantees enough room for the depletion width.
Additionally, the thicker the cuprous oxide, the better the short circuit current. The open circuit also increases but with a smaller slope. Increasing the thickness of the cuprous oxide results in more absorption, more generated charge carriers, and, hence, more efficient cells. It is shown in [61] and others that a layer of several microns of copper oxide leads to a more efficient cell. However, it has been shown by Sliti *et al.* in [12] that there is a maximum of around 10 μm where all the incoming light is absorbed and further increase of the thickness would lead to more recombinations without more optical generation. In any case, our choice is limited by the deposition method and the transparency criterion. Hence, 300 nm is chosen.

5.2.3 Doping variation

The doping concentration of the majority carriers is also investigated. The results are displayed in Figure 5.11. One can see that when the doping increases, the efficiency increases but to a certain threshold. First, the gain of efficiency with doping can be explained by the shift of the conduction and valence bands upwards in the cuprous oxide. As said by Sliti *et*

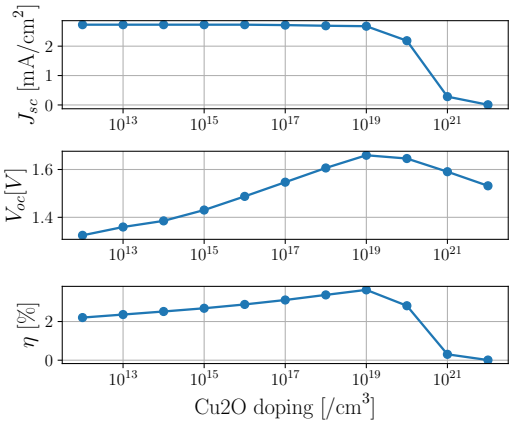

(a) Variation of the I-V parameters with the Cu_2O doping (N_a).

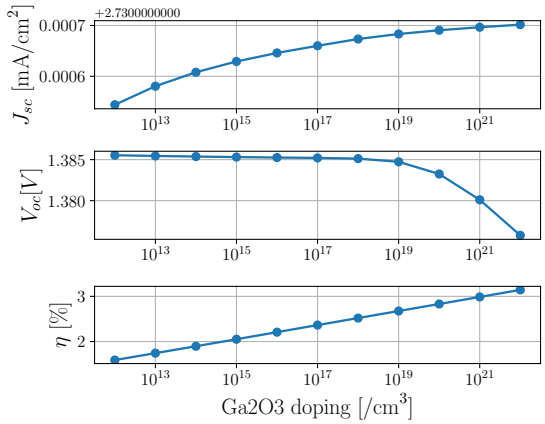

(b) Variation of the I-V parameters with the Ga_2O_3 doping (N_d).

Figure 5.11: Variation of the I-V parameters with both doping concentration of the ideal Ga_2O_3-Cu_2O solar cell under AM 1.5 illumination with default parameters given in Table 5.4.

al. in [12], this decreases the number of holes going towards the interface and recombining. However, after a certain threshold, there are many more recombinations through the doping levels as the characteristic time between recombinations τ_n is proportional to $\frac{1}{N_a}$. This means that the higher the doping, the smaller the time between recombination, thus, the number of recombination increases. This is seen by comparing the recombination rate for two different doping of cuprous oxide in Figure 5.12. It is then a balance between high carrier density and recombination. In the lab, because the copper oxide is doped via a constant nitrogen flux, the doping is often of the order of 10^{18} /cm^3. For the gallium oxide, it is shown in [66], [61] and [67] that with several doping methods, one can achieve doping of the order of 10^{18} /cm^3. Having high doping n-type decreases the number of minority carrier generation and thus, the recombination loss at the interface.

5.2.4 Optimized solar cell

From the previous results, one can extract the optimal parameters for the ideal solar cell. Here, the hypothesis is that the parameters are uncoupled from each other. This is explained later. Hence, one finds:

$$\boxed{x^{Ga_2O_3} = 20 \text{ nm},} \qquad \boxed{x^{Cu_2O} = 300 \text{ nm}.} \tag{5.3}$$

$$\boxed{N_d^{Ga_2O_3} = 10^{18} \text{ /cm}^3,} \qquad \boxed{N_a^{Cu_2O} = 10^{18} \text{ /cm}^3.} \tag{5.4}$$

The chosen value corresponds to the maximum or the experimentally possible optimum of the tested values. The simulation for the optimal cell gives the following and the curve in Figure 5.13:

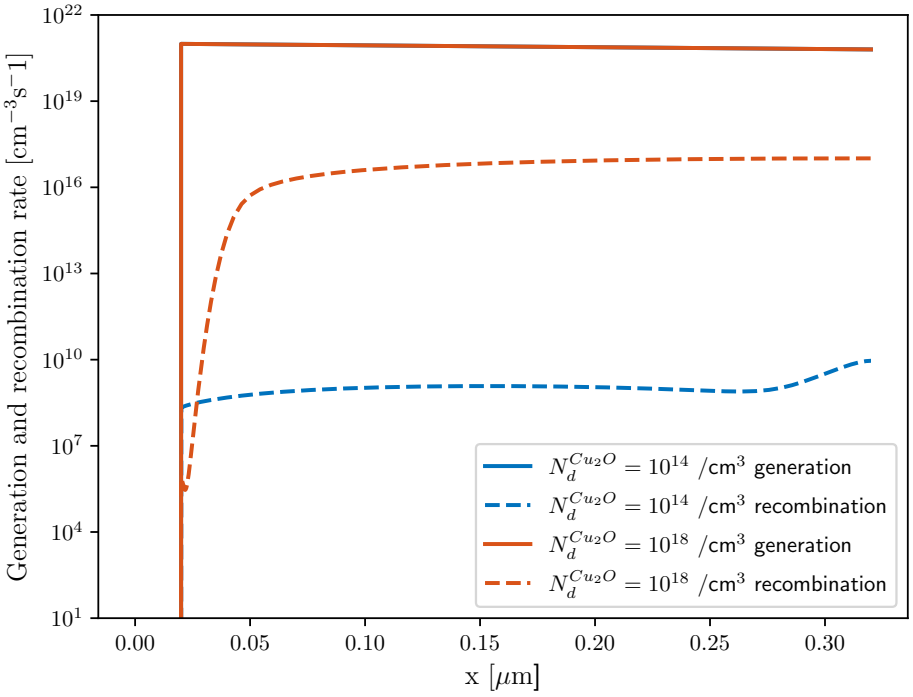

Figure 5.12: Generation and recombination rate for the $Ga_2O_3|Cu_2O$ junction for two different Cu_2O doping at equilibrium under AM 1.5 illumination.

V_{oc} [V]	J_{sc} [mA/cm^2]	FF [%]	η [%]
1.61	3.73	77.43	4.7

Table 5.5: I-V parameters for the optimal pristine solar cell without any bias.

5.2.5 Coupling of the varied parameters

To find the optimal parameters, it has been assumed that the doping and the thickness were uncoupled to allow for an easy and fast study. Each parameter was studied one at a time. However, to be sure that this assumption was not too strong, a quick small study on the cuprous oxide was made with the coupling with 6x6 parameters. The results are shown in Figure 5.14.

As can be seen, the same behavior is seen in the map in the two separated optimizations in Figure 5.11(a) and Figure 5.10(a). The doping has a maximum of around 10^{19}, whatever the thickness. The larger the thickness, the better. Hence, the following optimizations are made separately.

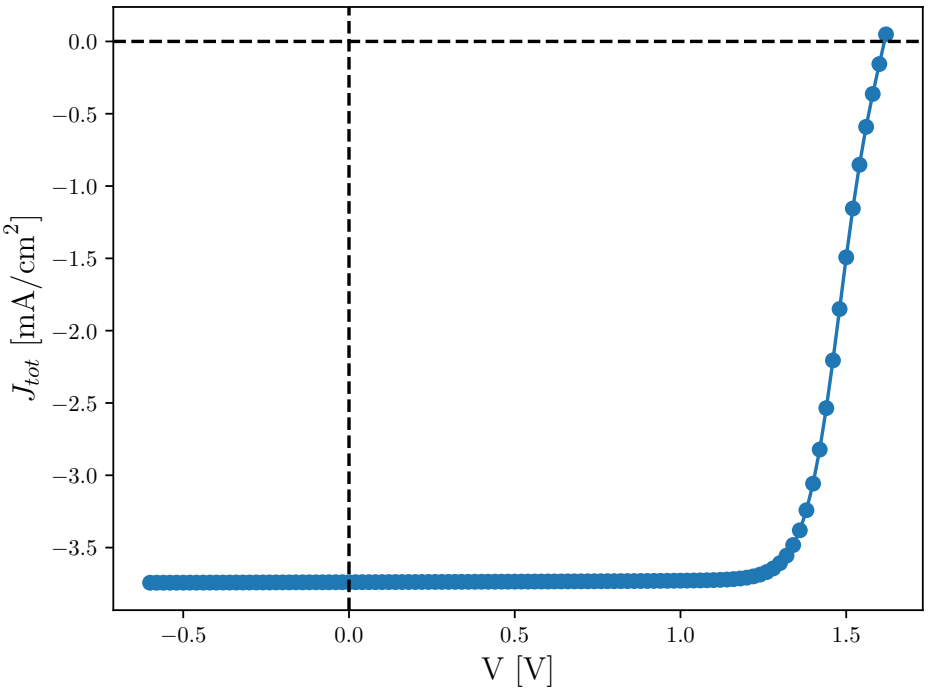

Figure 5.13: I-V curve of the optimal pristine Ga_2O_3—Cu_2O solar cell under AM 1.5 illumination with default parameters given in Table 5.4.

5.3 Solar cell with defects

Defects in the cuprous oxide are very important. The transport of carriers in the film is made possible thanks to copper vacancies which act as acceptors as they lead to extra holes. These holes at different states have the same effective mass as the holes in the valence band of Cu_2O. All of this makes the Cu_2O *p*-type [68]. Hence, to make a simulation that is faithful to reality, one needs to take the effects of defects that have opposite effects compared to the vacancies. This means defects that act, not as acceptors but as donors.

5.3.1 Including defects in the simulation

To study the effect of the defects in the bulk of the semiconductors, one starts from the optimal cell and adds defects. To simulate these in the bulk of the semiconductors, the data of defects used are available in Table 5.6. These defects come from Adaika *et al.* in [69] for the gallium oxide and from Sawicka *et al.* in [70] for the cuprous oxide. The defects are deep-level defects with a Gaussian distribution of energy. They are then near the middle of the band gap. They have been found numerically to match experimental results. The complete procedure for both gallium oxide and cuprous oxide is developed by Toghyani *et al.* in [61].

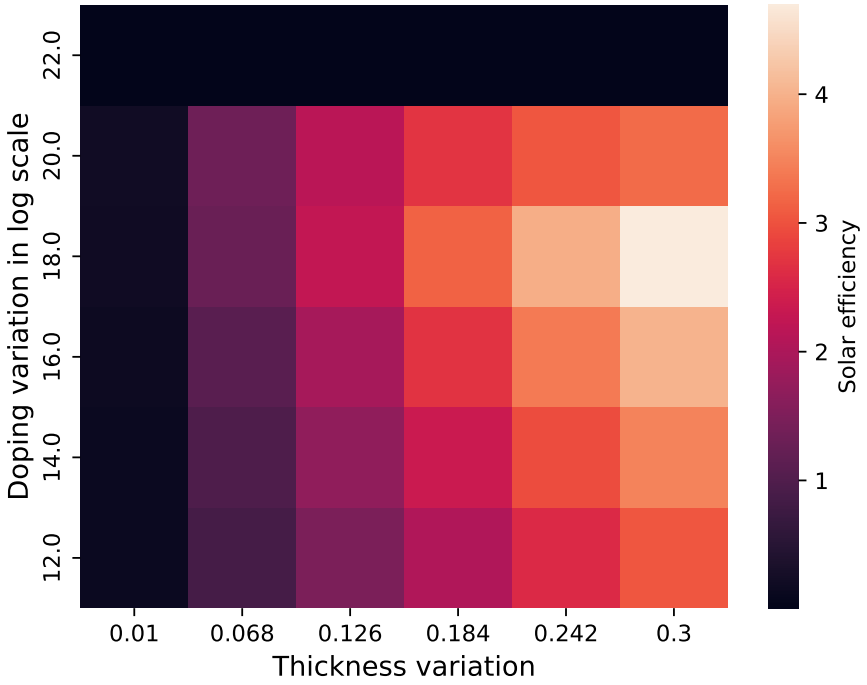

Figure 5.14: Study of the coupling effect on the efficiency for varying thickness and doping of Cu_2O in the Ga_2O_3-Cu_2O solar cell under AM 1.5 illumination with optimal parameters for gallium oxide.

	Defect type	Capture cross section [cm^2] (σ_e/σ_a)	Defect density [/cm^3]	Energy level [eV]	Standard deviation [eV]
Cu_2O	D-like, Gaussian	$5 \cdot 10^{-13}/10^{-15}$	10^{13}	Midgap	0.1
Ga_2O_3	D-like, Gaussian	$10^{-12}/10^{-15}$	$5 \cdot 10^{17}$	Midgap	0.05

Table 5.6: Numerical defect data for the Cu_2O—Ga_2O_3 solar cell [66], [61] and [12].

5.3.2 Thickness variation

As previously, the thickness of each layer is varied independently from the other. The results are available in Figure 5.15. As can be seen, the thickness of the gallium oxide still does not matter. For copper oxide, the behavior is also the same as previously, the thicker, the better. One still takes the maximum thickness possible in the laboratory.

5.3.3 Doping variation

The study of the doping in Figure 5.16 shows immediately that the addition of defects makes the efficiency decrease. However, the increase in doping has the same effect as without defects: a decrease of the recombination loss in the depletion region but an increase of the recombination in the semiconductors.

The simulation for the optimal cell with defects gives the following:

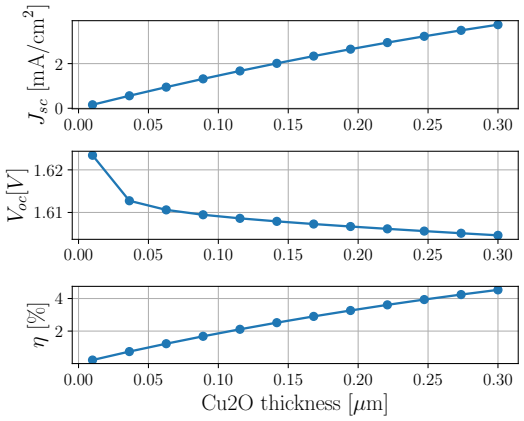

(a) Variation of the I-V parameters with the Cu_2O thickness.

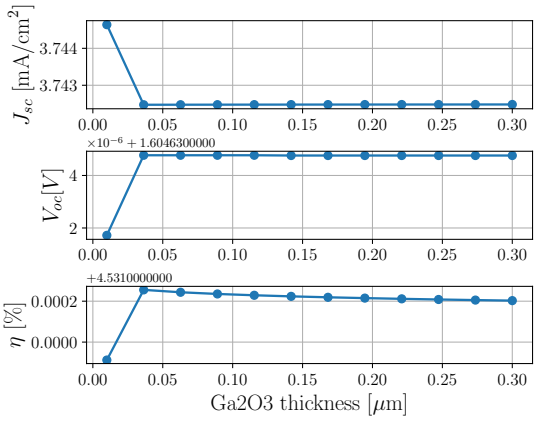

(b) Variation of the I-V parameters with the Ga_2O_3 thickness.

Figure 5.15: Variation of the I-V parameters with both thickness concentration of the Ga_2O_3-Cu_2O solar with defects from Table 5.6 cell under AM 1.5 illumination with default parameters given in Table 5.4.

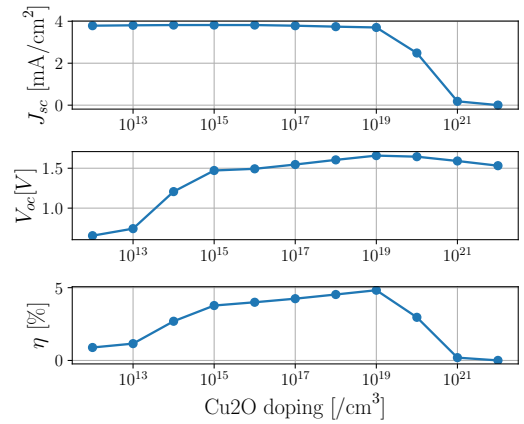

(a) Variation of the I-V parameters with the Cu_2O doping (N_a).

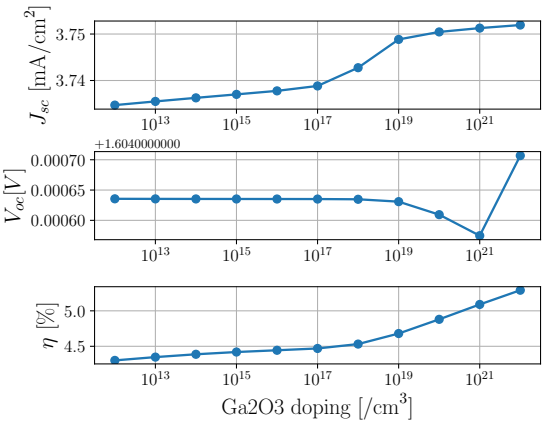

(b) Variation of the I-V parameters with the Ga_2O_3 doping (N_d).

Figure 5.16: Variation of the I-V parameters with both doping concentration of the Ga_2O_3-Cu_2O solar with defects from Table 5.6 cell under AM 1.5 illumination with default parameters given in Table 5.4.

V_{oc} [V]	J_{sc} [mA/cm^2]	FF [%]	η [%]
1.6	3.74	75.49	4.53

Table 5.7: I-V parameters for the optimal solar cell with defects in the bulk without any bias.

5.3.4 Study of the effects due to defects

To have a better understanding of the influence that the defects have on efficiency, one can analyze the recombination rates. To do so, Scaps provides us with the curves for the ideal defective and pristine solar cell in Figure 5.17.

First, only the cuprous oxide part of the cell plays a big role in the cell as the gallium

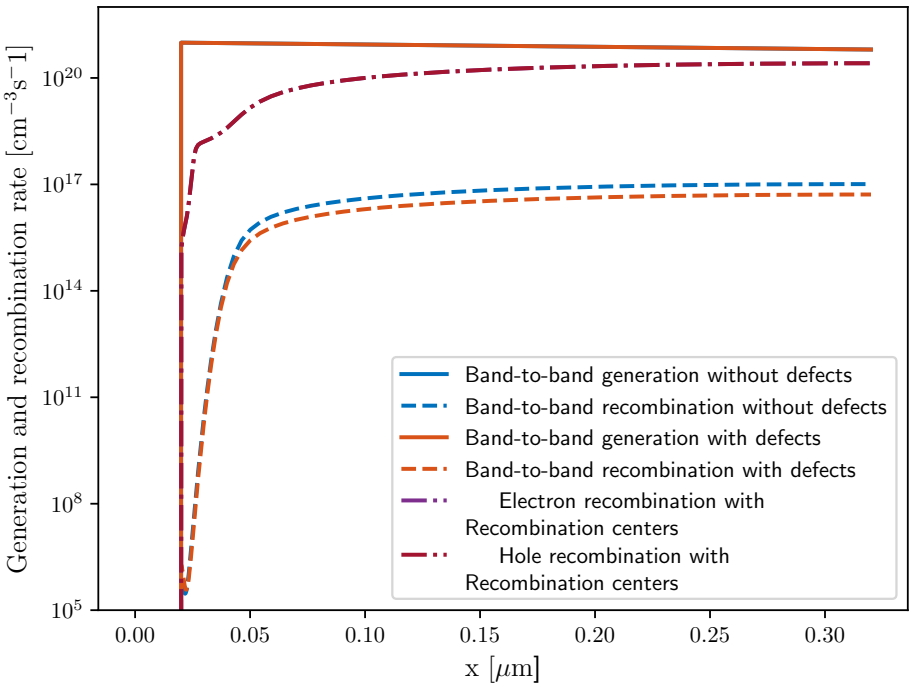

Figure 5.17: Generation and recombination rate for the two defective and pristine Ga_2O_3-Cu_2O with $V_{\text{bias}} = 0$ V and AM 1.5 illumination with default parameters given in Table 5.4.

oxide is transparent to light and does not have a charge generation via light excitation. As can be seen, the optical generation rate is only following the incident rate of photons from AM 1.5 illumination. It is the same for both defective and pristine cells. It only takes the band gap into account. However, having defects in the bulks in the midgap (deep defects) creates recombination centers (RC) for the charge to recombine. Here, while the thermal recombination from the conduction to the valence band is the same for both defective and pristine cells, there are additional recombinations with the traps for both electrons and holes. The recombination through the RC process has a big impact. It has already been reported for perovskite solar cells by Taheri *et al.* in [71], for thin films by Ouslimane *et al.* in [72] and Wischmann *et al.* in [73] that in solar cells, the defects which play the role of mid-band traps reduce the solar cell efficiency. Thus, while the only source of recombination was radiative and Auger recombination (from conduction to valence band), in the defective cell, the recombination can also be made at recombination centers. This means that more recombinations after an optical generation can happen. This decreases the number of charge carriers as some have recombined at recombination centers, hence, the current and thus, the efficiency decrease. The lower density of carriers reduces the drift current and having defects reduces the mobility and thus the diffusion current. However, because experimentally, one cannot avoid defects, it is crucial to take the defects into account to control their impacts. It has been determined in [71] that the deep defects are the most harmful to the recombination rate and the solar cell efficiency.

5.4 Additional AZO layer

Lastly, it has been shown in the literature in [12] and [10] that using two n-type layers with one as a buffer with cuprous oxide can increase solar efficiency. To compare the effect of the N-doping in the cuprous oxide on the solar efficiency, the simulated cell is the same as Minami *et al.* in [10] with Al-doped ZnO (AZO), Ga_2O_3 and Cu_2O. The numerical data are given in Table 5.8. Here, the gallium oxide and cuprous oxide parameters are the same as the optimal cell.

	AZO - n-type	Ga_2O_3 - n-type	Cu_2O - p-type
x [μm]	0.02	0.02	0.3
ε_r	9	10	7.6
E_g [eV]	3.35	4.8	2.1
$q\chi$ [eV]	4.4	4	3.2
N_c [cm^{-3}]	$2.2 \cdot 10^{18}$	$3.72 \cdot 10^{18}$	$2.43 \cdot 10^{19}$
N_v [cm^{-3}]	$1.8 \cdot 10^{-19}$	$3.72 \cdot 10^{18}$	$1.34 \cdot 10^{19}$
μ_n [cm$^2/(V \cdot s)$]	10	118	200
μ_p [cm$^2/(V \cdot s)$]	5	50	0.7
N_d [cm^{-3}]	10^{21}	10^{18}	10^{9}
N_a [cm^{-3}]	10^{9}	10^{9}	10^{14}
α_r [cm$^3/s$]	10^{-12}	10^{-12}	10^{-12}
α_A^n, α_A^p [cm$^6/s$]	10^{-30}	10^{-30}	10^{-30}

Table 5.8: AZO—Ga2O3—Cu2O data for pn junction without defects and without interface states.

It is worth noting that the doping being very large, the depletion width is smaller than 1 nm with a 1 V bias for doping concentration above 10^{18} /cm^3. When smaller, the depletion width can reach 150 nm for a doping concentration of 10^{15} /cm^3. This explains the chosen default AZO thickness.

Important note: to guarantee the convergence of the simulations over the whole voltage range, cuprous oxide doping could not have its optimal value of 10^{18} /cm^3. It had to be lowered. To see if it has an impact on the efficiency, the latter is seen in Figure 5.18. As can be seen, the doping of the Cuprous oxide influences the solar efficiency from 10 to 20 %. This means that it would be great to be able to do the simulations with the proper cuprous oxide doping and not a low value as done in this work due to numerical issues. Here, the chosen cuprous oxide doping as a replacement is 10^{14} /cm^3 for simplicity but one can see that the three tested dopings have the same behavior but slightly different values. One aspect that is not studied in this work is that it seems that the optimal doping of cuprous oxide found in the cell without AZO is not optimal with AZO. It would be interesting to run the optimization with the AZO layer.

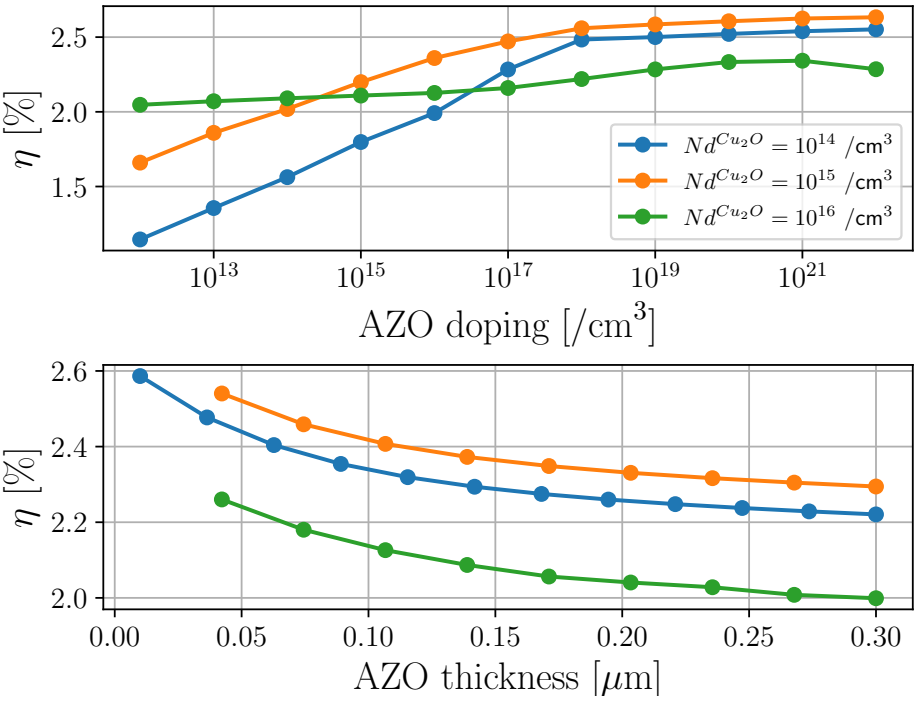

Figure 5.18: Solar efficiency for several Cu_2O doping in the AZO—Ga_2O_3-Cu_2O cell with $V_{\text{bias}} = 0$ V and AM 1.5 illumination with default parameters given in Table 5.4.

5.4.1 Doping and thickness variation

The same study as previously on the majority doping and the thickness of the AZO is made. The results are available in Figure 5.19. Beware that, due to numerical convergence, the software only gives an approximation of the efficiency because it could not reach the open-circuit potential and find the exact efficiency.

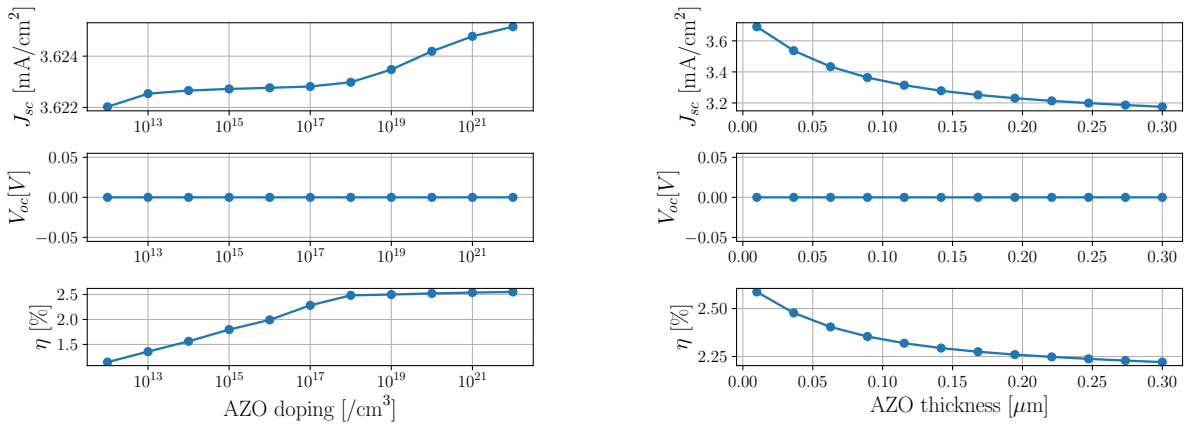

(a) Variation of the I-V parameters with the AZO doping (N_d).

(b) Variation of the I-V parameters with the AZO thickness.

Figure 5.19: Variation of the I-V parameters (without possible open-circuit potential) with doping concentration and thickness of the AZO in the AZO—Ga_2O_3-Cu_2O solar with defects from Table 5.8 cell under AM 1.5 illumination with default parameters given in Table 5.4.

From these results, one can find the optimal AZO parameters.
Hence, one finds:

$$\boxed{N_d^{AZO} = 10^{18}\ /\text{cm}^3,} \qquad \boxed{x^{AZO} = 20\ \text{nm}.} \tag{5.5}$$

As usual, the optimal cell is simulated and gives the parameters in Table 5.9.

V_{oc} [V]	J_{sc} [mA/cm^2]	FF [%]	η [%]
1.75	3.72	38.96	2.48

Table 5.9: I-V parameters for the optimal pristine solar cell with additional AZO layer without any bias.

5.4.2 Additionnal layer analysis

While the best AZO thickness is approximately 6 nm, one major constraint is the deposition process. For such a thin film, it becomes difficult to control precisely the deposition thickness via RF sputtering. Other methods such as thermal evaporation or electro-deposition are even less precise. That is why the choice of the best thickness is a little bit larger than 6 nm to make the deposition easier. Moreover, one needs to be sure that the film can guarantee the doping density for such a small thickness. It has been reported in [74] that for thicknesses

of around 70 nm, the density was around $2 \cdot 10^{20}$ /cm^3. Hence, the film being thinner in our case, the maximum doping is assumed to be experimentally feasible. Moreover, towards 1 nm thick, Scaps has trouble computing the cell correctly, the depletion width is still smaller than 1 nm but care must be taken.

To understand the origin of the doping effect on solar efficiency, one can analyze the recombination rate in Figure 5.20 for two doping densities. One can see that there is only a minor change in the AZO part. The recombination rate is larger when the doping concentration in the AZO is higher. This is the same behavior as for the cuprous oxide. This means that the larger the doping in AZO, the larger the recombination and the smaller the solar efficiency. And naturally, there is no change in the generation rate.

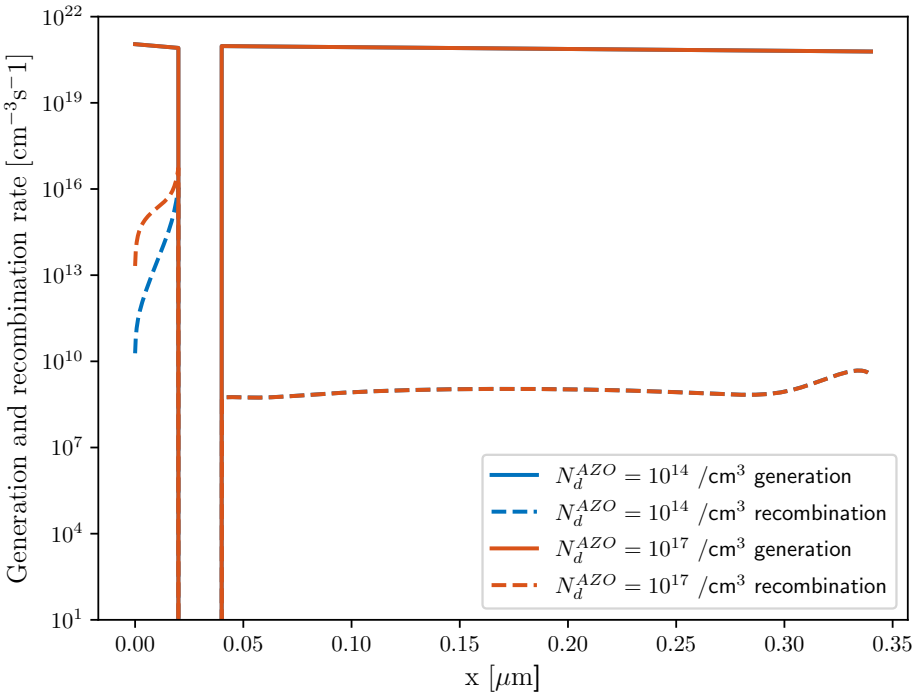

Figure 5.20: Generation and recombination rate for the AZO|Ga_2O_3|Cu_2O junction for two different AZO doping at equilibrium under AM 1.5 illumination.

5.4.3 Unexpected decreasing of the solar efficiency

While it is stated in [12] and [10] that the addition of a second n-type TCO increases the efficiency, it is seen here that the optimal efficiency of the pristine Ga_2O_3|Cu_2O is more than two times better than the pristine AZO|Ga_2O_3|Cu_2O cell. This behavior is quite unexpected. To compare both cells, the recombination and generation rates are shown in Figure 5.21.

As can be seen, there is indeed an optical generation in the AZO layer, this means that fewer photons can reach the cuprous oxide to generate EHP. Additionally, there are just a bit fewer recombinations in the cuprous oxide when the AZO is present. These effects confirm

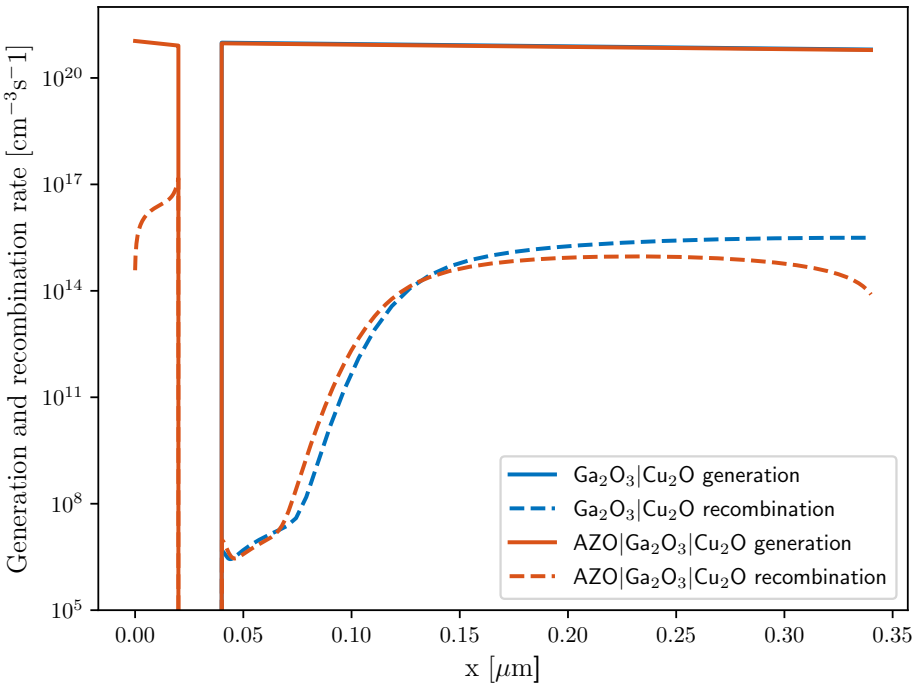

Figure 5.21: Generation and recombination rate for the AZO|Ga_2O_3|Cu_2O junction and the Ga_2O_3|Cu_2O (shifted to match the Cu_2O layer) at equilibrium under AM 1.5 illumination.

the fact that the efficiency is lowered with the addition of the AZO.

However, this behavior is not seen or talked about by Toghyani Rizi *et al.* in [61], where the cell is quite similar. The hypothesis of such a difference comes from the numerical representation of the defects in Scaps.

Indeed, in its paper, Toghyani Rizi, with different software, adds a defective interface layer between the gallium oxide and the cuprous oxide. This is not possible with Scaps as the software does not converge. Thus, there might be a mismatch between the way Toghyani Rizi computes the defects and the way done in this work.

However one can still extract the optimal parameters for the cells as the physics behind them are correct.

5.5 Simulation prospects

While this simulation allows for a first optimal cell and gives the flavor of the impacts of the parameters, some points can be improved and other cases can be studied.

- It would be interesting to be able to simulate the optimal cell with AZO and the optimal Cu_2O doping, as it has not been possible due to numerical issues. Moreover, a rerun of the cuprous oxide optimum study is required as it seemed the behavior was different compared to the cell without AZO.

- As it has been done in [61], representing the interface layers and defective layers between the cuprous oxide and its neighbor is quite important as the contact with Cu_2O is not straightforward. However, such simulations have been tested during this work but it was not possible to guarantee numerical convergence of the Scaps software, hence, another one is needed.
- Here, only AZO has been studied but another n-type buffer such as TiO_2 can be also studied and compared with Ga_2O_3.
- Lastly, no electrode on the top side of the cell has been added and simulated. Gold is often used for its good contact on the top of the cell but this has an impact on the transmission rate of light.

Chapter 6

Conclusion

This work was dedicated to the study of the Cu_2O-based semiconductor structures.

The first part was a brief reminder of semiconductor physics, explaining the concepts of charge carriers, bands, doping, and currents. Then, the homojunction was introduced to explain the heterojunction for the solar cell and the Schottky contact. Lastly, a few words about the current state of the art of both Cu_2O and Ga_2O_3 were said. The promising profile of cuprous oxide as a *p*-type semiconductor and all its uses was also introduced.

The experimental part started with a description of the thin film deposition techniques, namely, RF sputtering and thermal evaporation. Also, the electrical and optical measurement techniques were introduced with typical results such as an XRD pattern for a fabricated film of cuprous oxide.

With these techniques, the four samples were introduced with their nanofabrication parameters. Once measured, these were 200 nm thick, with a resistivity of 6.1 Ωcm, a majority carrier concentration of $2.6 \cdot 10^{18}/\text{cm}^3$ and a in-plane mobility of 0.7 $\text{cm}^2/\text{V}\cdot\text{s}$. After that, thermal annealing under nitrogen atmosphere was applied and a certain temperature threshold was found. When an annealing of 450°C is made, a phase of pure copper appears and the film loses its semiconducting properties. Thus, an annealing at a smaller temperature was performed. That one showed an increase in crystallinity and no change of phase. From the crystallinity measurements, hence, XRD measurements, the texture of the film has been discussed and it has been seen that the film was neither epitaxial nor a random polycrystalline. It is a randomly-oriented textured film. Then, silver has been deposited via thermal evaporation to create a rectifying contact as predicted by the theory. However, it has been observed that the I-V curves did not show the expected rectifying behavior but rather a usual ohmic one. The problem was that the measured resistance, with this ohmic curve, had the value as if there was no cuprous oxide. This meant that the silver passed through the cuprous oxide film. This issue meant that the silver deposition was to be discarded and another solution needed to be found.

The next chapter started by finding an alternative to silver, namely, a tungsten probe directly applied on the back contact, FTO, and the cuprous oxide. This new contact had the advantage of not requiring a deposition as the probe was just applied to the sample. However, the tungsten contact had a drawback as the application was not perfect and perfectly reproducible. However, the literature is quite sparse on this contact. A real study on this contact has not been done yet. Having such contact being promising and easy, it was decided that a study with the tungsten needle would be made. I-V curves are measured and their shape was neither rectifying nor ohmic. Hence, the space-charge-limited current was introduced to model the current behavior in the films. Its physics was explained and a first fit was made to have a linear and quadratic part on the log-log plot of the I-V curve. From this fit, the density of the acceptors in the film was extracted, with also the density of majority carriers in the valence band at equilibrium and the transversal mobility. Once fitted reasonably well to the curve, it was said to be approved and all the curves from all the samples were fit. The transversal mobility varied from 0.015 to 0.18 $cm^2/V{\cdot}s$, the acceptor density was of the order of 10^{16} $/cm^3$ and the density of holes in the valence band at thermal equilibrium was of the order of 10^{17} $/cm^3$. All these physical quantities were found assuming in the Mott-Gurney law that the effect of the acceptor levels were trap levels. From this fit, it has been determined that the in-plane mobility and the transversal were not that different as they were of the same order and the film was more or less textured.

The last chapter aimed at simulating the solar cell Ga_2O_3-Cu_2O. To do so, the software Scaps was introduced. It was first completely analyzed by comparing its results with the theoretical homojunction and heterojunction. Then, the ideal solar cell is optimized by varying the thickness and doping of both layers. It has been found that the more doped, the better. The gallium oxide thickness did not matter that much and the cuprous oxide needed to be as large as possible, regarding the deposition limitations and transparency desired. The parameters were then $1.6 \cdot 10^{18}$ and 50 nm for gallium oxide and 10^{17} $/cm^3$ and 300 nm for cuprous oxide. With these parameters, the solar efficiency was around 5.8 %. After this, the cell with bulk defects was computed and the same optimized parameters were found. However, as expected, the solar efficiency decreased with the addition of the defects. The efficiency is around 4.28 %. It has been decided to add another n-type layer, namely AZO, to enhance solar efficiency. This layer has been optimized without defects. The found thickness was 10 nm and the doping was $1.6 \cdot 10^{19}$ $/cm^3$. The efficiency was 2 %. However, it has been found, strangely, that the solar efficiency was lower for this cell. This behavior was unexpected and this might come from the pristine hypotheses. With proper defects, our solar cell without AZO might not be that good.

From this work, one can raise certain prospects. It might be interesting to try thicker cuprous oxide film with different annealing procedures to check whether the silver still produces a short circuit through the cuprous oxide to the back contact.

Moreover, one could try another contact than tungsten to be sure that our films can exhibit a better SCL model curve such as gold [19] or aluminum [20].

For the simulations, it would be interesting to use another software to be able to model defective layers and interface states between the layers to represent the real issues and have a better understanding of the contact mechanisms. Moreover, the solar cell resistance has not been represented. It is known that the shunt and resistance affect the solar cell efficiency. The numerical issues made the AZO optimum study incomplete and it would be interesting to run a complete variation for the three compounds. These additional features could give a larger range of studied physical parameters to have simulations closer to reality. Lastly, while only gallium oxide and AZO have been considered as n-type layers, studying other n-type materials such as TiO_2 could provide us with better results and better efficiencies.

Bibliography

[1] L. Hu et al. "Design strategy for p-type transparent conducting oxides". In: *Journal of Applied Physics* 128.14 (Oct. 2020), p. 140902. ISSN: 0021-8979. DOI: 10.1063/5.0023656. (Visited on 05/21/2024).

[2] Jorge Osorio-Guillén, Stephan Lany, and Alex Zunger. "Nonstoichiometry and hole doping in NiO". In: *AIP Conference Proceedings* 1199.1 (Jan. 2010), pp. 128–129. ISSN: 0094-243X. DOI: 10.1063/1.3295330. URL: https://doi.org/10.1063/1.3295330 (visited on 05/21/2024).

[3] Ardak Ainabayev et al. "High-performance p-type V2O3 films by spray pyrolysis for transparent conducting oxide applications". en. In: *Scientific Reports* 14.1 (Jan. 2024). Publisher: Nature Publishing Group, p. 1928. ISSN: 2045-2322. DOI: 10.1038/s41598-024-52024-4. URL: https://www.nature.com/articles/s41598-024-52024-4 (visited on 05/21/2024).

[4] Samira Dabaghmanesh et al. "Sulfur-alloyed Cr2O3: a new p-type transparent conducting oxide host". en. In: *RSC Advances* 7.8 (Jan. 2017). Publisher: The Royal Society of Chemistry, pp. 4453–4459. ISSN: 2046-2069. DOI: 10.1039/C6RA27852C. URL: https://pubs.rsc.org/en/content/articlelanding/2017/ra/c6ra27852c (visited on 05/21/2024).

[5] Chun-Ying Huang, En-Chun Wei, and Chia-Tse Yuan. "Dual functional modes for nanostructured p-Cu2O/n-Si heterojunction photodiodes". en. In: *Nanotechnology* 32.7 (Nov. 2020). Publisher: IOP Publishing, p. 075202. ISSN: 0957-4484. DOI: 10.1088/1361-6528/abc50d. URL: https://dx.doi.org/10.1088/1361-6528/abc50d (visited on 05/21/2024).

[6] Naama Sliti. "Physical vapor deposition of copper oxide as p-type material for semiconductor devices". Anglais. Publisher: ULiège - Université de Liège [Faculté des Sciences], Liège, Belgium. PhD thesis. Dec. 2023. URL: https://orbi.uliege.be/handle/2268/311212 (visited on 05/21/2024).

[7] Congrong Wang et al. "Heat management of LED-based Cu2O deposits on the optimal structure of heat sink". en. In: *High Temperature Materials and Processes* 42.1 (Jan. 2023). Publisher: De Gruyter. ISSN: 2191-0324. DOI: 10.1515/htmp-2022-0277. URL: https://www.degruyter.com/document/doi/10.1515/htmp-2022-0277/html (visited on 05/21/2024).

[8] Sinuo Chen et al. "A review of Cu2O solar cell". In: *Journal of Renewable and Sustainable Energy* 15.6 (Nov. 2023), p. 062701. ISSN: 1941-7012. DOI: 10.1063/5.0167383. (Visited on 05/21/2024).

[9] Khadidja Naceur et al. "Study and optimization of Cu2O/AZO hetero-junction solar cell with different buffer layers". In: *Optical Materials* 115 (May 2021), p. 111060. ISSN: 0925-3467. DOI: 10.1016/j.optmat.2021.111060. URL: https://www.sciencedirect.com/science/article/pii/S0925346721002615 (visited on 05/21/2024).

[10] Tadatsugu Minami, Yuki Nishi, and Toshihiro Miyata. "High-Efficiency Cu2O-Based Heterojunction Solar Cells Fabricated Using a Ga2O3 Thin Film as N-Type Layer". en. In: *Applied Physics Express* 6.4 (Mar. 2013). Publisher: IOP Publishing, p. 044101. ISSN: 1882-0786. DOI: 10.7567/APEX.6.044101. URL: https://iopscience.iop.org/article/10.7567/APEX.6.044101/meta (visited on 04/26/2024).

[11] Daniel A. Fentahun, Alekha Tyagi, and Kamal K. Kar. "Numerically investigating the AZO/Cu2O heterojunction solar cell using ZnO/CdS buffer layer". In: *Optik* 228 (Feb. 2021), p. 166228. ISSN: 0030-4026. DOI: 10.1016/j.ijleo.2020.166228. URL: https://www.sciencedirect.com/science/article/pii/S0030402620320301 (visited on 05/21/2024).

[12] Naama Sliti, Saâd Touihri, and Ngoc Duy Nguyen. "Numerical modeling and analysis of AZO/Cu2O transparent solar cell with a TiO2 buffer layer". en. In: *Engineering Research Express* 5.2 (Apr. 2023). Publisher: IOP Publishing, p. 025013. ISSN: 2631-8695. DOI: 10.1088/2631-8695/accacf. URL: https://dx.doi.org/10.1088/2631-8695/accacf (visited on 04/26/2024).

[13] A. Luque and Steven Hegedus, eds. *Handbook of photovoltaic science and engineering*. en. 2nd ed. OCLC: ocn656847927. Chichester, West Sussex, U.K: Wiley, 2011. ISBN: 978-0-470-72169-8.

[14] Chaker Fares, Fan Ren, and S. J. Pearton. "Temperature-Dependent Electrical Characteristics of -Ga $_2$ O $_3$ Diodes with W Schottky Contacts up to 500°C". en. In: *ECS Journal of Solid State Science and Technology* 8.7 (2019), Q3007–Q3012. ISSN: 2162-8769, 2162-8777. DOI: 10.1149/2.0011907jss. URL: https://iopscience.iop.org/article/10.1149/2.0011907jss (visited on 10/26/2023).

[15] A. Lakshmanan, Zachariah C. Alex, and S.R. Meher. "Cu2O thin films grown by magnetron sputtering as solar cell absorber layers". en. In: *Materials Science in Semiconductor Processing* 148 (Sept. 2022), p. 106818. ISSN: 13698001. DOI: 10.1016/j.mssp.2022.106818. URL: https://linkinghub.elsevier.com/retrieve/pii/S1369800122003572 (visited on 08/24/2023).

[16] Ashwin Kumar Saikumar, Shraddha Dhanraj Nehate, and Kalpathy B. Sundaram. "Review—RF Sputtered Films of Ga2O3". en. In: *ECS Journal of Solid State Science and Technology* 8.7 (Feb. 2019), Q3064. ISSN: 2162-8777. DOI: 10.1149/2.0141907jss. URL: https://iopscience.iop.org/article/10.1149/2.0141907jss/meta (visited on 08/21/2023).

[17] "Heterojunctions and Metal Semiconductor Junctions". en. In: Elsevier, 1972. ISBN: 978-0-12-498050-1. DOI: 10.1016/B978-0-12-498050-1.X5001-6. URL: https://linkinghub.elsevier.com/retrieve/pii/B9780124980501X50016 (visited on 08/30/2023).

[18] Oka Kurniawan and Er-Ping Li. "Study of a single coaxial silicon nanowire for on-chip integrated photovoltaic application". In: (Jan. 2009).

[19] Linfeng Pan et al. "High carrier mobility along the [111] orientation in Cu2O photoelectrodes". en. In: *Nature* 628.8009 (Apr. 2024). Publisher: Nature Publishing Group, pp. 765–770. ISSN: 1476-4687. DOI: 10.1038/s41586-024-07273-8. URL: https://www.nature.com/articles/s41586-024-07273-8 (visited on 05/11/2024).

[20] A. E. Rakhshani. "The role of space-charge-limited-current conduction in evaluation of the electrical properties of thin Cu2O films". In: *Journal of Applied Physics* 69.4 (Feb. 1991), pp. 2365–2369. ISSN: 0021-8979. DOI: 10.1063/1.348719. URL: https://doi.org/10.1063/1.348719 (visited on 05/04/2024).

[21] Radu Bunea, Ashwin Kumar Saikumar, and Kalpathy Sundaram. "The Effect of Annealing Temperature and Reactive Gases on Optical Properties of Cu2O Thin Films". en. In: *Materials Sciences and Applications* 12.5 (May 2021). Number: 5 Publisher: Scientific Research Publishing, pp. 182–196. DOI: 10.4236/msa.2021.125012. URL: https://www.scirp.org/journal/paperinformation.aspx?paperid=108948 (visited on 05/20/2024).

[22] Ling Gao et al. "Synthesis of Hierarchical Nanoporous Microstructures via the Kirkendall Effect in Chemical Reduction Process". en. In: *Scientific Reports* 5.1 (Nov. 2015). Publisher: Nature Publishing Group, p. 16061. ISSN: 2045-2322. DOI: 10.1038/srep16061. URL: https://www.nature.com/articles/srep16061 (visited on 05/20/2024).

[23] A. S. M. Sayem Rahman, M. A. Islam, and K. M. Shorowordi. "Electrodeposition and Characterization of Copper Oxide Thin Films for Solar cell Applications". In: *Procedia Engineering*. The 6th BSME International Conference on Thermal Engineering 105 (Jan. 2015), pp. 679–685. ISSN: 1877-7058. DOI: 10.1016/j.proeng.2015.05.048. URL: https://www.sciencedirect.com/science/article/pii/S1877705815008450 (visited on 05/20/2024).

[24] Shogo Ishizuka, Takahiro Maruyama, and Katsuhiro Akimoto. "Thin-Film Deposition of Cu2O by Reactive Radio-Frequency Magnetron Sputtering". en. In: *Japanese Journal of Applied Physics* 39.8A (Aug. 2000). Publisher: IOP Publishing, p. L786. ISSN: 1347-4065. DOI: 10.1143/JJAP.39.L786. URL: https://iopscience.iop.org/article/10.1143/JJAP.39.L786/meta (visited on 05/20/2024).

[25] B. S. Li, K. Akimoto, and A. Shen. "Growth of Cu2O thin films with high hole mobility by introducing a low-temperature buffer layer". In: *Journal of Crystal Growth* 311.4 (Feb. 2009), pp. 1102–1105. ISSN: 0022-0248. DOI: 10.1016/j.jcrysgro.2008.11.038. URL: https://www.sciencedirect.com/science/article/pii/S0022024808012852 (visited on 05/20/2024).

[26] Naama Sliti et al. "Mg-doped Cu2O thin films with enhanced functional properties grown by magnetron sputtering under optimized pressure conditions". In: *Ceramics International* 48.16 (Aug. 2022), pp. 23748–23754. ISSN: 0272-8842. DOI: 10.1016/j.ceramint.2022.05.028. URL: https://www.sciencedirect.com/science/article/pii/S0272884222015814 (visited on 05/20/2024).

[27] Sanggil Han and Andrew J. Flewitt. "Control of grain orientation and its impact on carrier mobility in reactively sputtered Cu2O thin films". In: *Thin Solid Films* 704 (June 2020), p. 138000. ISSN: 0040-6090. DOI: 10.1016/j.tsf.2020.138000. (Visited on 10/12/2023).

[28] Medina Umar et al. "Morphological and stoichiometric optimization of Cu2O thin films by deposition conditions and post-growth annealing". In: *Thin Solid Films* 732 (Aug. 2021), p. 138763. ISSN: 0040-6090. DOI: 10.1016/j.tsf.2021.138763. URL: https://www.sciencedirect.com/science/article/pii/S0040609021002467 (visited on 05/20/2024).

[29] N. A. Raship et al. "Effect of annealing temperature on the properties of copper oxide films prepared by dip coating technique". In: *AIP Conference Proceedings* 1788.1 (Jan. 2017), p. 030121. ISSN: 0094-243X. DOI: 10.1063/1.4968374. URL: https://doi.org/10.1063/1.4968374 (visited on 05/20/2024).

[30] O. V. Diachenko et al. "The influence of optical and recombination losses on the efficiency of thin-film solar cells with a copper oxide absorber layer". In: *Superlattices and Microstructures* 122 (Oct. 2018), pp. 476–485. ISSN: 0749-6036. DOI: 10.1016/j.spmi.2018.06.063. URL: https://www.sciencedirect.com/science/article/pii/S0749603618312692 (visited on 05/21/2024).

[31] Kiryung Eom et al. "Modified band alignment effect in ZnO/Cu2O heterojunction solar cells via Cs2O buffer insertion". en. In: *Journal of Physics D: Applied Physics* 51.5 (Jan. 2018). Publisher: IOP Publishing, p. 055101. ISSN: 0022-3727. DOI: 10.1088/1361-6463/aaa0b6. URL: https://dx.doi.org/10.1088/1361-6463/aaa0b6 (visited on 05/21/2024).

[32] Iñaki López et al. "Field emission properties of gallium oxide micro- and nanostructures in the scanning electron microscope". en. In: *physica status solidi (a)* 209.1 (2012). _eprint: https://onlinelibrary.wiley.com/doi/pdf/10.10 pp. 113–117. ISSN: 1862-6319. DOI: 10.1002/pssa.201127406. URL: https://onlinelibrary.wiley.com/doi/abs/10.1002/pssa.201127406 (visited on 05/21/2024).

[33] Masataka Higashiwaki. "-Ga2O3 material properties, growth technologies, and devices: a review". en. In: *AAPPS Bulletin* 32.1 (Jan. 2022), p. 3. ISSN: 2309-4710. DOI: 10.1007/s43673-021-00033-0. URL: https://doi.org/10.1007/s43673-021-00033-0 (visited on 05/21/2024).

[34] *Copper Mining and Processing: Processing Copper Ores*. en. July 2020. URL: https://superfund.arizona.edu/resources/learning-modules-english/copper-mining-and-processing/processing-copper-ores (visited on 05/04/2024).

[35] Guillaume Zante et al. "Efficient recycling of metals from solar cells using catalytic etchants". In: *Journal of Cleaner Production* 370 (Oct. 2022), p. 133552. ISSN: 0959-6526. DOI: 10.1016/j.jclepro.2022.133552. URL: https://www.sciencedirect.com/science/article/pii/S0959652622031316 (visited on 05/04/2024).

[36] Maryam Kavousi and Eskandar Keshavarz Alamdari. "A Comprehensive and Sustainable Recycling Process for Different Types of Blended End-of-Life Solar Panels: Leaching and Recovery of Valuable Base and Precious Metals and/or Elements". en. In: *Metals* 13.10 (Oct. 2023). Number: 10 Publisher: Multidisciplinary Digital Publishing Institute, p. 1677. ISSN: 2075-4701. DOI: 10.3390/met13101677. URL: https://www.mdpi.com/2075-4701/13/10/1677 (visited on 05/04/2024).

[37] *Fact.MR – Gallium Oxide Substrate Market Analysis Report By Dopant (Sn, Fe), By Application (Visible/ Ultraviolet LEDs, Power Semiconductors,Ultraviolet Detectors), By Region (North America, Europe, Asia Pacific) - Global Market Insights 2022 to 2032*. en. URL: https://www.factmr.com/report/5464/gallium-oxide-substrate-market (visited on 05/02/2024).

[38] M. Maarefvand, S. Sheibani, and F. Rashchi. "Recovery of gallium from waste LEDs by oxidation and subsequent leaching". In: *Hydrometallurgy* 191 (Jan. 2020), p. 105230. ISSN: 0304-386X. DOI: 10.1016/j.hydromet.2019.105230. URL: https://www.sciencedirect.com/science/article/pii/S0304386X19305468 (visited on 05/02/2024).

[39] George F. Harrington and José Santiso. "Back-to-Basics tutorial: X-ray diffraction of thin films". en. In: *Journal of Electroceramics* 47.4 (Dec. 2021), pp. 141–163. ISSN: 1573-8663. DOI: 10.1007/s10832-021-00263-6. (Visited on 05/24/2024).

[40] Yihui Geng. "Mathematical analysis of Van der Pauw's method for measuring resistivity". en. In: *Journal of Physics: Conference Series* 2321.1 (Aug. 2022). Publisher: IOP Publishing, p. 012027. ISSN: 1742-6596. DOI: 10.1088/1742-6596/2321/1/012027. URL: https://dx.doi.org/10.1088/1742-6596/2321/1/012027 (visited on 06/08/2024).

[41] Takumi Ikenoue et al. "Hole mobility improvement in Cu2O thin films prepared by the mist CVD method". en. In: *Applied Physics Express* 12.5 (Apr. 2019). Publisher: IOP Publishing, p. 055509. ISSN: 1882-0786. DOI: 10.7567/1882-0786/ab15b3. URL: https://dx.doi.org/10.7567/1882-0786/ab15b3 (visited on 04/29/2024).

[42] Dieter K. Schroder. *Semiconductor Material and Device Characterization — IEEE eBooks — IEEE Xplore*. English. URL: https://ieeexplore.ieee.org/book/5237928 (visited on 10/18/2023).

[43] Medina Umar et al. "Morphological and stoichiometric optimization of Cu2O thin films by deposition conditions and post-growth annealing". In: *Thin Solid Films* 732 (Aug. 2021), p. 138763. ISSN: 0040-6090. DOI: 10.1016/j.tsf.2021.138763. URL: https://www.sciencedirect.com/science/article/pii/S0040609021002467 (visited on 05/21/2024).

[44] L. H. Xu, D. D. Jiang, and X. J. Zheng. "Effect of grain orientation in x-ray diffraction pattern on residual stress in polycrystalline ferroelectric thin film". In: *Journal of Applied Physics* 112.4 (Aug. 2012), p. 043521. ISSN: 0021-8979. DOI: 10.1063/1.4748052. URL: https://doi.org/10.1063/1.4748052 (visited on 05/29/2024).

[45] Jiacheng He et al. "Fast synthesis of hierarchical cuprous oxide for nonenzymatic glucose biosensors with enhanced sensitivity". en. In: *Journal of Materials Science* 51.21 (Nov. 2016), pp. 9696–9704. ISSN: 1573-4803. DOI: 10.1007/s10853-016-0202-3. URL: https://doi.org/10.1007/s10853-016-0202-3 (visited on 05/13/2024).

[46] F. Chaffar Akkari et al. "Impedance spectroscopy characterization of anisotropic nano-sculptured copper oxide Cu2O thin films for optoelectronic applications". en. In: *Semiconductor Science and Technology* 34.7 (June 2019). Publisher: IOP Publishing, p. 075026. ISSN: 0268-1242. DOI: 10.1088/1361-6641/ab0ecf. URL: https://dx.doi.org/10.1088/1361-6641/ab0ecf (visited on 05/15/2024).

[47] M. Chelvayohan and C. H. B. Mee. "Work function measurements on (110), (100) and (111) surfaces of silver". en. In: *Journal of Physics C: Solid State Physics* 15.10 (Apr. 1982), p. 2305. ISSN: 0022-3719. DOI: 10.1088/0022-3719/15/10/029. URL: https://dx.doi.org/10.1088/0022-3719/15/10/029 (visited on 05/22/2024).

[48] Jonas Deuermeier et al. "Visualization of nanocrystalline CuO in the grain boundaries of Cu2O thin films and effect on band bending and film resistivity". In: *APL Materials* 6.9 (Sept. 2018), p. 096103. ISSN: 2166-532X. DOI: 10.1063/1.5042046. URL: https://doi.org/10.1063/1.5042046 (visited on 05/22/2024).

[49] Thi Thu Ha Pham et al. "Synthesis of cuprous oxide/silver (Cu2O/Ag) hybrid as surface-enhanced Raman scattering probe for trace determination of methyl orange". In: *Royal Society Open Science* 10.5 (May 2023). Publisher: Royal Society, p. 221623. DOI: 10.1098/rsos.221623. URL: https://royalsocietypublishing.org/doi/full/10.1098/rsos.221623 (visited on 05/15/2024).

[50] Daniel B. Butrymowicz, John R. Manning, and Michael E. Read. "Diffusion in Copper and Copper Alloys, Part II. Copper-Silver and Copper-Gold Systems". In: *Journal of Physical and Chemical Reference Data* 3.2 (Apr. 1974), pp. 527–602. ISSN: 0047-2689. DOI: 10.1063/1.3253145. URL: https://doi.org/10.1063/1.3253145 (visited on 05/15/2024).

[51] Alaa Nihad Tuama et All. "An Overview on Characterization of Silver/Cuprous Oxide Nanometallic(Ag/Cu2O) As Visible Light Photocatalytic". en. In: *International Journal of Advanced Science and Technology* 29.3 (Mar. 2020). Number: 3, pp. 5008–5018. ISSN: 2005-4238. (Visited on 05/15/2024).

[52] Tri Arini et al. "The Effect of deposition times on preparation of SnO2:F conductive glass by Indonesian local stannic chloride precursors". en. In: *IOP Conference Series: Materials Science and Engineering* 541.1 (June 2019). Publisher: IOP Publishing, p. 012022. ISSN: 1757-899X. DOI: 10.1088/1757-899X/541/1/012022. URL: https://dx.doi.org/10.1088/1757-899X/541/1/012022 (visited on 05/21/2024).

[53] Sin Cheng Siah et al. "Low contact resistivity of metals on nitrogen-doped cuprous oxide (Cu2O) thin-films". In: *Journal of Applied Physics* 112.8 (Oct. 2012), p. 084508. ISSN: 0021-8979. DOI: 10.1063/1.4758305. URL: https://doi.org/10.1063/1.4758305 (visited on 05/21/2024).

[54] Shouqiang Wei et al. "Fabrication of WO3/Cu2O composite films and their photocatalytic activity". In: *Journal of Hazardous Materials* 194 (Oct. 2011), pp. 243–249. ISSN: 0304-3894. DOI: 10.1016/j.jhazmat.2011.07.096. URL: https://www.sciencedirect.com/science/article/pii/S0304389411009770 (visited on 05/27/2024).

[55] C. L. Azanza Ricardo et al. "Structural properties of RF-magnetron sputtered Cu2O thin films". In: *Thin Solid Films* 520.1 (Oct. 2011), pp. 280–286. ISSN: 0040-6090. DOI: 10.1016/j.tsf.2011.07.066. URL: https://www.sciencedirect.com/science/article/pii/S0040609011014532 (visited on 10/12/2023).

[56] Millan F. Diaz-Aguado et al. "Experimental Investigation of Total Photoemission Yield from New Satellite Surface Materials". In: *Journal of Spacecraft and Rockets* 56.1 (Jan. 2019). Publisher: American Institute of Aeronautics and Astronautics, pp. 248–258. ISSN: 0022-4650. DOI: 10.2514/1.A34245. URL: https://arc.aiaa.org/doi/10.2514/1.A34245 (visited on 06/08/2024).

[57] Richard Tran et al. "Anisotropic work function of elemental crystals". In: *Surface Science* 687 (Sept. 2019), pp. 48–55. ISSN: 0039-6028. DOI: 10.1016/j.susc.2019.05.002. (Visited on 05/09/2024).

[58] F. L. Weichman and K. T. Chee. "Pt–Cu2O–Cu single-carrier space-charge-limited diodes". In: *Canadian Journal of Physics* 55.7-8 (Apr. 1977). Publisher: NRC Research Press, pp. 735–741. ISSN: 0008-4204. DOI: 10.1139/p77-101. URL: https://cdnsciencepub.com/doi/10.1139/p77-101 (visited on 05/04/2024).

[59] Yun Seog Lee et al. "Nitrogen-doped cuprous oxide as a p-type hole-transporting layer in thin-film solar cells". en. In: *Journal of Materials Chemistry A* 1.48 (Nov. 2013). Publisher: The Royal Society of Chemistry, pp. 15416–15422. ISSN: 2050-7496. DOI: 10.1039/C3TA13208K. URL: https://pubs.rsc.org/en/content/articlelanding/2013/ta/c3ta13208k (visited on 05/25/2024).

[60] Claudia Malerba et al. "Nitrogen doped Cu2O: A possible material for intermediate band solar cells?" In: *Solar Energy Materials and Solar Cells* 105 (Oct. 2012), pp. 192–195. ISSN: 0927-0248. DOI: 10.1016/j.solmat.2012.06.017. URL: https://www.sciencedirect.com/science/article/pii/S0927024812002954 (visited on 05/27/2024).

[61] Majid Toghyani Rizi, M. H. Shahrokh Abadi, and M. Ghaneii. "Two dimensional modeling of Cu2O heterojunction solar cells based-on -Ga2O3 buffer". In: *Optik* 155 (Feb. 2018), pp. 121–132. ISSN: 0030-4026. DOI: 10.1016/j.ijleo.2017.11.028. URL: https://www.sciencedirect.com/science/article/pii/S0030402617314316 (visited on 11/02/2023).

[62] M Burgelman, P Nollet, and S Degrave. "Modelling polycrystalline semiconductor solar cells". In: *Thin Solid Films* 361-362 (Feb. 2000), pp. 527–532. ISSN: 0040-6090. DOI: 10.1016/S0040-6090(99)00825-1. URL: https://www.sciencedirect.com/science/article/pii/S0040609099008251 (visited on 05/19/2024).

[63] Abderrahmane Béroual, Sophie Guillemet-Fritsch, and Thierry Lebey. "Capacitors for Power Electronics". In: *Power Electronics Semiconductor Devices*. John Wiley Sons, Ltd, 2009. Chap. 5. ISBN: 9780470611494. DOI: https://doi.org/10.1002/9780470611494.ch5.

[64] "Performance of conversion efficiency of a crystalline silicon solar cell with base doping density". en-US. In: *Results in Physics* 7 (Jan. 2017). Publisher: Elsevier, pp. 4264–4268. ISSN: 2211-3797. DOI: 10.1016/j.rinp.2017.10.039. URL: https://www.sciencedirect.com/science/article/pii/S2211379717313669 (visited on 05/19/2024).

[65] Dávid Kovács et al. "Position of gold dictates the photophysical and photocatalytic properties of Cu2O in Cu2O/Au multicomponent nanoparticles". en. In: *Journal of Materials Chemistry C* 11.26 (July 2023). Publisher: The Royal Society of Chemistry, pp. 8796–8807. ISSN: 2050-7534. DOI: 10.1039/D3TC01213A. URL: https://pubs.rsc.org/en/content/articlelanding/2023/tc/d3tc01213a (visited on 05/18/2024).

[66] Yuki Takiguchi and Shinsuke Miyajima. "Device simulation of cuprous oxide heterojunction solar cells". en. In: *Japanese Journal of Applied Physics* 54.11 (Oct. 2015). Publisher: IOP Publishing, p. 112303. ISSN: 1347-4065. DOI: 10.7567/JJAP.54.112303. (Visited on 04/26/2024).

[67] Marko J. Tadjer et al. "Editors' Choice—Review—Theory and Characterization of Doping and Defects in -Ga2O3". en. In: *ECS Journal of Solid State Science and Technology* 8.7 (Mar. 2019). Publisher: IOP Publishing, Q3187. ISSN: 2162-8777. DOI: 10.1149/2.0341907jss. URL: https://iopscience.iop.org/article/10.1149/2.0341907jss/meta (visited on 04/26/2024).

[68] Michael Nolan and Simon D. Elliott. "The p-type conduction mechanism in Cu2O: a first principles study". en. In: *Physical Chemistry Chemical Physics* 8.45 (Nov. 2006). Publisher: The Royal Society of Chemistry, pp. 5350–5358. ISSN: 1463-9084. DOI: 10.1039/B611969G. URL: https://pubs.rsc.org/en/content/articlelanding/2006/cp/b611969g (visited on 06/03/2024).

[69] M. Adaika et al. "Numerical simulation of bias and photo stress on indium–gallium–zinc-oxide thin film transistors". In: *Vacuum*. SATF 2014: Science and Application of Thin Films, Conference & Exhibition 120 (Oct. 2015), pp. 59–67. ISSN: 0042-207X. DOI: 10.1016/j.vacuum.2015.04.021. URL: https://www.sciencedirect.com/science/article/pii/S0042207X15001736 (visited on 05/16/2024).

[70] Paulina Sawicka-Chudy et al. "Review of the development of copper oxides with titanium dioxide thin-film solar cells". In: *AIP Advances* 10.1 (Jan. 2020), p. 010701. ISSN: 2158-3226. DOI: 10.1063/1.5125433. URL: https://doi.org/10.1063/1.5125433 (visited on 05/16/2024).

[71] Sara Taheri et al. "Effect of defects on high efficient perovskite solar cells". In: *Optical Materials* 111 (Jan. 2021), p. 110601. ISSN: 0925-3467. DOI: 10.1016/j.optmat.2020.110601. URL: https://www.sciencedirect.com/science/article/pii/S0925346720309411 (visited on 05/16/2024).

[72] Touria Ouslimane et al. "Impact of absorber layer thickness, defect density, and operating temperature on the performance of MAPbI3 solar cells based on ZnO electron transporting material". In: *Heliyon* 7.3 (Mar. 2021), e06379. ISSN: 2405-8440. DOI: 10.1016/j.heliyon.2021.e06379. URL: https://www.ncbi.nlm.nih.gov/pmc/articles/PMC7937749/ (visited on 05/16/2024).

[73] W. Wischmann et al. “CIGS Thin-Film Solar Cells with an Improved Efficiency of 20.8%”. In: Nov. 2014. (Visited on 05/16/2024).

[74] Yong Wu, Fa Cao, and Xiaohong Ji. “Optical and electrical properties of Al-doped ZnO thin films by atomic layer deposition”. en. In: *Journal of Materials Science: Materials in Electronics* 31.20 (Oct. 2020), pp. 17365–17374. ISSN: 1573-482X. DOI: 10.1007/s10854-020-04292-9. URL: https://doi.org/10.1007/s10854-020-04292-9 (visited on 05/28/2024).